ABSTRACT

HOSSEN, ELVIN. Removal of Organic Ions Using Capacitive Deionization: An Experimental and Modeling Approach to Understand Adsorption Mechanisms (Under the direction of Dr. Douglas Call).

Application of advanced separation technologies in water and wastewater industry has always been a critical challenge for stakeholders to ensure more sustainable process of contaminant removal or species recovery. An increasing pressure for environmental protection as well as resource demand resulted in the elevated interests of exploring a wide range of separation techniques to maximize process efficiency and prioritize circular green economy concept. Presence of organic contaminants in water or wastewater is one of the focal points for advanced separation methods given the potential for the recovery of valuable organic species.

Capacitive deionization (CDI), an electrochemical method for desalination, has primarily been studied and developed for the removal of small inorganic ions (e.g., Na^+, Cl^-). However, our fundamental understanding of organic ion electrosorption lags behind that of inorganic ions, which prevents the informed design and operation of CDI cells that can selectively remove organics. Many organic ions have properties that vary significantly from model inorganic ions particularly pertaining to their ability to be physically and/or chemically adsorbed to activated carbon (AC)-based electrodes. It is challenging, if not impossible, to extrapolate experimental and modeling efforts from inorganic to organic ions, especially those with dramatically different properties. This dissertation provides insights into organic ion removal in CDI by conducting three projects: 1) studying the removal of short-chain carboxylate ions in CDI, 2) elucidating the contribution of different adsorption processes of organic ions and their impacts on electrode

properties and performances of CDI, and 3) establishing kinetic and thermodynamic models to predict the performance of short-chain carboxylate ions in CDI.

The first project (Chapter 2) shows how CDI with AC cloth electrodes can remove short-chain carboxylate ions from water at different capacity depending on the ionic mobility and size of organic ions, providing the first answer towards understanding the adsorption of organic ions in CDI.

The second project (Chapter 3) investigated the dynamics of different adsorption mechanisms in CDI treating carboxylate ions, highlighting the role of non-electrosorption of organic ions in changing the ability of carbon electrodes to electrosorb charged species.

The third project (Chapter 4) delved into the kinetic and thermodynamic modeling development and verification in order to better estimate the performance of CDI treating carboxylate ions. Both experimental and modeling approaches, as well as computational analysis were performed in this dissertation to understand the adsorption mechanisms of organic ions onto carbon electrodes in CDI.

Removal of Organic Ions Using Capacitive Deionization: An Experimental and Modeling Approach to Understand Adsorption Mechanisms

by

Elvin Hossen

A dissertation submitted to the Graduate Faculty of

North Carolina State University

in partial fulfillment of the

requirements for the degree of

Doctor of Philosophy

Civil Engineering

Raleigh, North Carolina

2022

APPROVED BY:

_____	_____
Douglas Call Committee Chair	Detlef Knappe
_____	_____
Joel Ducoste	Edmond Bowden

DEDICATION

This dissertation is dedicated to my parents, Addrison Hossen and Helmiyati Amir Hamzah, and my lovely wife, Widya Imanesti, who all give me the greatest gift anyone could give another person: they believe in me.

BIOGRAPHY

Elvin Hossen always believes he is taking the roads less traveled by. Growing up in Pekanbaru, Indonesia, he decided to continue his secondary education at a religious boarding school and live in another island, far from his parents at the age of 15. He received his bachelor's degree in Chemical Engineering from Institut Teknologi Bandung, Indonesia, in 2009. He started his graduate study in 2011 at North Carolina State University and received his Master of Science degree in Environmental Engineering in 2013. After working for almost three years as process engineer in Indonesia, he returned to Raleigh, NC in 2016 to pursue a doctoral degree in Civil Engineering. His research focuses on different electrochemical methods for water/wastewater treatment as well as alternative energy generation. During his first year of graduate study, he investigated the acclimatization strategy for microbial fuel cell (MFC) treating wastewater with high salinity. He also collaborated with a team from NCSU and UNC Chapel Hill to investigate the temporal variation of power production via reverse electrodialysis (RED) using coastal North Carolina waters and how it correlated with the temperature and salinity. For his dissertation research, he relies extensively on different electrochemical techniques, analytical chemistry approaches, and mathematical and semi-empirical model development to understand the adsorption of organic ions under the voltage application influence in capacitive deionization (CDI). He currently serves as an R&D engineer for an advanced materials company in Minneapolis, MN.

ACKNOWLEDGEMENTS

I sincerely would like to address my gratitude to the following people who have played a very important part in this second chapter of my graduate student life here at North Carolina State University:

- Dr. Douglas Call, for his countless hours advising, encouraging, assisting, reviewing, and patiently guiding the past six ebullient years of my PhD journey
- Members of my PhD committee, Dr. Detlef Knappe, Dr. Joel Ducoste, and Dr. Edmond Bowden, for their generosity in sharing their expertise and precious time in supporting my research work and serving on my committee.
- Dr. Lisa Castellano, our lab manager, who played the biggest role in helping me analyzing those never-ending water samples
- The current and past members of Call lab group, Dr. Juan Fausto Ortiz Medina, Dr. Qiwen Cheng, Dr. Mark Poole, Yazeed Algurainy, Sol Park, Jenny Ding, Ethan Quinn, Dr. Fei Liu, and Dr. Shan Zhu, for their friendship and support after all these years.
- Friends of the CCEE department, Dr. Yi-Chun Lai, Dr. Amanda Karam, Diyuan Wang, Asmita Narode, Lan Cheng, Giovanna Portiolli, Jacqueline Yeh, Dr. Dominic Libera, and Dr. Zack Hopkins, Dr. Chuhui Zhang, for all the laughter and tears.
- My Indonesian friends in Raleigh, my second family, for their support and fun time every weekend doing countless karaoke nights, potluck parties, and road trips for the last six years.
- My family: mom, dad, my sister, and her family. Thank you for always being there for me, even though we are separated by 10000 miles of distance and 12 hours of time.
- And most importantly, to my wife. Thank you for breathing life into my existence.

-

TABLE OF CONTENTS

LIST OF FIGURES

Chapter 1. Introduction

Capacitive Deionization (CDI) is an emerging technology that removes ions from brackish water [1]. When porous carbon-based electrodes in CDI are charged with an electrical potential, counterions (oppositely charged ions) are transported from the bulk solution and accumulate into the electrical double layer (EDL) formed on the surface of the electrodes, i.e., electrosorbed, resulting in lower salinity water in the effluent (See **Figure 1.1**). Different types of electrode materials have been investigated, but high electrical conductivity and high surface are the two most common properties that are sought after for CDI electrodes [2]. The electrosorption process in CDI is reversible, meaning that when the application of electrical potential on the electrode stops, the previously stored ions will be released back into the solution, renewing the electrode for additional electrosorption cycles. Compared with other technologies (e.g., ion exchange, evaporation, and reverse osmosis), CDI provides several advantages including reversibility, no use of chemicals, low maintenance costs (approximately a third of the maintenance costs for reverse osmosis (RO)), long-term cyclability of electrode materials, and wide range of application [2–6]. That said, current advancement of CDI still leaves big room for improvement, as there are still several factor which prevent CDI technology to be scaled-up. As a desalination technology, current CDI still cannot compete with RO on the basis of energy consumption, water recovery, salinity range, or capital cost [7]; CDI requires specific energy consumption of 0.85 kWh/m3 to treat brackish water (2000 mg/L salt concentration), 8 times higher than RO (~0.09 kWh/m3) [7].

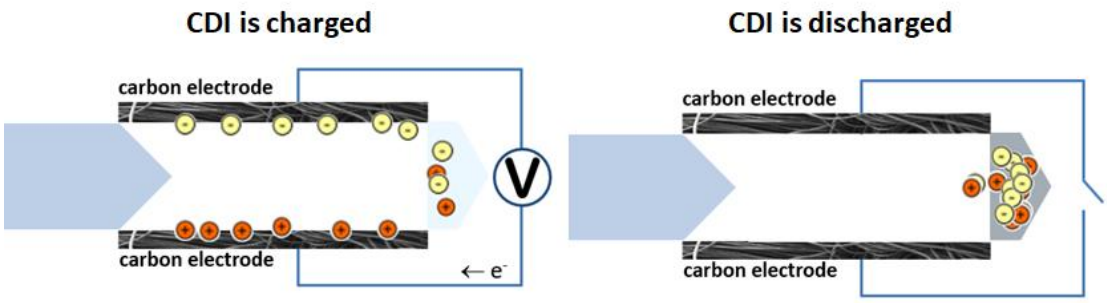

Figure 1.1. Schematic diagram on how capacitive deionization (CDI) works

Applications of CDI have expanded beyond brackish water desalination to inorganic ion removal in a variety of matrices. Examples include removing ions that cause water hardness ([7–11], remediation of wastewater to remove hazardous contaminants such as heavy metals, dyes, antibiotics, or organic contaminants [12–19] , and selective valuable ion recovery [20–26]. Various types of ions have now been investigated, including Na^+, K^+, NH_4^+, Mg^{2+}, Ca^{2+}, Cl^-, NO_3^-, SO_4^{2-}, PO_4^{3-}, or heavy metal ions such as Cr^{2+}, Pb^{2+}, Cd^{2+}, Fe^{3+} from water or wastewater [14,27–38] but CDI still faces many challenges before widespread commercial adoption can occur [39]. When compared to conventional treatment such as reverse osmosis (RO), current advancement of CDI still resulted in significantly less energy-efficient for brackish water desalination as well as more capital cost [40–43]. On the other hand, organic fouling and low efficiency for contaminant removal rendered CDI not competitive against common chemical- or physicochemical-based technology such with precipitation or coagulation for wastewater treatment [44–46]. For selective ion recovery, CDI is still lacking selectivity (e.g., for lithium) when compared to the use of conventional adsorbent such as hydrogenated manganese oxide (HMO) [20,24].

One area that has received little attention is the removal of organic ions. Organic ions in aqueous environmental matrices can vary significantly in size, shape, structure, composition,

mobility, charge, etc. [47]. As such, we cannot rely on our knowledge of small inorganic ions such as Na^+ and Cl^- to understand and predict removal of all organic ions in CDI. Some organic ions may be persistent pollutants such as dioxins, surfactants, organochloride pesticides, perfluorinated compounds among others [48,49]. Removing them from water and wastewater could reduce human and environmental risk. Other organic ions such as the short-chain carboxylates acetate, butyrate, and caproate, are present in natural and engineered systems as byproducts of microbial metabolisms. If recovered those ions could be highly valuable inputs to many commercial products. The carboxylates generated during the anaerobic digestion of wastes are one such resource where these ions are present. Utilizing CDI technology to separate and recover those ions would be advantageous from a commercial standpoint.

Several exploratory studies have showed that large organic ions can be removed in CDI, but fundamental mechanistic insight into how they are removed is missing [2,50–53]. In many cases, organic ions have been studied in the context of organic fouling of electrodes and/or membranes, with little attention given to the processes involved in ion sorption onto electrodes. Most importantly, for organic ions that can physically and/or chemically adsorb to porous carbon materials, there is no information about how those mechanisms influence their electrosorption and electrodesorption. Granular activated carbon (GAC), for example, showed a promising ability to adsorb hexanoate with affinity two times higher than pentanoate and more than six times higher than formate-butyrate, as measured by its adsorption capacity term; indicating that in the absence of an applied potential, carboxylate ions can be removed from bulk solution [54,55]. The model inorganic ion, Cl^-, on the other hand, exhibits little to no physical or chemical adsorption [56]. It is critically important to understand how inherent ion affinity for porous

carbon influences removals in CDI so that models can be created or refined, and new materials or operational strategies implemented to selectively remove those ions.

To address this knowledge gap, we conducted systematic research investigation of organic ion removal in CDI using a series of short-chain carboxylic acids (formate, acetate, butyrate, and hexanoate) as model ions. These ions are present in many biological systems, including anaerobic digesters, and if recovered would serve as valuable precursors to a variety of industrial usage such as in pharmaceutical, food, chemical industries [47]. In Chapter 2, we focused on the first research question, can CDI remove the carboxylate ions from water and if so, how well? We tested the electrosorption of organic ions using a flow-through CDI cell. We compared several metrics, including ions adsorption capacity against Cl^- as a benchmark for a model inorganic ion. Our results showed that non-electrical adsorption of organic ions, which typically is not a primary mechanism of removal of small inorganic ions, is an important property that needs to be taken into consideration when understanding electrosorption of organic ions. Moreover, this dissertation further discussed about the dynamic contribution of different adsorption mechanisms when CDI used to remove organic ions (Chapter 3). The goal of this objective was to identify the contribution of physical/chemical adsorption and its impact on the overall performance of CDI. Several electrode pretreatments were investigated to highlight the change in adsorption mechanism favorability due to electrolyte-electrode interactions. We also propose further research to better understand the mechanisms and impact of physical and chemical adsorption of organic ions during CDI operation. Lastly, this dissertation also provided a foundation for kinetic and modelling approaches to predict the performance of CDI treating organic ions in Chapter 4.

References

[1] J.E. Dykstra, S. Porada, A. Van Der Wal, P.M. Biesheuvel, Energy consumption in Capacitive Deionization – constant current versus constant voltage operation, Water Res. 143 (2018) 1–12. doi:10.1016/j.watres.2018.06.034.

[2] S. Porada, R. Zhao, A. Van Der Wal, V. Presser, P.M. Biesheuvel, Progress in Materials Science Review on the science and technology of water desalination by capacitive deionization, Prog. Mater. Sci. 58 (2013) 1388–1442. doi:10.1016/j.pmatsci.2013.03.005.

[3] M. Suss, Capacitive water desalination with hierarchical porous electrodes, (2013) 126. https://searchworks.stanford.edu/view/10160559.

[4] S. Porada, L. Weinstein, R. Dash, A. Van Der Wal, M. Bryjak, Y. Gogotsi, P.M. Biesheuvel, Water desalination using capacitive deionization with microporous carbon electrodes, ACS Appl. Mater. Interfaces. 4 (2012) 1194–1199. doi:10.1021/am201683j.

[5] S.J. Seo, H. Jeon, J.K. Lee, G.Y. Kim, D. Park, H. Nojima, J. Lee, S.H. Moon, Investigation on removal of hardness ions by capacitive deionization (CDI) for water softening applications, Water Res. 44 (2010) 2267–2275. doi:10.1016/j.watres.2009.10.020.

[6] C.H. Hou, J.F. Huang, H.R. Lin, B.Y. Wang, Preparation of activated carbon sheet electrode assisted electrosorption process, J. Taiwan Inst. Chem. Eng. 43 (2012) 473–479. doi:10.1016/j.jtice.2011.12.003.

[7] Z.Y. Leong, H.Y. Yang, Capacitive Deionization of Divalent Cations for Water Softening Using Functionalized Carbon Electrodes, (2020). doi:10.1021/acsomega.9b02330.

[8] J.J. Lado, R.L. Zornitta, I. Vázquez Rodríguez, K. Malverdi Barcelos, L.A.M. Ruotolo, Sugarcane Biowaste-Derived Biochars as Capacitive Deionization Electrodes for Brackish

Water Desalination and Water-Softening Applications, ACS Sustain. Chem. Eng. 7 (2019) 18992–19004. doi:10.1021/acssuschemeng.9b04504.

[9] Y.J. Kim, J.H. Kim, J.H. Choi, Selective removal of nitrate ions by controlling the applied current in membrane capacitive deionization (MCDI), J. Memb. Sci. 429 (2013) 52–57. doi:10.1016/j.memsci.2012.11.064.

[10] G. Bharath, K. Rambabu, F. Banat, A. Hai, A.F. Arangadi, N. Ponpandian, Enhanced electrochemical performances of peanut shell derived activated carbon and its Fe3O4 nanocomposites for capacitive deionization of Cr(VI) ions, Sci. Total Environ. 691 (2019) 713–726. doi:10.1016/j.scitotenv.2019.07.069.

[11] K. Fang, H. Gong, W. He, F. Peng, C. He, K. Wang, Recovering Ammonia from Municipal Wastewater by Flow-Electrode Capacitive Deionization, Chem. Eng. J. 348 (2018) 301–309. doi:10.1016/j.cej.2018.04.128.

[12] O. Pastushok, F. Zhao, D.L. Ramasamy, M. Sillanpää, Nitrate removal and recovery by capacitive deionization (CDI), Chem. Eng. J. 375 (2019) 121943. doi:10.1016/j.cej.2019.121943.

[13] D.I. Oyarzun, A. Hemmatifar, J.W. Palko, M. Stadermann, J.G. Santiago, Adsorption and capacitive regeneration of nitrate using inverted capacitive deionization with surfactant functionalized carbon electrodes, Sep. Purif. Technol. 194 (2018) 410–415. doi:10.1016/j.seppur.2017.11.027.

[14] L. Legrand, O. Schaetzle, R.C.F. De Kler, H.V.M. Hamelers, Solvent-Free CO 2 Capture Using Membrane Capacitive Deionization, (2018). doi:10.1021/acs.est.8b00980.

[15] A. Ullah, M. Wajid, W. Kim, International Journal of Greenhouse Gas Control Performance and energy cost evaluation of an integrated NH 3 -based CO 2 capture-

capacitive deionization process, Int. J. Greenh. Gas Control. 66 (2017) 85–96. doi:10.1016/j.ijggc.2017.09.013.

[16] K. Zuo, J. Kim, A. Jain, T. Wang, R. Verduzco, M. Long, Q. Li, Novel Composite Electrodes for Selective Removal of Sulfate by the Capacitive Deionization Process, (2018). doi:10.1021/acs.est.8b01868.

[17] Y. Cheng, Z. Hao, C. Hao, Y. Deng, X. Li, K. Li, Y. Zhao, A review of modi fi cation of carbon electrode material in capacitive deionization, (2019) 24401–24419. doi:10.1039/c9ra04426d.

[18] D.I. Oyarzun, A. Hemmatifar, J.W. Palko, M. Stadermann, J.G. Santiago, Ion selectivity in capacitive deionization with functionalized electrode: Theory and experimental validation, Water Res. X. 1 (2018) 100008. doi:10.1016/j.wroa.2018.100008.

[19] Y. Xu, H. Zhou, G. Wang, Y. Zhang, H. Zhang, H. Zhao, Selective Pseudocapacitive Deionization of Calcium Ions in Copper Hexacyanoferrate, ACS Appl. Mater. Interfaces. 12 (2020) 41437–41445. doi:10.1021/acsami.0c11233.

[20] J. Lee, S. Kim, N. Kim, C. Kim, J. Yoon, Enhancing the desalination performance of capacitive deionization using a layered double hydroxide coated activated carbon electrode, Appl. Sci. 10 (2020) 12–15. doi:10.3390/app10010403.

[21] A. Kalfa, B. Shapira, A. Shopin, I. Cohen, E. Avraham, Chemosphere Capacitive deionization for wastewater treatment : Opportunities and challenges, Chemosphere. 241 (2020) 125003. doi:10.1016/j.chemosphere.2019.125003.

[22] P. Liang, X. Sun, Y. Bian, H. Zhang, X. Yang, Y. Jiang, P. Liu, X. Huang, Optimized desalination performance of high voltage flow-electrode capacitive deionization by adding carbon black in flow-electrode, Desalination. 420 (2017) 63–69.

doi:10.1016/j.desal.2017.05.023.

[23] E.M. Remillard, A.N. Shocron, J. Rahill, M.E. Suss, C.D. Vecitis, A direct comparison of flow-by and flow-through capacitive deionization, Desalination. 444 (2018) 169–177. doi:10.1016/j.desal.2018.01.018.

[24] R.D. Cusick, Y. Kim, B.E. Logan, Energy Capture from Thermolytic Solutions in Microbial Reverse-Electrodialysis Cells, Science (80-.). 335 (2012) 1474–1477. doi:10.1126/science.1219330.

[25] C. Zhang, D. He, J. Ma, W. Tang, T.D. Waite, Comparison of faradaic reactions in flow-through and flow-by capacitive deionization (CDI) systems, Electrochim. Acta. 299 (2019) 727–735. doi:10.1016/j.electacta.2019.01.058.

[26] C. Zhang, J. Ma, D. He, T.D. Waite, Capacitive Membrane Stripping for Ammonia Recovery (CapAmm) from Dilute Wastewaters, Environ. Sci. Technol. Lett. 5 (2018) 43–49. doi:10.1021/acs.estlett.7b00534.

[27] A. Rommerskirchen, A. Kalde, C.J. Linnartz, L. Bongers, G. Linz, M. Wessling, Unraveling charge transport in carbon flow-electrodes: Performance prediction for desalination applications, Carbon N. Y. 145 (2019) 507–520. doi:10.1016/j.carbon.2019.01.053.

[28] F. Liu, O. Coronell, D.F. Call, Electricity generation using continuously recirculated flow electrodes in reverse electrodialysis, J. Power Sources. 355 (2017) 206–210. doi:10.1016/j.jpowsour.2017.04.061.

[29] N.A. Thu Tran, N.M. Phuoc, H. Yoon, E. Jung, Y.W. Lee, B.G. Kang, H.S. Kang, C.Y. Yoo, Y. Cho, Improved Desalination Performance of Flow- A nd Fixed-Capacitive Deionization using Redox-Active Quinone, ACS Sustain. Chem. Eng. 8 (2020) 16701–

16710. doi:10.1021/acssuschemeng.0c06651.

[30] J. Choi, H. Lee, S. Hong, Capacitive deionization (CDI) integrated with monovalent cation selective membrane for producing divalent cation-rich solution, Desalination. 400 (2016) 38–46. doi:10.1016/j.desal.2016.09.016.

[31] Y. Zhang, L. Zou, Y. Wimalasiri, J.Y. Lee, Y. Chun, Reduced graphene oxide/polyaniline conductive anion exchange membranes in capacitive deionisation process, Electrochim. Acta. 182 (2015) 383–390. doi:10.1016/j.electacta.2015.09.128.

[32] P. Liang, L. Yuan, X. Yang, S. Zhou, X. Huang, Coupling ion-exchangers with inexpensive activated carbon fiber electrodes to enhance the performance of capacitive deionization cells for domestic wastewater desalination, Water Res. 47 (2013) 2523–2530. doi:10.1016/j.watres.2013.02.037.

[33] A. Hassanvand, G.Q. Chen, P.A. Webley, S.E. Kentish, Improvement of MCDI operation and design through experiment and modelling: Regeneration with brine and optimum residence time, Desalination. 417 (2017) 36–51. doi:10.1016/j.desal.2017.05.004.

[34] Y. Zhang, P. Srimuk, M. Aslan, M. Gallei, V. Presser, Polymer ion-exchange membranes for capacitive deionization of aqueous media with low and high salt concentration, Desalination. 479 (2020) 114331. doi:10.1016/j.desal.2020.114331.

[35] P.A. Fritz, F.K. Zisopoulos, S. Verheggen, K. Schroën, R.M. Boom, Exergy analysis of membrane capacitive deionization (MCDI), Desalination. (2018) 0–1. doi:10.1016/j.desal.2018.01.026.

[36] K. Laxman, D. Kimoto, A. Sahakyan, J. Dutta, Nanoparticulate Dielectric Overlayer for Enhanced Electric Fields in a Capacitive Deionization Device, ACS Appl. Mater. Interfaces. 10 (2018) 5941–5948. doi:10.1021/acsami.7b16540.

[37] H.J. Oh, J.H. Lee, H.J. Ahn, Y. Jeong, Y.J. Kim, C.S. Chi, Nanoporous activated carbon cloth for capacitive deionization of aqueous solution, Thin Solid Films. 515 (2006) 220–225. doi:10.1016/j.tsf.2005.12.146.

[38] K. Laxman, D. Kimoto, A. Sahakyan, J. Dutta, Nanoparticulate Dielectric Overlayer for Enhanced Electric Fields in a Capacitive Deionization Device, ACS Appl. Mater. Interfaces. 10 (2018) 5941–5948. doi:10.1021/acsami.7b16540.

[39] J. Luo, D. Tian, Z. Ding, T. Lu, X. Xu, L. Pan, Enhanced cycling stability of capacitive deionization via effectively inhibiting H2O2 formation: The role of nitrogen dopants, J. Electroanal. Chem. 855 (2019) 113488. doi:10.1016/j.jelechem.2019.113488.

[40] P. Nie, W. Cai, Z. Xie, X. Shang, J. Liu, Inversion phenomenon and effective charging quantity in capacitive deionization device, Ionics (Kiel). 26 (2020) 3523–3529. doi:10.1007/s11581-019-03431-5.

[41] P. Hojati-Talemi, L. Zou, M. Fabretto, R.D. Short, Using oxygen plasma treatment to improve the performance of electrodes for capacitive water deionization, Electrochim. Acta. 106 (2013) 494–499. doi:10.1016/j.electacta.2013.05.119.

[42] L.M. Chang, X.Y. Duan, W. Liu, Preparation and electrosorption desalination performance of activated carbon electrode with titania, Desalination. 270 (2011) 285–290. doi:10.1016/j.desal.2011.01.008.

[43] W. Li, H. Yusha, L. Yifei, F. Jiangtao, H. Ning, M. Li, Desalination mechanism of modified activated carbon/carbon nanotubes composite electrode, Water Sci. Technol. Water Supply. 19 (2019) 2054–2060. doi:10.2166/ws.2019.082.

[44] S. Porada, G. Feng, M.E. Suss, V. Presser, Capacitive deionization in organic solutions: Case study using propylene carbonate, RSC Adv. 6 (2016) 5865–5870.

doi:10.1039/c5ra20786j.

[45] J. Chang, F. Duan, H. Cao, K. Tang, C. Su, Y. Li, Superiority of a novel flow-electrode capacitive deionization (FCDI) based on a battery material at high applied voltage, Desalination. 468 (2019) 114080. doi:10.1016/j.desal.2019.114080.

[46] L. Lin, J. Hu, J. Liu, X. He, B. Li, X.Y. Li, Selective Ammonium Removal from Synthetic Wastewater by Flow-Electrode Capacitive Deionization Using a Novel K2Ti2O5-Activated Carbon Mixture Electrode, Environ. Sci. Technol. 54 (2020) 12723–12731. doi:10.1021/acs.est.0c04383.

[47] P. Nativ, O. Lahav, Y. Gendel, Separation of divalent and monovalent ions using flow-electrode capacitive deionization with nanofiltration membranes, Desalination. 425 (2018) 123–129. doi:10.1016/j.desal.2017.10.026.

[48] J.G. Hong, W. Zhang, J. Luo, Y. Chen, Modeling of power generation from the mixing of simulated saline and freshwater with a reverse electrodialysis system: The effect of monovalent and multivalent ions, Appl. Energy. 110 (2013) 244–251. doi:10.1016/j.apenergy.2013.04.015.

[49] Z. Ge, X. Chen, X. Huang, Z.J. Ren, Capacitive deionization for nutrient recovery from wastewater with disinfection capability, Environ. Sci. Water Res. Technol. (2018). doi:10.1039/C7EW00350A.

[50] M.S. Gaikwad, C. Balomajumder, Simultaneous electrosorptive removal of chromium(VI) and fluoride ions by capacitive deionization (CDI): Multicomponent isotherm modeling and kinetic study, Sep. Purif. Technol. 186 (2017) 272–281. doi:10.1016/j.seppur.2017.06.017.

[51] T. Alfredy, Y.A.C. Jande, T. Pogrebnaya, Removal of lead ions from water by capacitive

deionization electrode materials derived from chicken feathers, J. Water Reuse Desalin. 9 (2019) 282–291. doi:10.2166/wrd.2019.074.

[52] L. Xu, C. Yu, Y. Mao, Y. Zong, B. Zhang, H. Chu, D. Wu, Can flow-electrode capacitive deionization become a new in-situ soil remediation technology for heavy metal removal?, J. Hazard. Mater. 402 (2021) 123568. doi:10.1016/j.jhazmat.2020.123568.

[53] T. Wang, C. Zhang, L. Bai, B. Xie, Z. Gan, J. Xing, G. Li, H. Liang, Scaling behavior of iron in capacitive deionization (CDI) system, Water Res. 171 (2020) 115370. doi:10.1016/j.watres.2019.115370.

[54] E. Bayram, E. Ayranci, Electrochemically Enhanced Removal of Polycyclic Aromatic Basic Dyes from Dilute Aqueous Solutions by Activated Carbon Cloth Electrodes, 44 (2010) 6331–6336.

[55] E. Bayram, E. Ayranci, Electrosorption based waste water treatment system using activated carbon cloth electrode : Electrosorption of benzoic acid from a flow-through electrolytic cell, Sep. Purif. Technol. 86 (2012) 113–118. doi:10.1016/j.seppur.2011.10.032.

[56] X. Gao, S. Porada, A. Omosebi, K. Liu, P.M. Biesheuvel, J. Landon, Complementary surface charge for enhanced capacitive deionization, Water Res. 92 (2016) 275–282. doi:10.1016/j.watres.2016.01.048.

[57] L.K. Park, S.J. Satinover, S. Yiacoumi, R.T. Mayes, Electrosorption of Organic Acids from Aqueous Bio-oil and Conversion into Hydrogen via Microbial Electrolysis Cells, (2018).

[58] L. Xu, Y. Xie, Y. Zong, Y. Mao, B. Zhang, H. Chu, D. Wu, Formic acid recovery from EDTA wastewater using coupled ozonation and flow-electrode capacitive deionization (

Ozo / FCDI): Performance assessment at high cell voltage, Sep. Purif. Technol. 254 (2021) 117613. doi:10.1016/j.seppur.2020.117613.

[59] H. Kim, Y. Choi, S. Lee, K.B. Lee, K.W. Jung, J.W. Choi, Pretreatment for capacitive deionization: Feasibility tests using activated filter media and granule activated carbon filtration, J. Ind. Eng. Chem. 93 (2021) 253–258. doi:10.1016/j.jiec.2020.10.001.

[60] M. Mossad, L. Zou, Study of fouling and scaling in capacitive deionisation by using dissolved organic and inorganic salts, J. Hazard. Mater. 244–245 (2013) 387–393. doi:10.1016/j.jhazmat.2012.11.062.

[61] L. Chen, C. Wang, S. Liu, Q. Hu, L. Zhu, C. Cao, Investigation of the long-term desalination performance of membrane capacitive deionization at the presence of organic foulants, Chemosphere. 193 (2018) 989–997. doi:10.1016/j.chemosphere.2017.11.130.

[62] S. Liang, M. Li, J. Cao, K. Zuo, Y. Bian, K. Xiao, X. Huang, Integrated ultrafiltration–capacitive-deionization (UCDI) for enhanced antifouling performance and synchronous removal of organic matter and salts, Sep. Purif. Technol. 226 (2019) 146–153. doi:10.1016/j.seppur.2019.05.085.

[63] Z. Wang, Y. Wang, D. Ma, S. Xu, J. Wang, Investigations on the fouling characteristics of ion-doped polypyrrole/carbon nanotube composite electrodes in capacitive deionization by using half cycle running mode, Sep. Purif. Technol. 192 (2018) 15–20. doi:10.1016/j.seppur.2017.09.004.

Chapter 2: Removal of short-chain carboxylate ions in capacitive deionization (CDI)

2.1. Abstract

Capacitive deionization (CDI), an electrochemical method for desalination, has primarily been studied and developed for the removal of small inorganic ions (e.g., Na^+, Cl^-). However, our fundamental understanding of organic ion electrosorption lags behind that of inorganic ions, which prevents the informed design and operation of CDI cells that can selectively remove organics. Many organic ions have properties that vary significantly from model inorganic ions. It is challenging, if not impossible, to extrapolate experimental and modeling efforts from inorganic to organic ions, especially those with dramatically different properties. To address this knowledge gap, we conducted a systematic research investigation of organic ion adsorption onto activated carbon cloth (ACC) electrode using model short-chain carboxylate ions in CDI cell. We first tested the specific capacitance of ACC in carboxylate-containing solutions to investigate the prospective of ACC as CDI electrode for organic ions removal. We determined the ion adsorption capacity (IAC) of CDI in treating formate ($HCOO_3^-$), acetate (CH_3COO^-), butyrate ($C_3H_7COO^-$), and hexanoate ($C_5H_{11}COO^-$) as well as Cl^- for inorganic benchmark. The contribution of physical and chemical adsorption on the overall removal of the organic ions in CDI was studied by comparing the total ions removed during charging (physical, chemical, plus electrosorption) to those recovered after the discharging step (i.e., only the electrosorbed ions). Our results showed that the ACC electrodes possess a large microporosity and stable electrochemical performance in short-chain carboxylate-containing solution with specific

capacitances of 77.6 – 119 F/g. We observed that total-IAC for the largest carboxylate, hexanoate, was the lowest among all tested carboxylates (115.5 ± 18.6 μmol/g-C), while it was the highest for formate (199.3 ± 25.0 μmol/g-C). The decrease in adsorption capacity as the carboxylate size increased was likely due to (1) higher solution resistance, (2) a decrease in the anode potential (which decreased the driving force for anion adsorption), and (3) physical/chemisorption which may have negatively impacted electrosorption due to the introduction of carboxyl groups from the carboxlyates onto the electrode surface. We also found that CDI in hexanoate solution showed a higher proportion of ion adsorbed due to non-electrostatic force, compared to smaller carboxylate ions. Energetic assessment for CDI for organic solutions showed that charge efficiency and energy-normalized adsorbed ions (ENAI) decreases as the carboxylate ion getting larger. These results should lay the groundwork towards understanding the adsorption of organic ions into carbon electrode in CDI.

2.2. Significance

This work is the first systematic investigation of organic ion electrosorption in CDI. The results improve our understanding of adsorption mechanisms of organic ions and lay the foundation for modeling and optimizing electrodes that remove organic ions from aqueous environments.

2.3.Introduction

Capacitive Deionization (CDI) is an emerging technology that removes ions from brackish water [1]. When porous carbon-based electrodes in CDI are charged with an electrical potential, counterions (oppositely charged ions) are transported from the bulk solution and accumulate into

the electrical double layer (EDL) formed on the surface of the electrodes, i.e., electrosorbed, resulting in lower salinity water in the effluent. Different types of electrode materials have been investigated, but high electrical conductivity and high surface are the two most common properties that are sought after for CDI electrodes [2]. The electrosorption process in CDI is reversible, meaning that when the application of electrical potential on the electrode stops, the previously stored ions will be released back into the solution, renewing the electrode for additional electrosorption cycles. Compared with other technologies (e.g., ion exchange, evaporation, and reverse osmosis), CDI provides several advantages including reversibility, no use of chemicals, , low maintenance costs, approximately a third of the maintenance costs for reverse osmosis (RO), long-term cyclability of electrode materials, and wide range of application [2–6].

Applications of CDI have expanded beyond brackish water desalination to inorganic ion removal in a variety of matrices. Examples include removing ions that cause water hardness ([7–11], remediation of wastewater to remove hazardous contaminants such as heavy metals, dyes, antibiotics, or organic contaminants [12–19] , and selective valuable ion recovery [20–26]. Various types of ions have now been investigated, including Na^+, K^+, $NH4^+$, Mg^{2+}, Ca^{2+}, Cl^-, NO_3^-, SO_4^{2-}, PO_4^{3-}, or heavy metal ions such as Cr^{2+}, Pb^{2+}, Cd^{2+}, Fe^{3+} from water or wastewater [14,27–38] but CDI still faces many challenges before widespread commercial adoption can occur [39]. When compared to conventional treatment such as reverse osmosis (RO), current advancement of CDI still resulted in significantly less energy-efficient for brackish water desalination and requires larger capital cost [40–43]. On the other hand, organic fouling and low efficiency for contaminant removal rendered CDI not competitive against common chemical- or physicochemical-based technology such as precipitation or coagulation for wastewater treatment

[44–46]. For selective ion recovery, CDI is still lacking selectivity (e.g., for lithium) when compared to the use of conventional adsorbent such as hydrogenated manganese oxide (HMO) [20,24].

One area that has received little attention is the removal of organic ions. Organic ions in aqueous environmental matrices can vary significantly in size, shape, structure, composition, mobility, charge, etc. [47]. As such, we cannot rely on our knowledge of small inorganic ions such as Na^+ and Cl^- to understand and predict removal of organic ions in CDI. Some organic ions may be persistent pollutants such as dioxins, surfactants, organochloride pesticides, perfluorinated compounds among others [48,49]. Removing them from water and wastewater could reduce human and environmental risk. Other organic ions such as the short-chain carboxylates acetate, butyrate, and caproate, are present in natural and engineered systems as byproducts of microbial metabolisms. If recovered those ions could be highly valuable inputs to many commercial products. The carboxylates generated during the anaerobic digestion of wastes are one such resource where these ions are present. Utilizing CDI technology to separate and recover those ions would be advantageous from a commercial standpoint.

Several exploratory studies have showed that large organic ions can be removed in CDI, but fundamental mechanistic insight into how they are removed is missing [2,50–53]. In many cases, organic ions have been studied in the context of organic fouling of electrodes and/or membranes, with little attention given to the processes involved in ion sorption onto electrodes. Most importantly, for organic ions that can physically and/or chemically adsorb to porous carbon materials, there is no information about how those mechanisms influence their electrosorption and electrodesorption. Granular activated carbon (GAC), for example, exhibits a high adsorption capacity for hexanoate with affinity 2 times higher than pentanoate and >6 times higher than

formate-butyrate, as measured by its adsorption capacity term; indicating that in the absence of an applied potential, that carboxylate ions can be removed from bulk solution [54,55]. The model inorganic ion, Cl-, on the other hand, exhibits little to no physical or chemical adsorption [56]. It is critically important to understand how inherent ion affinity for porous carbon influences removals in CDI so that models can be created or refined, and new materials or operational strategies implemented to selectively remove those ions.

To address this knowledge gap, we conducted a systematic research investigation of organic ion removal in CDI using a series of short-chain carboxylic acids (formate, acetate, butyrate, and hexanoate) as model ions. These ions are present in many biological systems, including anaerobic digesters, and if recovered would serve as valuable precursors to a variety of industrial usage such as in pharmaceutical, food, chemical industries [47]. We used a flow-through CDI cell and monitored the change in conductivity of each ion during charging and quantified effluent concentrations using ion chromatography. We compared several metrics, including ions adsorption capacity against Cl- as a benchmark for inorganic ion. Our results show that that non-electrical adsorption of organic ions, which typically is not a primary mechanism of removal of small inorganic ions, is an important property that needs to be taken into consideration when understanding electrosorption of organic ions. In this chapter we also propose further works to better understand the mechanism and impact of physical and chemical adsorption of organic ions during CDI operation.

2.4. Experimental Section

2.4.1. Materials and Experimental Setup

Four short-chain carboxylate ions were used in this study: formate (CHO_2^-), acetate ($C_2H_3O_2^-$), butyrate ($C_4H_7O_2^-$), and hexanoate ($C_6H_{11}O_2^-$), with Cl- included as a model inorganic ion for comparison and benchmarking purposes. Each anion-containing solution was made from their respective sodium salt dissolved in deionized water (18.2 μΩ) to achieve 5 mM concentration. All chemicals used in this work were analytical reagent grade (>99% purity) purchased from Sigma Aldrich (USA) and used without further treatment and purification.

The CDI cell consisted of two outer plates of polycarbonate plastic, 5 cm x 5 cm, and 0.5 cm thickness, two interior polycarbonate plates with a 3 cm diameter reservoir, and two graphite plates with dimensions of 5 cm x 5 cm x 0.32 cm as current collectors (with 3 cm hole extruded). The electrodes used in this study were commercially available activated carbon cloth (ACC-5092-20, Kynol Europa GmBH, Germany), which are well characterized in several previous CDI studies [58,59]. Using N_2 adsorption in a Quantachrome Autosorb iQ system, we recorded a surface area of 1658.08 ± 21.74 m^2/g and pore volume of 0.80 ± 0.02 mL/gr for a pristine ACC. The pore size distribution (PSD) was calculated assuming slit-like pores in the density functional theory (DFT) method with a NLDFT equilibrium calculation model provided by ASIQwin software from Quantachrome. Prior to N_2 adsorption, the ACC samples were first degassed under backfill condition approximately for 5.2 hours with a final outgas temperature of 300^{o}C.

For the CDI experiments, two ACC electrodes (one for anode and one for cathode) were first cut in circular shape to a size of 3.81 cm diameter. Prior to use, the electrodes were rinsed with deionized water and dried in air at 80^{o}C overnight, and then weighed to obtain a mass of

188.3 ± 2.4 mg each and stored in desiccator. In the CDI cell, the anode and cathode were separated by a 25 μm thick, porous polypropylene spacer (3501, Celgard, USA) to prevent electrical short-circuiting. Neoprene rubber gaskets with identical dimensions (thickness 0.38 mm and 0.78 mm) were laser cut and inserted between the polycarbonate and graphite plates to tightly seal the cell and avoid liquid leakage. Versilon 2001 tubing (L/S 16) was used to direct the flow from the peristaltic pump (Masterflex, Cole-Palmer, USA) to the CDI cell. On the effluent line, a flow through conductivity electrode (eDAQ Pty, Australia) and pH micro electrode (eDaq Pty, Australia) were installed to continuously monitor the conductivity and pH changes, respectively, while a flow cell was used whenever dissolved oxygen (DO) monitoring using a NEOFOX DO probe (OceanOptics, USA) was necessary. A potentiostat (VMP3, BioLogic, France) was used to monitor open circuit voltage (OCV) and apply an electrical potential (E_{apl}) to the CDI cell during charging (E_{cell} = 1.2 V) and discharging (E_{cell} = 0 V), the positioning of alligator clips on the current collector established the upstream-cathode, downstream-anode CDI configuration. Two low-profile Ag/AgCl reference electrodes (PINE, USA)) were each placed in the reservoirs upstream and downstream of the current collectors and were used to measure the anode and cathode half-cell potentials during the experiments. A schematic diagram showing the CDI setup is presented in **Figure 2.1**.

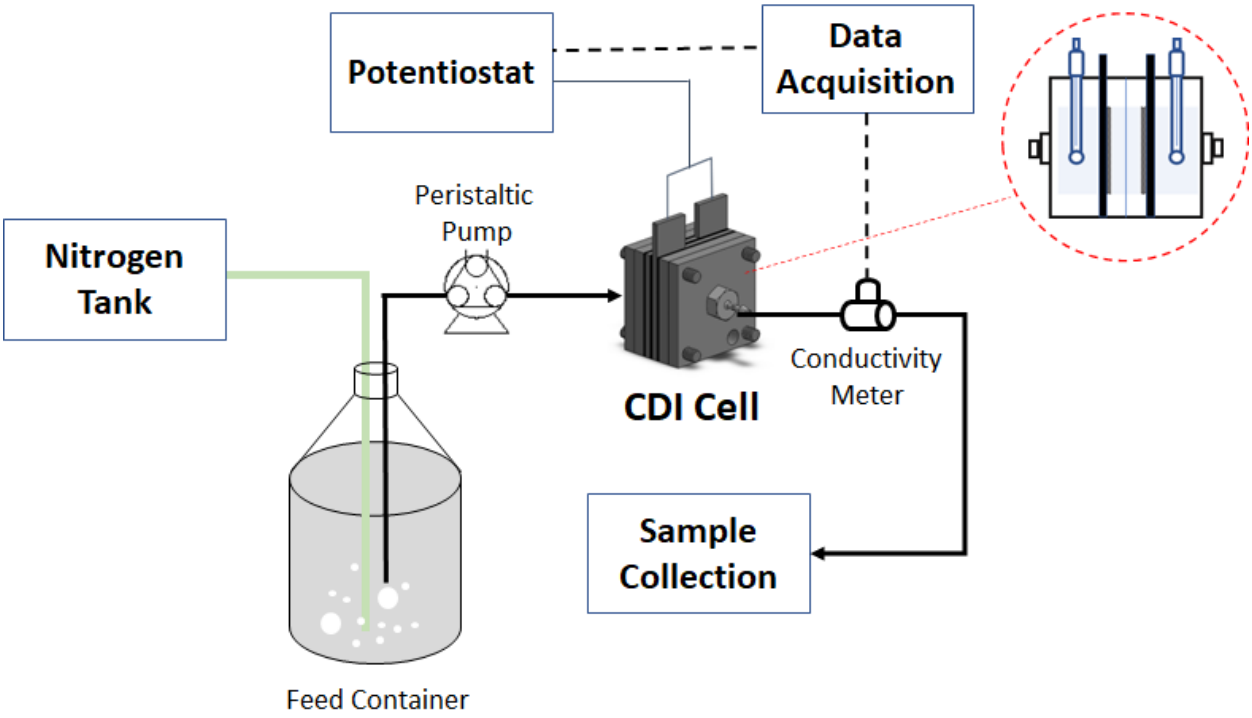

Figure 2.1. Schematic diagram of the CDI system used in this study for the electrosorption of carboxylate ions. The CDI cell was operated with upstream-cathode/downstream-anode configuration in single-pass continuous-flow mode during the electrode conditioning and electrosorption steps. The inset of CDI cell shows the positioning of reference electrodes (blue drawing), current collectors, ACC electrodes, and the spacer in the middle of cell.

2.4.2. Electrochemical Characterization of ACC

Several different electrochemical techniques were used to characterize the ACC. To determine the specific capacitance and resistance profiles, cyclic voltammetry (CV) and electrochemical impedance spectroscopy (EIS) were conducted in a separate 3-electrode setup of cube cell with titanium ring connected to titanium wire as the current collector, ACC as the working electrode (dry mass = 45.9 ± 1.5 mg) and counter electrode (dry mass = 188.3 ± 2.4 mg), and Ag/AgCl as the reference electrode (BASi, USA) in an aqueous solution of 0.5 M NaHCOO, $NaCH_3COO$, NaC_3H_7COO, $NaC_5H_{11}COO$, and NaCl. This relatively high concentration was selected to minimize diffusional and transport-related limitations and to avoid

ion starvation during CV [59,60]. The cell configuration is described by the following steps: ACC were employed as both working electrode (WE) and counter electrode (CE), with surface area of the CE to be much larger than WE to ensure no hindrance of the electron flow and more accurate current measurements. The cell was built from polycarbonate block cut cylindrically to have a working volume of 5 mL. On both ends of the polycarbonate plate, plastic barbed fittings were installed to let the flow of solutions can flow in and out of the cell. During the CV operation, the solution inside the cell is recirculated to ensure good mixing and limit diffusion limitation. The voltammograms from CV were used to confirm the electrosorptive characteristic and reversible behavior of the ACC, and the stability of carboxylate ions during multiple cycles of polarization. For each solution, CV with a scan rate of 5 mV/s was done in 10 cycles, with voltage window of -0.8 V to +0.8 V. The specific capacitance was calculated using the following equation [61]:

$$C_s = \frac{\int I\, dV}{v\, m\, \Delta V} \tag{2.1}$$

Where C_s ($F.g^{-1}$) is the specific capacitance, IdV is the integrated area under the CV curve, v ($mV.s^{-1}$) is the scan rate, m (g) is the mass of working electrode, and ΔV (V) is the potential window.

2.4.3. CDI Operation

For all tests, single salts were continuously flushed through the CDI cell. A target concentration of 5 mM was used for all salts. The salts were NaHCOO, $NaCH_3COO$, NaC_3H_7COO, $NaC_5H_{11}COO$,, or NaCl. The solution was continuously purged with ultra-high purity (UHP) nitrogen gas in a 4 L glass reservoir to keep the DO levels low (2-3 ppm recorded

using a DO probe) before being pumped (Masterflex, Cole-Parmer, USA) into the CDI cell at volumetric flow rate of 3 mL/min. The N_2 purging was done to minimize the impact of parasitic Faradaic reactions (e.g., O_2 reduction, carbon oxidation) on ion electrosorption and CDI performance. A pulse dampener in the form polyethylene body (Cole-Parmer, USA) was placed between the pump head and the cell in order to minimize the pulsation effect from the pump on the solution flow and to stabilize the conductivity readings. In this study, CDI experiment was defined as 3-hr 1.2 V charging followed by 3-hr 0 V discharging. Prior to CDI experiment, the cell was being prepared in three phases. Phase 1: the cell was continuously flushed with DI water for one hour to remove impurities from the ACC. In Phase 2, we flushed the cell with respective feed solution for 12-hr at open circuit with the goal to fully saturate the electrode with the solution. For phase 3, the cell was conditioned by performing a 12-cycle of 30-min charging (E_{apl} = 1.2 V) and 30-min discharging (E_{apl} = 0 V). Effluent conductivity, current response, and electrode potential were continuously monitored during this conditioning. After conditioning, single-pass cell charging was carried out again at a constant voltage of 1.2 V for 180 minutes only and was followed by 0 V discharging step for another 180-minute. For each step, effluent samples were accumulated in a container (for a total of 540 mL sample) for subsequent analysis. The 180 min charging period was selected based on preliminary tests which showed after 3 hours, the current reading for CDI were already stagnating, indicating the electrosorption process reached equilibrium. During this CDI experiment, conductivity and pH data were acquired for monitoring purposes, and effluent anion concentrations were determined using ion chromatography (ICS-5000$^+$, Thermo Fisher, USA) while sodium concentrations were determined using a sodium ion selective electrode (Orion 8611BNWP, Thermo Scientific, USA).

In this study, we measured ion adsorption capacity (IAC) using two different methods. First, we calculated the number of ions removed during the charging step normalized to the electrode mass using Eq.2.2, later we defined this adsorption capacity as *total-IAC*:

$$total - IAC = \frac{v(C_i - C_{e,c})}{m} \quad (2.2)$$

Where v (mL) is the volume of effluent accumulated from the charging step, C_i and $C_{e,c}$ (mmol/L) are the influent and effluent ion concentration after charging, and m (g) is the total mass of electrodes. This approach is consistent with prior studies. However, since some of the organic ions in this study are known to physically or chemically adsorb, we also used a second method to quantify IAC due to electrosorption only, i.e., electrosorption-IAC. We referred this method to previous studies which found that calculating electrosorption capacity from discharging step give more accurate value since charging the electrodes at ~1 V can result in the deviation of effluent pH from the influent which impacts the solution conductivity and complicate the analysis [62–64]. This issue can be a result of resistive dissipation, parasitic side reactions, and/or redistribution of accumulated charge within the electrodes [65]. On the other hand, it is well-characterized that physical and chemical adsorption are mostly irreversible processes where adsorbate tends to stick onto the carbon surface unless external force is being applied or the drawing solution is being replaced. In the case of discharging step at 0 V following the charging, most electrosorbed ions would be released back into the bulk solution due to the dissipation of electrical double layer, indicating that the ions recovered during the discharging step were only the ions being previously electrosorbed, hence the actual electrosorption capacity (electrosorption-IAC). **Figure 2.2** shows the graphical representation of this proposed methods.

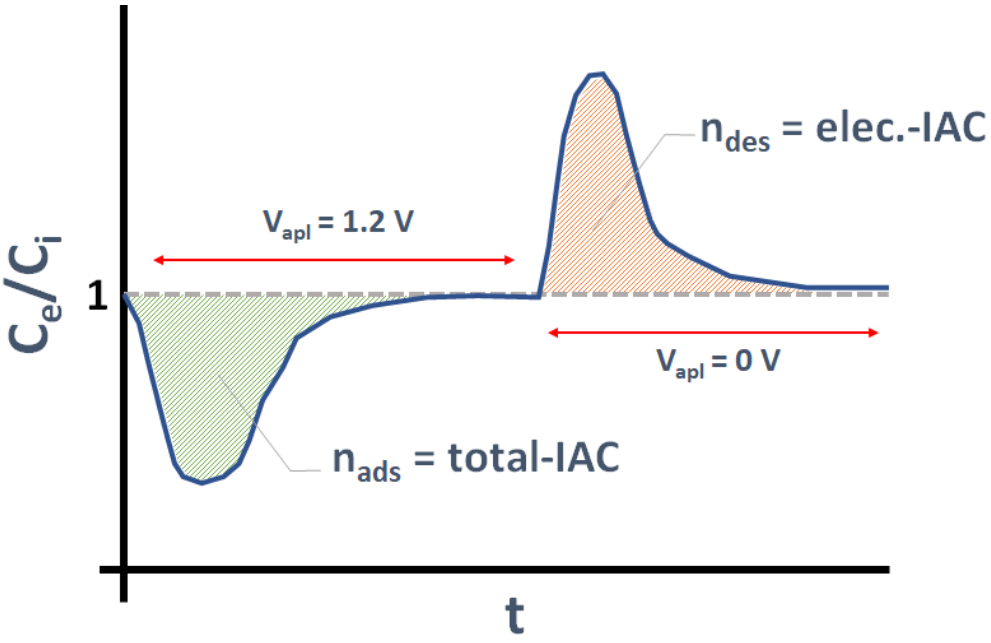

Figure 2.2. Graphical representation of the proposed sampling and calculation strategy for the adsorption capacity in the case of capacitive deionization (CDI) treating organic-containing solution. Ions removed during the charging step contributes to the total adsorption capacity (total-IAC), and ions recovered during the discharging step is equal to electrosorption capacity (elec.-IAC.)

We calculated the number of ions recovered during the discharging step normalized to the electrode mass using the following Eq.2.3, which we defined as *electrosorption-IAC* or elec-IAC:

$$elec - IAC = \frac{v(C_{e,d} - C_i)}{m} \quad \text{.....(2.3)}$$

Where v (mL) is the volume of effluent accumulated from discharging step, C_i and $C_{e,d}$ (mmol/L) are ion concentration of the influent and accumulated effluent after discharging respectively, and m (g) is the total mass of electrodes.

We also used other metrics to report CDI performance: charge efficiency (Λ) and energy-normalized adsorbed ion (*ENAI*). Charge efficiency is the ratio of ions removed over charge transferred in CDI cell, and is calculated as:

$$\Lambda = \frac{F.\Gamma_{elec.}}{\int I(t)dt} \quad (2.4)$$

Where F is the Faraday constant (96,485 C/mol), $\Gamma_{elec.}$ [= $\nu(C_i\text{-}C_e)$] is the total ions adsorbed (mol), and $I(t)$ is the current (A) at time t (sec).

Energy-normalized adsorbed ions (*ENAI*, or *ENAS* for salts, J/mol) represents the adsorbed ions normalized to the energy loss due to resistive loss (linearly proportional to current) and parasitic reactions on the carbon surface [65]. Higher ENAI indicates that the CDI cell is more effective to remove ions with less energy wastage, and can be calculate as:

$$ENAI = \frac{\Gamma_{elec.}}{E_{in}-E_{out}} \quad (2.5)$$

Where E_{in} (J) is the energy input to the cell during charging, and E_{out} (J) is the energy recovered during discharging. Both E_{in} and E_{out} can be calculated using the following equation:

$$E = \Delta V_{cap} \int I(t)dt \quad (2.6)$$

Where ΔV_{cap} (V) is the maximum range of applied voltage between charge and discharge. negatively charged).

2.4.4. Analytical Method

During the experiments, conductivity, pH, and dissolved oxygen (DO) were continuously monitored using a flow-thru conductivity electrode (eDaq, Australia), a pH micro electrode

(eDaq, Australia), and a DO probe (NEOFOX-KIT-Probe, OceanOptics, USA), respectively. To measure carboxylate ion concentrations, we used ion chromatography for anions (ICS-5000$^+$, Thermo Fisher, USA), which was calibrated using standards for each of the targeted anions (primary and secondary standards for formate, acetate, butyrate, hexanoate, and chloride were purchased from Inorganic Ventures (USA) Absolute standards (USA)). The IC was also validated for its smallest detectable changes among our samples using quality controls prepared from secondary standards obtained from another source (Environmental Express, USA) to ensure that changes in carboxylate ions were detectable and not within the percent error of the ICs (± 3%).

2.4.5. Data Visualization and Statistical Methods

All figures generated in this study were created using Origin v2022 (OriginLab Corporation), including any statistical works performed. A p-value less than 0.05 was considered statistically significant. Standard deviations were determined from three replicates of experiments (n = 3)

2.5.Results and Discussion

2.5.1. Electrochemical Characterization of ACC electrodes

We first characterized two electrochemical properties of the ACC electrodes in the presence of each salt: capacitance and resistance. For capacitance, we performed a series of CVs for each of NaHCOO, $NaCH_3COO$, NaC_3H_7COO, $NaC_5H_{11}COO$ (with NaCl as benchmark) at 0.5 M according to the procedure described in Section 2.4.2. The resulting voltammograms for

each ion are presented in **Figure 2.3(A)**. All CV curves exhibit leaf-like quasi-rectangular shapes without obvious redox peaks within the range of applied voltage, demonstrating typical capacitive behavior of CDI electrodes application [66] and stability of carboxylate ions during voltage [67]. The less pronounced rectangular shape of the voltammograms shows there is a resistive behavior involved in the 3-electrode cell setups.

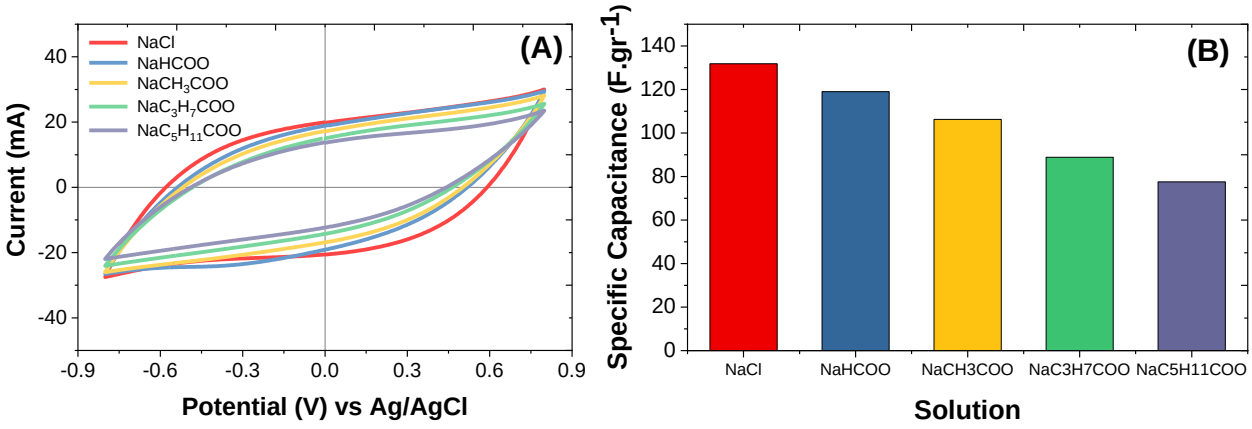

Figure 2.3(A) Cyclic Voltammetry (CV) curves of activated carbon cloth (ACC, Kynol 5092-20) at 5 mV/s scan rate in 0.5 M of different sodium carboxylate solutions and NaCl; (B) Comparison of specific capacitance (F/gr) of ACC in different sodium carboxylate solutions and NaCl.

Integration of the CV curves indicated that the ACC electrodes have a specific capacitance (C_s) of 119.0, 106.2, 88.8, and 77.6 F/g in 0.5 M NaHCOO, $NaCH_3COO$, NaC_3H_7COO, and $NaC_5H_{11}COO$, all of which are smaller than Cs ACC in NaCl at the same concentration (**Figure 2.2(B)**). It is well-characterized that capacitance proportionally correlates to the ion mobility of the electrolyte, and here in this results, the specific capacitance of ACC follows the trend of solution conductivity ($\kappa_{NaCl} > \kappa_{NaHCOO} > \kappa_{NaC3H7COO} > \kappa_{NaC3H7COO} > \kappa_{NaC5H11COO}$), since higher ionic conductivity would lead to a less resistive behavior in the

capacitive setup [68]. Strong correlation was observed between specific capacitance and solution conductivity (See Appendix A.2) In the case of ACC in 0.5 M NaCl, the specific capacitance was observed to be 131.8 F/g which is consistent with previous study using the same electrode material (Kynol ACC 5092-20) [59].

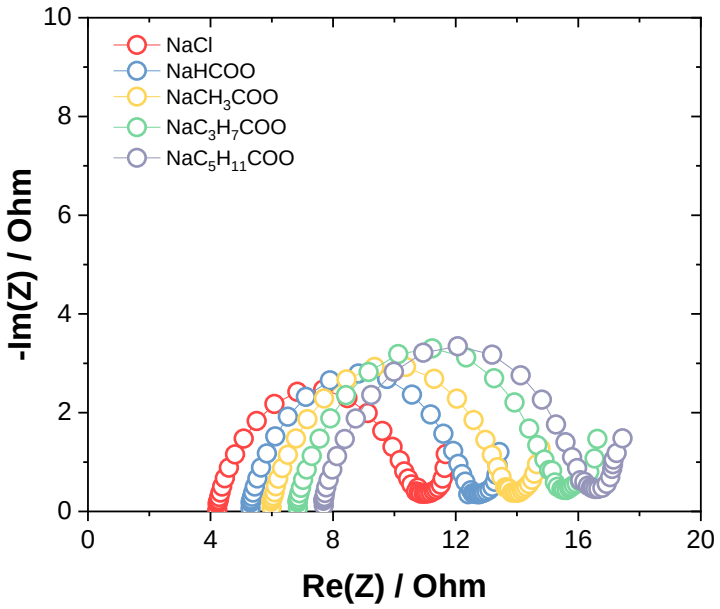

Figure 2.4. The Nyquist impedance plot of ACC Kynol 5092-20 in different organic solution, as measured in a 3-electrode setup

We used electrochemical impedance spectroscopy (EIS) to study the resistance of the ACC in different organic electrolytes. **Figure 2.4** shows the EIS spectra of the ACC in the form of Nyquist plots for each solution. The intercept to the x-axis represents the setup resistance which includes ionic resistance of the solution, electrical resistance of current collectors, and resistance of any wires [69]. Previous studies investigating many aspects of CDI cell resistances found that

typically the electrode ionic resistances were the main contributor to the Ohmic power dissipation of the cell [70,71]. Our results indicated that CDI with NaHCOO has the lowest setup resistance (5.31 Ohm) while $NaC_5H_{11}COO$ the highest among organic solutions (7.69 Ohm), directly correlates to the difference in conductivity. The semi-circle portion attributed to the double layer capacitance between electrode matrix and electrolyte, and in parallel with the internal resistance [69,72–74]. The size of semi-circle indicated the smaller charge transfer resistance, of which NaHCOO has the smallest resistance among all four carboxylates. Charge transfer resistance (RCT) is the main parameter that characterizes the electrochemical process at electrode-electrolyte interface [75], and our results showed that larger resistive force would be expected in a CDI working with longer carboxylate solutions.

2.5.2. Electrosorption of carboxylate ions under polarization

To investigate the electrosorption of carboxylate ions in a CDI experiment, anodic polarization (positive) was applied to the ACC using constant voltage of 1.2 V for 180 min during charging process with another 180 min for 0 V discharging step. During the charging phase for electrode conditioning, we observed the removal of carboxylate ions from bulk solution onto the ACC electrode, as indicated by the change in the effluent conductivity (**Figure 2.5(A)**). Different trend in conductivity profile is observed among the four carboxylate ions, with NaHCOO and $NaCH_3COO$ showed the lowest relative effluent conductivity (normalized with the influent conductivity) at t ~7 min. The 2 smallest carboxylates (together with chloride) showed no significant difference (p-value > 0.05) with regard to the lowest concentrated effluent, especially when compared to butyrate and hexanoate. At the same time, effluent conductivity larger than the influent was observed for CDI treating NaCl, $NaCH_3COO$, and $NaC_5H_{11}COO$,

specifically closer to the end of this charging cycle, indicating more ions were introduced into the effluent. This increase of conductivity could be a result of several events, one of which is parasitic faradaic reaction in the form of hydroxide/proton generation or carbon oxidation due to overpotential which could introduce more ions to the bulk solution [76]. However, relying on conductivity data only may not be the best strategy to understand the occurrence in the system or to calculate adsorption capacity of a complex system such as CDI with organic solution. Therefore, for the calculation of adsorption capacity in this study, we used a more consistent IC measurement to determine ion concentration of the effluent and influent and used these values to calculate more accurate values for the capacity. Another key observation from **Figure 2.5(A)** is the inverse peak observed during the initial charging period, which indicates that there is a sudden increase in number of ions in the system after voltage application. This phenomenon, the release of ions at the beginning of charging process, was also consistently observed in prior studies [76–78] and attributed to the co-ion repulsion from each electrode. The inversion peak is observed to be highest with hexanoate and lowest with formate (and chloride). We argued that, in addition to the co-ion repulsion, this may be attributed to the release of non-electrically (physically or chemically) adsorbed organic ions from the electrode surface due to the change in energy after voltage application, breaking down the bond between ions and surface functional groups. Further studies are needed to confirm this argument.

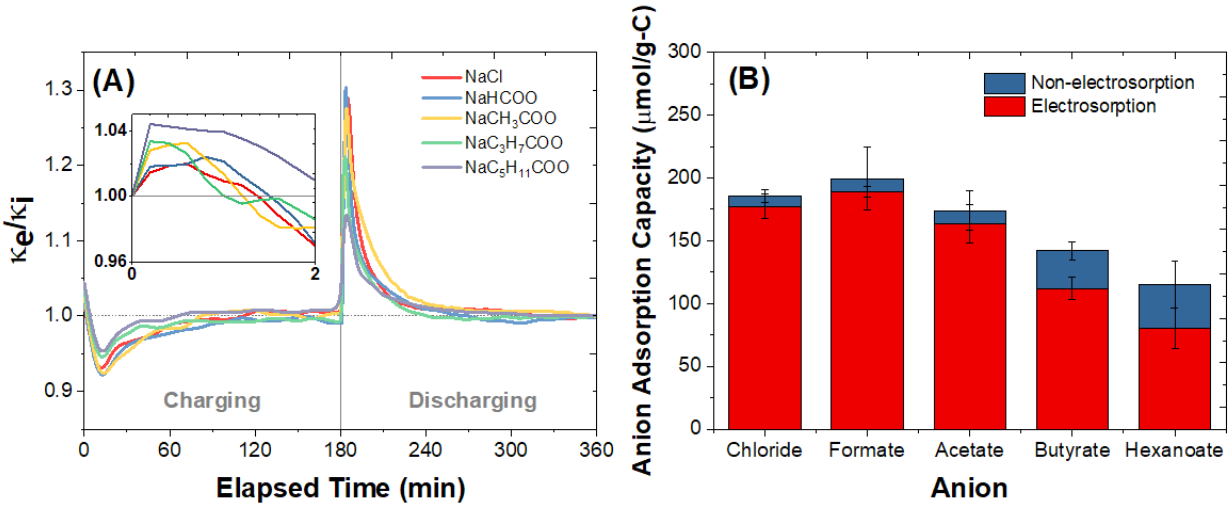

Figure 2.5. (A) Profile of effluent conductivity normalized to the influent conductivity during the three hours charging (E_{apl} = 1.2 V) and three hours discharging (E_{apl} = 0 V) steps for each sodium carboxylate solutions (and sodium chloride) in CDI cell; (B) Ion adsorption capacity for all anions showing contribution from both electrosorption and non-electrostatic interactions. Inset on **Figure 2.5**(A) shows the inverse peak observed during the first 2 mins of charging process. Gray line at 180 min indicates the switch time between charging and discharging steps. Error bars represent a triplicate experiment (n = 3)

The calculated IAC using the Eq. 2.2. for different carboxylate ions are presented in **Figure 2.5**(A), showing both adsorption capacity due to electrostatic force as well as non-electrostatic interaction (e.g., physical or chemical adsorption). At a voltage application of 1.2 V, the total IAC values for ACC treating organic solutions were 199.3 ± 25.0 μmol/g-C for formate, 174.1 ± 16.1 μmol/g-C for acetate, 141.9 ± 6.8 μmol/g-C for butyrate, and 115.5 ± 18.6 μmol/g-C for hexanoate, indicating the larger carboxylates (butyrate, hexanoate) were being adsorbed more in total than smaller carboxylate (formate, acetate) after 180 min charging. As for electrosorption-IAC, the values were 188.9 ± 3.9 μmol/g-C for formate, 163.6 ± 15.1 μmol/g-C for acetate, 112.1 ± 8.8 μmol/g-C for butyrate, and 80.3 ± 16.3 μmol/g-C for hexanoate, corresponding to electrosorption-IAC/total-IAC ratio of 94.8%, 93.9%, 78.9%, and 69.6% for

formate, acetate, butyrate, hexanoate respectively. These results showed consistent trend as observed from the specific capacitance test from section 2.3.1. Theoretically, specific capacitance of an electrode represents the strength of electrostatic force to attract counterions and form the electrical double layer (EDL), as a result, higher specific capacitance means more ions removed from the bulk. Specific capacitance directly correlates to the active surface area of the electrode to electrosorb ions [59]. At the same time, recent experiments have found that carbon-based CDI electrodes showed preference by electrosorbing smaller ions than bigger in the case of equal-valence ions [79], here predicting that among the four carboxylate ions, formate should have been removed the most.

Discussing our adsorption results furthermore, we tried to look deeper into what made the charged ACC electrosorbed less amount of butyrate/hexanoate than smaller carboxylates and chloride proportionally to the overall adsorption capacity (**Figure 2.5(B)**). It is well-characterized that unlike other small, monovalent, inorganic ions (i.e., Cl^-, F^-, NO_3^-), organic ions such as carboxylates also possess additional traits due to its non-polar acyl group on top of the anionic properties from its polar carboxyl end, which more pronounce as the carboxylate chain gets longer. We argued that during the charging process, 3 sorption process simultaneously occurred and together resulted in the removal of organic ions from bulk onto ACC electrodes: 1) electrosorption, of charged species onto electrode's EDL, 2) physical adsorption (i.e., microporosity effect, presence of hydrogen bonds), and 3) chemisorption (i.e., acid-base reactions) [80]. From the study by Lopez-Velandia et al., it can be concluded that the adsorption of carboxylic acid such as acetic and butyric acid from bulk solution would depend on pore structure and the surface chemistry of activated carbon. Specifically, for butyrate (and to a lesser extent, acetate), the presence of longer -R chain resulted in stronger interactions with the surface

functional groups of the ACC electrodes, indicating larger physical adsorption and chemisorption, as observed in the results showed on **Figure 2.5(B)**. Nevertheless, it is still unclear whether it is actually physical adsorption or chemisorption which played a bigger role in butyrate or hexanoate removal, and our knowledge on evaluating each sorption individually from a complex process like adsorption in charged environment such as CDI is still limited. For now, we combined both physical adsorption and chemisorption into a single term, non-electrosorption. In this study, non-electrosorption shall include any other types of sorption that would remove ions from bulk solutions without any electrical assistance.

2.5.3. Cell Voltage Distribution and Electrode Potentials

During the CDI experiments, half-cell electrode potentials over charging and discharging steps were recorded. Ideally, when voltage is applied to the cell (1.2 V) with symmetrical electrodes, it will be distributed almost equally between cathode and anode [81]. During the charging step in this study, the applied voltage was evenly distributed between anode (0.51 ± 0.01 V) and cathode (0.58 ± 0.11 V) in CDI with NaCl, an observation which is consistent with previous works [81,82]. On the other hand, with other larger carboxylate ions (i.e., butyrate and hexanoate), the applied voltage was unevenly distributed, with most of the voltage went to cathode. After 3 hours of 1.2 voltage being applied, the anode potential for hexanoate was steady at around 0.35 V, while cathode reached -0.88 V, which theoretically should favor the occurrence of cathodic Faradaic reactions such as oxygen reduction while minimizing anodic faradaic reactions (i.e., carbon oxidation) [83,84]. This uneven distribution with larger carboxylate only (and not with formate or chloride) highlighted the influence of physically/chemically adsorbed organic ions onto the surface of electrodes (i.e., anode and cathode). The long exposure of ACC as electrodes

to the butyrate and hexanoate solutions means enough ions attached to the surface of carbon materials and modified its properties, particularly its electronegativity, prior to the CDI experiment. Physically/chemically adsorbed organics, known for its negative charged ends, resulted in the ACC surface to be more negatively charged, consequently creating opposite impact on the electrode potentials when the cell is being applied with voltage , i.e., 'accidental' asymmetrical electrodes [58,85–88]. A more negative anode would resist positive voltage, while more negative cathode encourages more voltage distribution. If the ion did not have the properties to let physical or chemical interaction with electrode surface to occur, anode and cathode would not deviate from each other, and the electrodes would have stayed symmetrical.

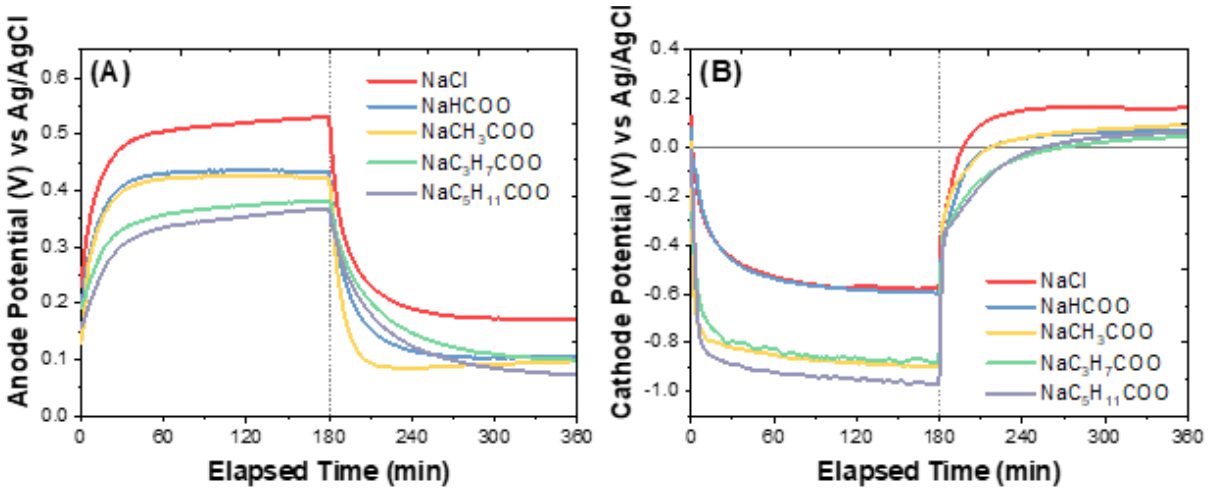

Figure 2.6. Profile of (A) anode half-cell potential and (B) cathode half-cell potential for each of solutions during the charging and discharging steps.

Interestingly, the asymmetrical distribution of electrode potentials in CDI with larger carboxylates means that the uneven adsorption capacity per molar basis between cation (i.e., Sodium) and anion (i.e., carboxylate ions or chloride) shall also be expected. A more negative cathode potential should enhance the cation adsorption while a less positive anode would reduce

the anion adsorption capacity since it is well-characterized that there is a linear positive correlation between electrode potential with the logarithm of the electrosorption capacity [89]. Our results on sodium adsorption capacity versus butyrate/hexanoate adsorption confirmed that per molar basis, sodium was electrosorbed at a higher capacity than butyrate or hexanoate (See Appendix A.4).

2.5.4. Charge Efficiency and Energy-normalized Adsorbed Ions

Charge efficiency is one of the functional metrics that can be used to evaluate the efficiency of CDI system to remove ions. As previously mentioned, in this study we defined the charge efficiency as the ratio between the number of ions electrosorbed to the electric charge and estimated using ions and charge recovered from the discharging process. The average charge efficiency of the CDI in different carboxylate solutions is shown in **Figure 2.7(A)**. Results showed that among the four carboxylate ions, CDI in formate had the highest charge efficiency ($90.15 \pm 3.7\%$) while hexanoate the lowest ($31.35 \pm 0.5\%$). The low charge efficiency on hexanoate indicates most of the charge did not go towards adsorbing the hexanoate via electrostatic force, and likely used to adsorb a smaller anion such as OH as shown by the pH drop during charging process (See **Figure A.4** pH profile)$^{-}$. Overall, the charge efficiency of both butyrate and hexanoate were significantly lower than that of formate or acetate ($p<0.05$). Given the difference in ionic mobility of larger carboxylates, the result is to be expected as charge efficiency is dependent on many factors, one of which is the mobility of charged species in bulk solution, i.e., adsorbing larger ion would be less efficient than small ions. The efficiency would even go lower if we considered the total charge being introduced to the cell during the charging period, as most of it went toward faradaic reactions or was dissipated due to resistive force

instead of ion adsorption (See Appendix A.3 for ratio of component charge). Another possible explanation for the difference in charge efficiency between larger versus smaller carboxylates is the lower anode potential reached when the electrode being charged. The less positive anode potential for butyrate and hexanoate resulted in weaker driving force for the anion adsorption, ultimately reducing the anode charge density [81].

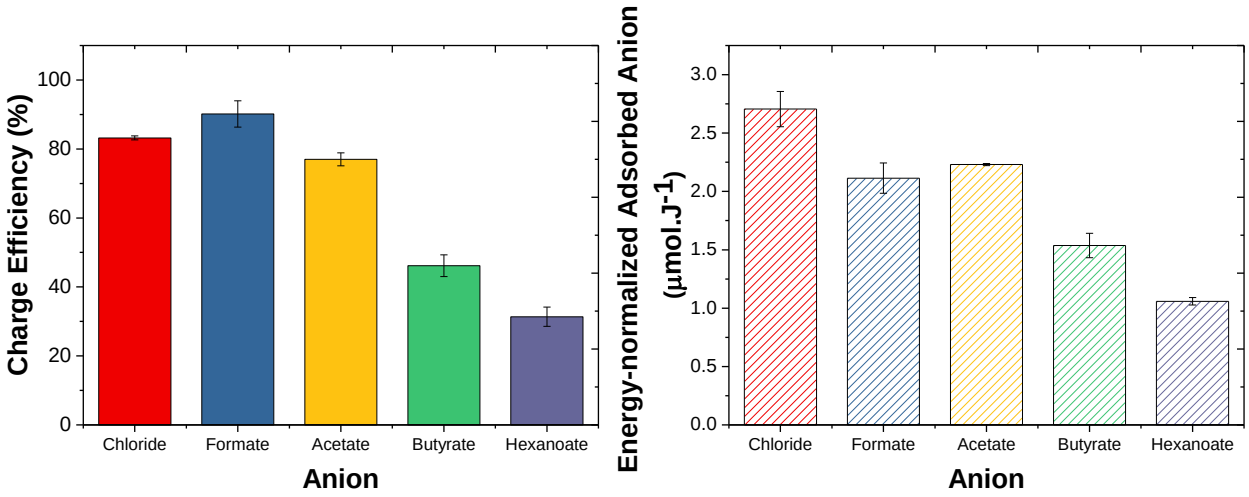

Figure 2.7(A) Charge Efficiency (Λ) and (B) Energy-normalized adsorbed ion (ENAI) of the CDI treating different carboxylate ions and chloride. Error bars represent a triplicate experiment (n = 3)

In previous studies, charge efficiency could also be used for energetic evaluation as it relates to the energy consumption [90]. However, to assess the energy performance of CDI in this work, we proposed using energy-normalized adsorbed ion (ENAI) which is a better indicator of energetic performance as it quantifies the capacity of carboxylate electrosorption per energy losses [41,65]. From our results (**Figure 2.7**(B)), the ENAI for different carboxylates generally followed the same trend as charge efficiency, except for ENAI of acetate being the largest among carboxylates, instead of formate. This result indicates that there were more energy losses per

molar of formate being adsorbed compared to acetate. However, this discrepancy between is not statistically significant ($p>0.05$) and may be a result of cell setup.

2.6.Conclusion

In this study, we examined the performance of capacitive deionization (CDI) cell in treating a range of organic-containing solutions (formate, acetate, butyrate, and hexanoate) and how it behaves differently than typical inorganic ion. To do this, we used a flow-through CDI cell for the adsorption experiment and employed a different strategy to better determine the performance metric when different adsorption mechanisms occurred simultaneously. The strategy was based on the difference in reversibility trait of adsorption processes (i.e., physical, chemical, and electrosorption). Our major conclusions are as follows:

- Activated Carbon Cloth (ACC, Kynol 5092-20) possess a large microporosity and stable electrochemical performance in short-chain carboxylate-containing solution with specific capacitance of 77.6 – 119 F/g.
- In CDI experiment, total ion adsorption capacity for the largest carboxylate, hexanoate, is the lowest among all carboxylate (115.5 ± 18.6 μmol/g-C) while formate is the highest (199.3 ± 25.0 μmol/g-C) with both acetate and butyrate in-between. Possible reasons for the decreased capacity of the carboxylates include higher solution resistance due to lower solution conductivity of equimolar solutions, decrease in anode potential (which decreased the driving force for anion adsorption), and physical/chemisorption which may have negatively impacted electrosorption due to carboxyl group's introduction.

- CDI in hexanoate solution showed a higher proportion of ion adsorbed due to non-electrostatic force, compared to smaller carboxylate ions. The decrease electrosorption-IAC/total-IAC ratio with large carboxylate showed that during the charging step, bigger carboxylate ions were simultaneously interacted with the surface of ACC by means of physical/chemical interaction, in addition to electrosorption. Meanwhile for CDI in smaller carboxylate and inorganic ion (NaCl) solution, electrosorption capacity contributed to the majority (~90%) of total adsorption capacity
- Energetic assessment for CDI for organic solutions showed that charge efficiency decreases as the carboxylate ion getting longer. The energy-normalized adsorbed ions (ENAI) generally followed the same trend as larger carboxylate requires more energy per molar ion adsorbed as it tends to be less efficient in utilizing the energy being applied.

2.7.References

[1] S. Porada, R. Zhao, A. Van Der Wal, V. Presser, P.M. Biesheuvel, Review on the science and technology of water desalination by capacitive deionization, Prog. Mater. Sci. 58 (2013) 1388–1442. doi:10.1016/j.pmatsci.2013.03.005.

[2] L.K.E. Park, S.J. Satinover, S. Yiacoumi, R.T. Mayes, A.P. Borole, C. Tsouris, Electrosorption of organic acids from aqueous bio-oil and conversion into hydrogen via microbial electrolysis cells, Renew. Energy. 125 (2018) 21–31. doi:10.1016/j.renene.2018.02.076.

[3] W. Shi, X. Gao, J. Mao, X. Qian, W. Liu, F. Wu, H. Li, Z. Zeng, J. Shen, X. Cao, Exploration of Energy Storage Materials for Water Desalination via Next-Generation Capacitive Deionization, Front. Chem. 8 (2020) 1–9. doi:10.3389/fchem.2020.00415.

[4] J.G. Gamaethiralalage, K. Singh, S. Sahin, J. Yoon, M. Elimelech, M.E. Suss, P. Liang, P.M. Biesheuvel, R.L. Zornitta, L.C.P.M. De Smet, Recent advances in ion selectivity with capacitive deionization, Energy Environ. Sci. 14 (2021) 1095–1120. doi:10.1039/d0ee03145c.

[5] M.A. Ahmed, S. Tewari, Capacitive deionization: Processes, materials and state of the technology, J. Electroanal. Chem. 813 (2018) 178–192. doi:10.1016/j.jelechem.2018.02.024.

[6] Y.M. Volfkovich, Capacitive Deionization of Water (A Review), Russ. J. Electrochem. 56 (2020) 18–51. doi:10.1134/S1023193520010097.

[7] H. Yoon, J. Lee, S.R. Kim, J. Kang, S. Kim, C. Kim, J. Yoon, Capacitive deionization with Ca-alginate coated-carbon electrode for hardness control, Desalination. 392 (2016)

46–53. doi:10.1016/j.desal.2016.03.019.

[8] P. Nie, B. Hu, X. Shang, Z. Xie, M. Huang, J. Liu, Highly efficient water softening by mordenite modified cathode in asymmetric capacitive deionization, Sep. Purif. Technol. 250 (2020). doi:10.1016/j.seppur.2020.117240.

[9] N. Sun, H. Zhou, H. Zhang, Y. Zhang, H. Zhao, G. Wang, Synchronous removal of tetracycline and water hardness ions by capacitive deionization, J. Clean. Prod. 316 (2021) 128251. doi:10.1016/j.jclepro.2021.128251.

[10] L. Wang, S. Lin, Mechanism of Selective Ion Removal in Membrane Capacitive Deionization for Water Softening, Environ. Sci. Technol. 53 (2019) 5797–5804. doi:10.1021/acs.est.9b00655.

[11] J.H. Choi, B.T. Kim, Hardness removal in membrane capacitive deionization with a selective cation exchange membrane, Desalin. Water Treat. 66 (2017) 97–102. doi:10.5004/dwt.2017.20211.

[12] G. Bharath, A. Hai, K. Rambabu, D. Savariraj, Y. Ibrahim, F. Banat, The fabrication of activated carbon and metal-carbide 2D framework-based asymmetric electrodes for the capacitive deionization of Cr(vi) ions toward industrial wastewater remediation, Environ. Sci. Water Res. Technol. 6 (2020) 351–361. doi:10.1039/c9ew00805e.

[13] S.Y. Huang, C.S. Fan, C.H. Hou, Electro-enhanced removal of copper ions from aqueous solutions by capacitive deionization, J. Hazard. Mater. 278 (2014) 8–15. doi:10.1016/j.jhazmat.2014.05.074.

[14] Z. Huang, L. Lu, Z. Cai, Z.J. Ren, Individual and competitive removal of heavy metals using capacitive deionization, J. Hazard. Mater. 302 (2016) 323–331.

doi:10.1016/j.jhazmat.2015.09.064.

[15] S. Hou, X. Xu, M. Wang, T. Lu, C.Q. Sun, L. Pan, Synergistic conversion and removal of total Cr from aqueous solution by photocatalysis and capacitive deionization, Chem. Eng. J. 337 (2018) 398–404. doi:10.1016/j.cej.2017.12.120.

[16] C.S. Fan, S.Y.H. Liou, C.H. Hou, Capacitive deionization of arsenic-contaminated groundwater in a single-pass mode, Chemosphere. 184 (2017) 924–931. doi:10.1016/j.chemosphere.2017.06.068.

[17] W. Tang, D. He, C. Zhang, T.D. Waite, Optimization of sulfate removal from brackish water by membrane capacitive deionization (MCDI), Water Res. 121 (2017) 302–310. doi:10.1016/j.watres.2017.05.046.

[18] S. Wang, X. Li, H. Zhao, X. Quan, S. Chen, H. Yu, Enhanced adsorption of ionizable antibiotics on activated carbon fiber under electrochemical assistance in continuous-flow modes, Water Res. 134 (2018) 162–169. doi:10.1016/j.watres.2018.01.068.

[19] K. Shi, I. Zhitomirsky, Influence of chemical structure of dyes on capacitive dye removal from solutions, Electrochim. Acta. 174 (2015) 588–595. doi:10.1016/j.electacta.2015.06.029.

[20] D.H. Lee, T. Ryu, J. Shin, J.C. Ryu, K.S. Chung, Y.H. Kim, Selective lithium recovery from aqueous solution using a modified membrane capacitive deionization system, Hydrometallurgy. 173 (2017) 283–288. doi:10.1016/j.hydromet.2017.09.005.

[21] A. Siekierka, M. Bryjak, Selective sorbents for recovery of lithium ions by hybrid capacitive deionization, Desalination. 520 (2021) 115324. doi:10.1016/j.desal.2021.115324.

[22] A. Siekierka, J. Wolska, M. Bryjak, W. Kujawski, Anion-exchange membranes in lithium extraction by means of capacitive deionization system, Desalin. Water Treat. 75 (2017) 331–341. doi:10.5004/dwt.2017.20431.

[23] A. Siekierka, B. Tomaszewska, M. Bryjak, Lithium capturing from geothermal water by hybrid capacitive deionization, Desalination. 436 (2018) 8–14. doi:10.1016/j.desal.2018.02.003.

[24] B. Kim, J.Y. Seo, C.-H. Chung, Electrochemical Desalination and Recovery of Lithium from Saline Water upon Operation of a Capacitive Deionization Cell Combined with a Redox Flow Battery, ACS ES&T Water. 1 (2021) 1047–1054. doi:10.1021/acsestwater.1c00014.

[25] S. Sahin, H. Zuilhof, R.L. Zornitta, L.C.P.M. de Smet, Enhanced monovalent over divalent cation selectivity with polyelectrolyte multilayers in membrane capacitive deionization via optimization of operational conditions, Desalination. 522 (2022) 115391. doi:10.1016/j.desal.2021.115391.

[26] X. Zhang, K. Zuo, X. Zhang, C. Zhang, P. Liang, Selective ion separation by capacitive deionization (CDI) based technologies: A state-of-the-art review, Environ. Sci. Water Res. Technol. 6 (2020) 243–257. doi:10.1039/c9ew00835g.

[27] D.I. Oyarzun, A. Hemmatifar, J.W. Palko, M. Stadermann, J.G. Santiago, Ion selectivity in capacitive deionization with functionalized electrode: Theory and experimental validation, Water Res. X. 1 (2018) 100008. doi:10.1016/j.wroa.2018.100008.

[28] A. Amiri, M. Shanbedi, M. Savari, B.T. Chew, S.N. Kazi, Cadmium ion sorption from aqueous solutions by high surface area ethylenediaminetetraacetic acid- and diethylene

triamine pentaacetic acid-treated carbon nanotubes, RSC Adv. 5 (2015) 71144–71152. doi:10.1039/c5ra08945j.

[29] L. Xu, C. Yu, Y. Mao, Y. Zong, B. Zhang, H. Chu, D. Wu, Can flow-electrode capacitive deionization become a new in-situ soil remediation technology for heavy metal removal?, J. Hazard. Mater. 402 (2021). doi:10.1016/j.jhazmat.2020.123568.

[30] T. Wang, C. Zhang, L. Bai, B. Xie, Z. Gan, J. Xing, G. Li, H. Liang, Scaling behavior of iron in capacitive deionization (CDI) system, Water Res. 171 (2020) 115370. doi:10.1016/j.watres.2019.115370.

[31] J. Chang, F. Duan, H. Cao, K. Tang, C. Su, Y. Li, Superiority of a novel flow-electrode capacitive deionization (FCDI) based on a battery material at high applied voltage, Desalination. 468 (2019). doi:10.1016/j.desal.2019.114080.

[32] L. Lin, J. Hu, J. Liu, X. He, B. Li, X.Y. Li, Selective Ammonium Removal from Synthetic Wastewater by Flow-Electrode Capacitive Deionization Using a Novel K2Ti2O5-Activated Carbon Mixture Electrode, Environ. Sci. Technol. 54 (2020) 12723–12731. doi:10.1021/acs.est.0c04383.

[33] P. Nativ, O. Lahav, Y. Gendel, Separation of divalent and monovalent ions using flow-electrode capacitive deionization with nanofiltration membranes, Desalination. 425 (2018) 123–129. doi:10.1016/j.desal.2017.10.026.

[34] Z. Ge, X. Chen, X. Huang, Z.J. Ren, Capacitive deionization for nutrient recovery from wastewater with disinfection capability, Environ. Sci. Water Res. Technol. 4 (2018) 33–39. doi:10.1039/c7ew00350a.

[35] L. Chen, C. Wang, S. Liu, L. Zhu, Investigation of adsorption/desorption behavior of

Cr(VI) at the presence of inorganic and organic substance in membrane capacitive deionization (MCDI), J. Environ. Sci. (China). 78 (2019) 303–314. doi:10.1016/j.jes.2018.11.005.

[36] M.S. Gaikwad, C. Balomajumder, Simultaneous electrosorptive removal of chromium(VI) and fluoride ions by capacitive deionization (CDI): Multicomponent isotherm modeling and kinetic study, Sep. Purif. Technol. 186 (2017) 272–281. doi:10.1016/j.seppur.2017.06.017.

[37] T. Alfredy, Y.A.C. Jande, T. Pogrebnaya, Removal of lead ions from water by capacitive deionization electrode materials derived from chicken feathers, J. Water Reuse Desalin. 9 (2019) 282–291. doi:10.2166/wrd.2019.074.

[38] R. Rajumon, S.P. Aravind, S. Bhuvaneshwari, J. Ranjitha, P. Mohanraj, Removal of cadmium heavy metal ions from wastewater by electrosorption using modified activated carbon felt electrodes, Water Sci. Technol. 82 (2020) 1430–1444. doi:10.2166/wst.2020.425.

[39] X. Xu, J. Tang, Y.V. Kaneti, H. Tan, T. Chen, L. Pan, T. Yang, Y. Bando, Y. Yamauchi, Unprecedented capacitive deionization performance of interconnected iron-nitrogen-doped carbon tubes in oxygenated saline water, Mater. Horizons. 7 (2020) 1404–1412. doi:10.1039/c9mh01829h.

[40] M. Qin, A. Deshmukh, R. Epsztein, S.K. Patel, O.M. Owoseni, W.S. Walker, M. Elimelech, Comparison of energy consumption in desalination by capacitive deionization and reverse osmosis, Desalination. 455 (2019) 100–114. doi:10.1016/j.desal.2019.01.003.

[41] L. Wang, J.E. Dykstra, S. Lin, Energy Efficiency of Capacitive Deionization, Environ.

Sci. Technol. 53 (2019) 3366–3378. doi:10.1021/acs.est.8b04858.

[42] X. Liu, S. Shanbhag, T. V. Bartholomew, J.F. Whitacre, M.S. Mauter, Cost Comparison of Capacitive Deionization and Reverse Osmosis for Brackish Water Desalination, ACS ES&T Eng. 1 (2021) 261–273. doi:10.1021/acsestengg.0c00094.

[43] P. Sharan, T.J. Yoon, S.M. Jaffe, T. Ju, R.P. Currier, A.T. Findikoglu, Can capacitive deionization outperform reverse osmosis for brackish water desalination?, Clean. Eng. Technol. 3 (2021) 100102. doi:10.1016/j.clet.2021.100102.

[44] A. Kalfa, B. Shapira, A. Shopin, I. Cohen, E. Avraham, D. Aurbach, Capacitive deionization for wastewater treatment: Opportunities and challenges, Chemosphere. 241 (2020) 125003. doi:10.1016/j.chemosphere.2019.125003.

[45] T. Wang, H. Liang, L. Bai, X. Zhu, Z. Gan, J. Xing, G. Li, T.M. Aminabhavi, Adsorption behavior of powdered activated carbon to control capacitive deionization fouling of organic matter, Chem. Eng. J. 384 (2020) 123277. doi:10.1016/j.cej.2019.123277.

[46] L.Y. Lee, H.Y. Ng, S.L. Ong, J.Y. Hu, G. Tao, K. Kekre, B. Viswanath, W. Lay, H. Seah, Ozone-biological activated carbon as a pretreatment process for reverse osmosis brine treatment and recovery, Water Res. 43 (2009) 3948–3955. doi:10.1016/j.watres.2009.06.016.

[47] L. Xu, Y. Xie, Y. Zong, Y. Mao, B. Zhang, H. Chu, D. Wu, Formic acid recovery from EDTA wastewater using coupled ozonation and flow-electrode capacitive deionization (Ozo / FCDI): Performance assessment at high cell voltage, Sep. Purif. Technol. 254 (2021) 117613. doi:10.1016/j.seppur.2020.117613.

[48] S. Chowdhury, N. Khan, G.H. Kim, J. Harris, P. Longhurst, N.S. Bolan, Zeolite for

Nutrient Stripping From Farm Effluents, Elsevier Inc., 2016. doi:10.1016/B978-0-12-803837-6.00022-6.

[49] F.L. Xu, S.E. Jorgensen, Y. Shimizu, E. Silow, Persistent organic pollutants in fresh water ecosystems, Sci. World J. 2013 (2013) 2–4. doi:10.1155/2013/303815.

[50] E. Bayram, E. Ayranci, Electrochemically Enhanced Removal of Polycyclic Aromatic Basic Dyes from Dilute Aqueous Solutions by Activated Carbon Cloth Electrodes, 44 (2010) 6331–6336.

[51] E. Bayram, E. Ayranci, Electrosorption based waste water treatment system using activated carbon cloth electrode : Electrosorption of benzoic acid from a flow-through electrolytic cell, Sep. Purif. Technol. 86 (2012) 113–118. doi:10.1016/j.seppur.2011.10.032.

[52] S. Porada, G. Feng, M.E. Suss, V. Presser, Capacitive deionization in organic solutions: Case study using propylene carbonate, RSC Adv. 6 (2016) 5865–5870. doi:10.1039/c5ra20786j.

[53] A. Ban, A. Schafer, H. Wendt, Fundamentals of electrosorption on activated carbon for wastewater treatment of industrial effluents, J. Appl. Electrochem. 28 (1998) 227–236. doi:10.1023/a:1003247229049.

[54] C.A. Contreras-Dávila, N. Nadal Alemany, C. Garcia-Saravia Ortiz-de-Montellano, Z. Bao, C.J.N. Buisman, D.P.B.T.B. Strik, Designing a Selective n -Caproate Adsorption–Recovery Process with Granular Activated Carbon and Screening of Conductive Materials in Chain Elongation , ACS ES&T Eng. 2 (2022) 54–64. doi:10.1021/acsestengg.1c00214.

[55] C. López-Velandia, J. Moreno-Barbosa, R. Sierra-Ramirez, L. Giraldo, J. Moreno-Piraján,

Adsorption of volatile carboxylic acids on activated carbon synthesized from watermelon shells, Adsorpt. Sci. Technol. 32 (2014) 227–242. doi:10.1260/0263-6174.32.2-3.227.

[56] M.W. Ryoo, G. Seo, Improvement in capacitive deionization function of activated carbon cloth by titania modification, Water Res. 37 (2003) 1527–1534. doi:10.1016/S0043-1354(02)00531-6.

[57] E.N. Guyes, T. Malka, M.E. Suss, Enhancing the ion-size-based selectivity of capacitive deionization electrodes, Environ. Sci. Technol. 53 (2019) 8447–8454. doi:10.1021/acs.est.8b06954.

[58] C. Kim, P. Srimuk, J. Lee, S. Fleischmann, M. Aslan, V. Presser, Influence of pore structure and cell voltage of activated carbon cloth as a versatile electrode material for capacitive deionization, Carbon N. Y. 122 (2017) 329–335. doi:10.1016/j.carbon.2017.06.077.

[59] M. Aslan, M. Zeiger, N. Jäckel, I. Grobelsek, D. Weingarth, V. Presser, Improved capacitive deionization performance of mixed hydrophobic/hydrophilic activated carbon electrodes, J. Phys. Condens. Matter. 28 (2016). doi:10.1088/0953-8984/28/11/114003.

[60] A.A. Ensafi, N. Ahmadi, B. Rezaei, Electrochemical preparation and characterization of a polypyrrole/nickel-cobalt hexacyanoferrate nanocomposite for supercapacitor applications, RSC Adv. 5 (2015) 91448–91456. doi:10.1039/c5ra17945a.

[61] E.N. Guyes, T. Malka, M.E. Suss, Enhancing the ion-size-based selectivity of capacitive deionization electrodes, Environ. Sci. Technol. 53 (2019) 8447–8454. doi:10.1021/acs.est.8b06954.

[62] N. Holubowitch, A. Omosebi, X. Gao, J. Landon, K. Liu, Quasi-Steady-State Polarization

Reveals the Interplay of Capacitive and Faradaic Processes in Capacitive Deionization, ChemElectroChem. 4 (2017) 2404–2413. doi:10.1002/celc.201700082.

[63] Y. Bouhadana, M. Ben-Tzion, A. Soffer, D. Aurbach, A control system for operating and investigating reactors: The demonstration of parasitic reactions in the water desalination by capacitive de-ionization, Desalination. 268 (2011) 253–261. doi:10.1016/j.desal.2010.10.037.

[64] A. Hemmatifar, J.W. Palko, M. Stadermann, J.G. Santiago, Energy breakdown in capacitive deionization, Water Res. 104 (2016) 303–311. doi:10.1016/j.watres.2016.08.020.

[65] W. Tang, D. He, C. Zhang, P. Kovalsky, T.D. Waite, Comparison of Faradaic reactions in capacitive deionization (CDI) and membrane capacitive deionization (MCDI) water treatment processes, 120 (2017). doi:10.1016/j.watres.2017.05.009.

[66] C.O. Ania, F. Béguin, Mechanism of adsorption and electrosorption of bentazone on activated carbon cloth in aqueous solutions, Water Res. 41 (2007) 3372–3380. doi:10.1016/j.watres.2007.03.031.

[67] N. Jäckel, S. Patrick Emge, B. Krüner, B. Roling, V. Presser, Quantitative Information about Electrosorption of Ionic Liquids in Carbon Nanopores from Electrochemical Dilatometry and Quartz Crystal Microbalance Measurements, J. Phys. Chem. C. 121 (2017) 19120–19128. doi:10.1021/acs.jpcc.7b06915.

[68] Y. Qu, T.F. Baumann, J.G. Santiago, M. Stadermann, Characterization of Resistances of a Capacitive Deionization System, Environ. Sci. Technol. 49 (2015) 9699–9706. doi:10.1021/acs.est.5b02542.

[69] B. van Limpt, Performance relations in Capacitive Deionization systems, 2010. http://edepot.wur.nl/154085.

[70] H.A. Kuo, A. Ramachandran, D.I. Oyarzun, E.C. Clevenger, J.G. Santiago, M. Stadermann, P.G. Campbell, S.A. Hawks, Understanding resistances in capacitive deionization devices, Environ. Sci. Water Res. Technol. 6 (2020) 1842–1854. doi:10.1039/d0ew00169d.

[71] J.E. Dykstra, R. Zhao, P.M. Biesheuvel, A. Van der Wal, Resistance identification and rational process design in Capacitive Deionization, Water Res. 88 (2016) 358–370. doi:10.1016/j.watres.2015.10.006.

[72] X. Liu, S. Shanbhag, S. Natesakhawat, J.F. Whitacre, M.S. Mauter, Performance Loss of Activated Carbon Electrodes in Capacitive Deionization: Mechanisms and Material Property Predictors, Environ. Sci. Technol. 54 (2020) 15516–15526. doi:10.1021/acs.est.0c06549.

[73] H.H. Kyaw, M.T.Z. Myint, S. Al-Harthi, M. Al-Abri, Removal of heavy metal ions by capacitive deionization: Effect of surface modification on ions adsorption, J. Hazard. Mater. 385 (2020). doi:10.1016/j.jhazmat.2019.121565.

[74] L.G. Zamfir, M. Puiu, C. Bala, Advances in electrochemical impedance spectroscopy detection of endocrine disruptors, Sensors (Switzerland). 20 (2020) 1–21. doi:10.3390/s20226443.

[75] Y. Algurainy, D.F. Call, Asymmetrical removal of sodium and chloride in fl ow-through capacitive deionization, Water Res. 183 (2020) 116044. doi:10.1016/j.watres.2020.116044.

[76] A. Omosebi, X. Gao, J. Landon, K. Liu, Asymmetric electrode configuration for enhanced membrane capacitive deionization, ACS Appl. Mater. Interfaces. 6 (2014) 12640–12649. doi:10.1021/am5026209.

[77] I. Cohen, E. Avraham, Y. Bouhadana, A. Soffer, D. Aurbach, The effect of the flow-regime, reversal of polarization, and oxygen on the long term stability in capacitive de-ionization processes, Electrochim. Acta. 153 (2015) 106–114. doi:10.1016/j.electacta.2014.12.007.

[78] M.E. Suss, Size-Based Ion Selectivity of Micropore Electric Double Layers in Capacitive Deionization Electrodes, J. Electrochem. Soc. 164 (2017) E270–E275. doi:10.1149/2.1201709jes.

[79] C. López-velandia, J.J. Moreno-barbosa, R. Sierra-ramirez, Adsorption of Volatile Carboxylic Acids on Activated Carbon Synthesized from Watermelon Shells, (2014) 227–242. doi:10.1260/0263-6174.32.2-3.227.

[80] Y. Algurainy, D.F. Call, Improving Long-Term Anode Stability in Capacitive Deionization Using Asymmetric Electrode Mass Ratios, ACS ES&T Eng. 2 (2022) 129–139. doi:10.1021/acsestengg.1c00348.

[81] Z. Sun, L. Chai, M. Liu, Y. Shu, Q. Li, Y. Wang, D. Qiu, Effect of the electronegativity on the electrosorption selectivity of anions during capacitive deionization, Chemosphere. 195 (2018) 282–290. doi:10.1016/j.chemosphere.2017.12.031.

[82] W. Tang, D. He, C. Zhang, P. Kovalsky, T.D. Waite, Comparison of Faradaic reactions in capacitive deionization (CDI) and membrane capacitive deionization (MCDI) water treatment processes, Water Res. 120 (2017) 229–237. doi:10.1016/j.watres.2017.05.009.

[83] C. Zhang, D. He, J. Ma, W. Tang, T.D. Waite, Comparison of faradaic reactions in flow-through and flow-by capacitive deionization (CDI) systems, Electrochim. Acta. 299 (2019) 727–735. doi:10.1016/j.electacta.2019.01.058.

[84] T. Wu, G. Wang, Q. Dong, B. Qian, Y. Meng, J. Qiu, Asymmetric capacitive deionization utilizing nitric acid treated activated carbon fiber as the cathode, Electrochim. Acta. 176 (2015) 426–433. doi:10.1016/j.electacta.2015.07.037.

[85] G. Peng, F. Gramm, C. Ludwig, F. Vogel, Effect of carbon surface functional groups on the synthesis of Ru/C catalysts for supercritical water gasification, Catal. Sci. Technol. 5 (2015) 3658–3666. doi:10.1039/c5cy00352k.

[86] I. Cohen, E. Avraham, M. Noked, A. Soffer, D. Aurbach, Enhanced charge efficiency in capacitive deionization achieved by surface-treated electrodes and by means of a third electrode, J. Phys. Chem. C. 115 (2011) 19856–19863. doi:10.1021/jp206956a.

[87] Y.J. Oh, J.J. Yoo, Y. Il Kim, J.K. Yoon, H.N. Yoon, J.H. Kim, S. Bin Park, Oxygen functional groups and electrochemical capacitive behavior of incompletely reduced graphene oxides as a thin-film electrode of supercapacitor, Electrochim. Acta. 116 (2014) 118–128. doi:10.1016/j.electacta.2013.11.040.

[88] Z. Sun, L. Chai, M. Liu, Y. Shu, Q. Li, Y. Wang, D. Qiu, Effect of the electronegativity on the electrosorption selectivity of anions during capacitive deionization, Chemosphere. 195 (2018) 282–290. doi:10.1016/j.chemosphere.2017.12.031.

[89] M.E. Suss, S. Porada, X. Sun, P.M. Biesheuvel, J. Yoon, V. Presser, Water desalination via capacitive deionization: What is it and what can we expect from it?, Energy Environ. Sci. 8 (2015) 2296–2319. doi:10.1039/c5ee00519a.

Chapter 3: Elucidating the Contribution of Different Adsorption Processes of Organic Ions and Their Impacts on Electrode Properties and Performances of Capacitive Deionization (CDI) Cell

3.1. Abstract

Capacitive deionization (CDI) is an electrochemical method of removing ions from aqueous solutions. The primary application of CDI is desalination of brackish water. As a result, most research has focused on removing inorganic ions, namely Na^+ and Cl^-. CDI may also be useful to remove organic ions, including pollutants (e.g., per- and polyfluoroalkyl substances) and high-value chemicals [e.g., volatile fatty acids (VFAs)]. Removal of many organic ions is not as straightforward as small, inorganic ions, especially when activated carbon (AC) electrodes are used. Some organic ions can physically and/or chemically adsorb to the AC in the absence of an applied potential. Under voltage application, the process becomes more complex with the role of electrical double layer (EDL) capacitance. Toward understanding the complex interplay of different adsorptive processes occurring simultaneously and fundamental factors controlling organic ion removal, we investigated four organic ions that varied only by carbon chain length in flow-through CDI cells using AC cloth (ACC) electrodes. Formate, acetate, butyrate, and hexanoate (common VFAs generated in many anaerobic microbial processes) were selected as representative monovalent organics and chloride as an inorganic ion. We used three different operational conditions to elucidate the contributions of electro- and non-electro-sorptive processes: electrosorption onto a pristine electrode (PR-E), electrosorption onto electrodes

saturated with ions (ST-E), and electrosorption onto electrodes pre-conditioned through multiple CDI cycles (CD-E). From these tests, we propose a new approach to calculate adsorption capacity due to electrosorption or non-electrosorption processes. We found that CDI with PR-E held under a constant 1.2 V adsorbed hexanoate the most, with total ion adsorption capacity (IAC) of 0.89 ± 0.06 mmol/g-C, 86.8% of which is due to physical/chemisorption. Meanwhile formate-CDI with PR-E removed the ion with total IAC of 0.49 ± 0.07 mmol/g-C, with physisorption/chemisorption contributed slightly more than electrosorption (58% vs 42%). In contrast, for the electrodes which were first conditioned through multiple charge/discharge cycles (CD-E), total IAC decreased for all ions with electrosorption now becoming the predominant mechanism of adsorption. No significant difference in IAC was observed between formate (0.19 ± 0.03 mmol/g-C), acetate (0.17 ± 0.02 mmol/g-C), and chloride ions (0.18 ± 0.00 mmol/g-C); of which >90% was due to electrosorption. Moreover, in CDI treating bigger carboxylate (butyrate and hexanoate), physical/chemisorption still contributed 20-30% of total IAC. For CDI with ST-E, the majority of formate, acetate, and chloride adsorbed through electrosorption (71-81%), while butyrate and hexanote, both electrosorption and non-electrosorption interaction contribute relatively equal to total IAC. In this study, we also tested the impact of ACC interaction with different organic ions on electrode structural, chemical, and electrical properties. We investigated the change in pores volume (v_{mi}), chemical charge concentration (σ_{chem}), as well as potential of zero charg (E_{pzc}). We found that saturating ACC electrodes with hexanoate ions affected electrosorption capacity by reducing available micropores volume for adsorption sites resulting in lower adsorption capacity. Meanwhile, no significant change in pores volume and surface area were observed for ACC saturated with formate or chloride. We also found that physical/chemisorption of hexanoate ions onto ACC

surface modified the σ_{chem} significantly, resulting in a more negatively charged surface. We did not find a strong correlation between types of carboxylates with E_{pzc} as it was not enough to shift E_{pzc} without potential-driven or chemically induced surface oxidation. These results highlighted that the physical and chemical adsorptive behavior of organic ions can have a strong influence on the electrosorption of ions in CDI relative to the electrode structural, chemical, and electrical properties. Our finding also revealed certain dynamic of different adsorption mechanisms for organic ions occurring in CDI relevant to different electrode conditions.

3.2. Significance

This work will provide insights on the contribution of different adsorption mechanisms in CDI treating organic ions and how its occurrence impacts the electrode properties and overall performance of CDI

3.3. Introduction

Capacitive deionization (CDI) has been receiving great attention for its potential for broad application in water and wastewater treatment. It is an emerging technology that utilizes the principle of electrosorption of ions onto porous carbon-based electrodes that is already proven to be a promising option for brackish water desalination [1,2], but also has the potential to be an alternative technology for water softening and selective ion recovery [3].

With the goal to realize CDI as a commercially available technology for water industry, notable efforts have been made in recent years to expand the use of electrochemically mediated separation not only for contaminant removal process but also for the recovery of valued charged

chemicals in food, biotechnology, or textile industries [4–8]. Organic ions, such as carboxylates (-COO-), sulfonates (-SO3-), are also typically present in wastewater as contaminants of concern for agricultural intake or drinking water sources, thus removing these ions from water is another challenge that must be addressed from environmental perspective.

Previous studies on the use of electrosorptive process to recover valuable organic ions from water typically focused on finding the best strategy to selectively remove or improve the adsorption capacity by selecting different electrode materials, modifying carbon functionalization, employing asymmetric faradaic electrodes, or using organic-selective membrane [5,9–11]. However, little is known about dynamic of adsorption processes in CDI treating complex organic ions, which behave differently than of inorganic ions, especially on the commonly used and low-cost activated carbon-based electrodes.

Non-electrochemical-based adsorption of organic ions onto the surface of activated carbon is widely used process and has been extensively investigated for many years due to its highly efficient process because of AC's high specific area, surface reactivity, porous structure, as well as versatile pore size distribution [12–15]. Organic species in aqueous phase adsorb easily onto the surface of activated carbon by means of both electrostatic and non-electrostatic interactions, which is mainly controlled by the structural integrity and the presence of oxygen-containing surface functional groups, both basic and acidic (Belhachemi, 2021). Overall, physical and chemical interactions are the main factors for AC's ability to adsorb a large number of organic species.

Activated carbon is also commonly used electrode materials for capacitive deionization due to its high capacitive properties from its abundant micropores for electrical double layer (EDL) formation, relatively low cost, and flexibility for surface modification [16]. Several studies have

looked into the use of activated carbon electrodes to remove organic species from water using CDI cell [5,10,11].

Previous studies have shown that there are several known adsorption mechanisms of ion removal that occur during CDI experiments: (1) physical adsorption due to affinity between ion and ACC surface (e.g., van der Waals force, H-bonding, etc), which is reversible only using external force [17], (2) chemical adsorption (chemisorption) which is accompanied with chemical reactions and irreversible, and (3) electrosorption due to electrical double layer (EDL) capacitance [18–20]. However, knowledge gaps still exist with regard to the adsorption of organic species onto the surface of carbon electrodes in CDI. Physical and chemical adsorption of organic ion onto ACs are well-characterized in a potential-free environment, while electrosorptive ability of AC electrode in CDI is extensively studied. However, the contribution of physical, chemical, and electrosorption of organic ions onto the surface of carbon electrode is not yet well-understood. Non-electrosorptive interaction has been investigated in several studies: Ryoo & Seo (2003) noted the occurrence of physical adsorption of NaCl in CDI with AC electrode and developed a strategy to minimize its impact by modifying the ACC with titania, while Liu et al., (2016) tried to quantify the individual amount of physical adsorption and electrosorption of organic species by running the CDI at open circuit voltage [18]. A study by Ge et al., (2017) differentiated the physical adsorption from electrosrption by soaking the electrodes into feed solution thus saturating carbon materials of physical adsorption before voltage application commenced [21]. Most CDI studies that acknowledged the contribution of physical adsorption typically quantify the capacity under no voltage condition, independent from electrosorption capacity. However, it is not well understood the dynamic of the contribution from different adsorption mechanisms occurring simultaneously during charging of the CDI.

In this study, we looked at the contribution of different adsorption mechanisms when they simultaneously take place under voltage applications and how they behaved differently across different carboxylate (and chloride) ions, as well as different electrode conditions. We proposed new approach to quantify physical/chemisorption and electrosorption capacity by measuring how much ions being removed from the bulk during voltage application (charging) versus how much ions can be recovered back in the bulk after the voltage application stops (discharging). In ideal scenario, quantifying each physical and chemisorption separately would provide a clearer answer to the objective. However, in this study we combined these two terms into single category: non-electrosorption. We selected four different monovalent carboxylates: formate ($HCOO^-$), acetate (CH_3COO^-), butyrate ($C_3H_7COO^-$), and hexanoate ($C_5H_{11}COO^-$) to systematically investigate the adsorption mechanisms and how it varies across different ion within the same group, as well as chloride as inorganic benchmark. All carboxylate-containing solutions were made from their respective sodium salts, ensuring identical cations thus minimizing uncertainty so the focus of study remains on different anions of interest. In addition to the charged species, adsorption capacity of ACs in CDI also depend on the electrode conditions. Therefore, we investigated the impact of electrode conditions on the overall adsorption process. We selected three different electrode conditions based on their pre-treatment: pristine electrode (PR-E), previously saturated electrode (ST-E), and previously conditioned electrode (CD-E). These three different electrode conditions highlighted the markedly variation in physical and chemical properties of electrodes and how they may impact the overall performance of CDI. We tested these electrodes in typical charging-discharging sequence of CDI and measure the change in contribution from each of the adsorption mechanisms as well as the overall performance. To further explained the anticipated difference in CDI performance across carboxylates with different electrode conditions, we

looked at the impact of the electrode pre-treatment on the structural, chemical, and electrical properties of the electrodes and used the information to make correlation.

3.4. Experimental Section

3.4.1. CDI Operation

This study focused on the dynamics of organic ion adsorption processes in a CDI cell when a voltage is applied. Different electrode pretreatments were included to understand how the ions removed when an electrode was pristine, saturated with the target ion, and conditioned under typical CDI operational cycles. The three different pretreatments were (**Figure 3.1**):

1) Pristine electrodes (PR-E): Pretreatment of the ACC by flowing deionized water through pristine ACC for 1 hour at 3 mL/min flow rate to remove impurities
2) Saturated electrodes (ST-E): First, the electrodes were treated identical to the PR-E pretreatment. Then the target ion was continuously flushed through the electrodes (3 mL/min for 12 hours) without an applied voltage in order to saturate the electrodes with the ion.
3) Conditioned electrodes (CD-E): First, the electrodes were treated identical to the ST-E pretreatment. Then the electrodes were subjected to 12 cycles of 1.2 V-charging / 0V-discharging cycles prior to the extended charge/discharge cycle.

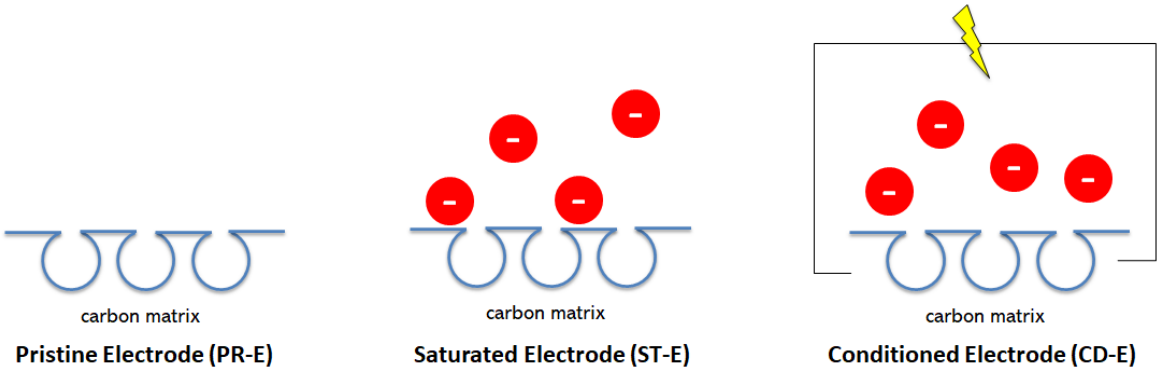

Figure 3.1. Schematic representation of the three electrode conditions tested for CDI experiments in this study

All experiments were performed using the same CDI cell setup and feed solution. The salt was the only variable (four carboxylates and NaCl). A target concentration of 0.05 M was used in all tests. CDI experiments were performed on each of three different electrode conditions and were carried out with the same sequences: 1.2 V charging for 3 hours, followed by 0 V discharging for 3 hours. Effluent samples were each collected for both charging and discharging to measure the ion concentrations.

To investigate the impact of our pretreatments, we focused on three different parameters of electrodes which are commonly investigated as contributing factors to CDI performance: structural, chemical, and electrical properties. In this study, the structural property was assessed by calculating the pores volume (v_{mi}) and pore size distribution, chemical property was represented by chemical charge concentration (σ_{chem}), and electrical properties was represented by potential of zero-charge (E_{pzc}).

We reported several parameters as performance metrics. We calculated ion adsorption capacity (IAC) using two different methods. First, we calculated the number of ions removed

during the charging step normalized to the electrode mass using Eq.3.1, later we defined this adsorption capacity as *total-IAC*:

$$total\ IAC = \frac{v(C_i - C_{e,c})}{m} \quad \text{.....(3.1)}$$

Where *v* (mL) is the volume of effluent accumulated from the charging step, C_i and $C_{e,c}$ (mmol/L) are the influent and effluent ion concentration after charging, and *m* (g) is the total mass of electrodes.

We calculated the number of ions recovered during the discharging step normalized to the electrode mass using the following Eq.3.2, which we defined as *electrosorption IAC* or *elec-IAC*:

$$electrosorption\ IAC = \frac{v(C_{e,d} - C_i)}{m} \quad \text{.....(3.2)}$$

Where *v* (mL) is the volume of effluent accumulated from discharging step, C_i and $C_{e,c}$ (mmol/L) are ion concentration of the influent and accumulated effluent after discharging respectively, and *m* (g) is the total mass of electrodes.

We reported the percentage contribution of ions adsorbed due to electrosorption (electrosorption-IAC) from overall adsorption capacity, using the following calculation:

$$electrosorption\ contribution\ (\%) = \frac{electrosorption\ IAC}{total\ IAC} \times 100\% \quad \text{.....(3.3)}$$

3.4.2. Physical Characterization of ACC electrode

The ACC structural properties were characterized by nitrogen adsorption carried out in liquid nitrogen at -196^{o}C temperature and the relative pressure of nitrogen which was increased from 10^{-7} to 1 bar in 85 steps (adsorption and desorption) using Quantachrome Autosorb iQ system.

The pore size distributions (PSD) (assuming slit-like pores) were calculated by the density functional theory (DFT) method with a NLDFT equilibrium calculation model provided by ASIQwin software from Quantachrome. Prior to N_2 adsorption, the ACC samples were extracted from the CDI cell, dried overnight at 80^{o}C, and cooled down to room temperature in a desiccator. The ACC samples were then cut into small pieces, weighed at ~0.1 g, and then transferred into the Autosorbed column. The samples were degassed under backflip condition approximately for 5.2 hours with final outgas temperature of 300^{o}C.

3.4.3. Chemical Characterization of ACC Electrode

To determine the chemical properties of the electrodes, we used the Boehm titration. This method is commonly used to quantify the concentration of chemical charge on the electrode [22–24]. In this study, we focused on the acidic functional groups due to their relevance to the carboxylate ions used. However, instead of using the direct titration method, we selected the indirect titration method as previously described [25,26]. When compared to the direct method, the indirect Boehm titration has the advantage of eliminating the need for constant degassing or heating because by using Na_2CO_3 as the titrant, CO_2 has no influence on titration [25]. We focused on two sources of chemical charges: carboxyl groups and total acidic groups. Two different bases at a concentration of 0.01 N were used as reactants: 1) NaOH, which reacts with all surface acidic groups (carboxyl, lactones, and phenols), to determine total functional group concentration and 2) $NaHCO_3$, which primarily deprotonates carboxyl, to determine carboxyl group concentration.

To prepare the electrodes for the Boehm titration, we ground the samples and weighed around 100 mg of ACC each to be transferred into two 100 mL polycarbonate vessels. Then, we poured

50 mL of base (NaOH or $NaHCO_3$) into each vessel to react with the ground ACC. Another 50 mL of each reaction base was also added into 100-mL vessel without ACC and served as reference to determine the equivalent point for the titration. We then sealed the vessels and placed in a mini shaker and let them sit while shaken at 500 rpm for 3 days to give enough time for the bases to react with the functional groups. Afterwards we filtered out the aliquots from the ACCs using 0.45 um syringe filter (VWR, USA) and stored in another sealed container to be used within 1-hour to avoid further contamination.

We carried out the dynamic Boehm titration using Autotitrator T910 (ThermoFisher, USA) with a double-junction pH electrode (Orion 9110DJWP, ThermoFisher) for continuous pH measurement and automatic stirrer probe for constant mixing during titration. For all titrations, we used the same titrant, 0.01 N Na_2CO_3, to make sure constant titer within all series (titer = 1). The following titration setting was used: ΔE = 3 mV per addition, t_{min} = 1 s, t_{max} = 45 s. Into 100 mL plastic beaker, we transferred 10 mL of aliquot sample and mixed with 20 mL of 0.01 N HCl.

The quantification of functional groups was performed using the following equations:

$$n_{carboxyl\ groups}\left[\frac{mmol}{g_{ACC}}\right] = \frac{\left((V_{sample,NaHCO3} - \overline{V}_{referemce,NaHCO3}) \times titer \times c\right)_{titrator\ base}}{weight_{ACC} \times \frac{1}{5}} \quad \text{.....(3.4)}$$

$$n_{total\ acidic\ groups}\left[\frac{mmol}{g_{ACC}}\right] = \frac{\left((V_{sample,NaOH} - \overline{V}_{referemce,NaOH}) \times titer \times c\right)_{titrator\ base}}{weight_{ACC} \times \frac{1}{5}} \quad \text{.....(3.5)}$$

Where c (mol/L) is the concentration of titrant (i.e. 0.01 N Na_2CO_3), $V_{reference,reaction\ base}$ (mL) represents the volume of titrant use to titrate the control (i.e., no ACC) until it reached the equivalence point while $V_{sample,reaction\ base}$ (mL) represents the volume of titrant used to reach the equivalence point of the titration for the base + ACC, $weight_{ACC}$ is the total mass of ACC

reacting with base, and titer = 1. The factor of 1/5 is used here representing the 1/5 of reaction base (only 10 mL of aliquot is used for titration from 50 mL generated).

3.4.3. E_{pzc} characterization of ACC electrode

The potential of zero charge (E_{pzc}) of the electrodes is defined as a transition potential region where the overall charge on the surface is equal to zero, resulting in the least adsorption capacity (Zhang et al., 2019). E_{pzc} was tested through differential capacitance minimum measurements at room temperature in a three-electrode system consisting of ACC for both working (WE) and counter electrodes (CE), and Ag/AgCl electrode as the reference electrode, and 5 mM of each target ion (four carboxylates and NaCl) in 100 mM of Na_2SO_4 as the background electrolyte. As E_{pzc} is an electrode property which also depends on the solution, we conducted each E_{pzc} measurement for electrodes relevant to their feed solutions, e.g., the E_{pzc} of the hexanoate-saturated electrode was determined in a Na_2SO_4+$NaC_6H_{11}O_2$ solution. Given the possibility of physical/chemical adsorption of larger carboxylates if a pristine electrode was soaked in the solution, we avoided using highly concentrated feeding solution as electrolyte for E_{pzc} measurements, and instead used a "neutral" solution as background electrolyte which does not contain any anions of interests (chloride, formate, acetate, butyrate, or hexanoate); Na_2SO_4 was selected due to its common use as supporting electrolyte in electrochemical system [27–30].

ACCs for WE were cut into circular shape with 1" diameter while ACC for CE was cut into a larger size (d = 3") to prevent CE to be a limiting factor. The electrochemical impedance spectra were measured at a frequency of 0.2 Hz with a sinusoidal voltage perturbation of 10 mV and a potential increment of 100 mV.

The value of E_{pzc} was determined from the minimum values of the specific capacitance (C), which was calculated using the following equation [31–35]:

$$C = \left|\frac{1}{\omega Z''}\right| \quad \text{.....(3.6)}$$

Where ω (Hz) is the angular frequency and Z'' (Ohm) is the imaginary impedance spectra.

3.4.4. Analytical Method

Similar to CDI experiments in Chapter 2, in this study, we performed continuous measurement of conductivity and pH using a flow-thru conductivity electrode and pH micro electrode (eDaq, Australia) respectively, while DO was occasionally checked using a DO probe (NEOFOX-KIT, OceanOptics) to ensure DO remained below 2 ppm. We used ion chromatography (ICS-5000+, ThermoFisher) and a sodium ISE probe (Orion, ThermoFisher) to measure anions (all carboxylates and chloride ion) and sodium concentrations, respectively.

3.4.5. Data Visualization and Statistical Methods

All figures generated in this study were created using Origin v2017 (OriginLab Corporation), including any statistical works performed. A p-value less than 0.05 was considered statistically significant. Error bars shown in any graphs represent triplicate experiments (n = 3).

3.5. Results and Discussion

3.5.1. Ion Adsorption Capacity

We first measured the ion adsorption capacity (IAC) of the electrodes as a function of the three different pretreatments. Across all ions tested (carboxylates and Cl^-), the PR-E pretreated electrodes consistently removed the most ions of all the pretreatments (**Figure 3.2**). IAC then decreased for the ST-E and CD-E pretreatments. For example, with hexanoate (**Figure 3.2 (F)**), the IAC decreased from 0.89 ± 0.06 mmol/g-C (PR-E) to 0.21 ± 0.00 mmol/g-C (ST-E; ~76% decrease) and 0.11 ± 0.02 mmol/g-C (CD-E; ~87.2% decrease). For the smallest carboxylate formate (**Figure 3.2(B)**), the drop in adsorption capacity was smaller but still followed a similar trend: IAC decreased from 0.49 ± 0.07 mmol/g-C (PR-E) to 0.26 ± 0.02 mmol/g-C (ST-E; ~46.9% decrease) and 0.19 ± 0.03 mmol/g-C (CD-E; ~59.9% decrease) respectively. As comparison, for CDI treating chloride ions (**Figure 3.2(A)**), the IAC dropped from 0.46 ± 0.02 mmol/g-C for PR-E to 0.27 ± 0.00 mmol/g-C (ST-E, ~41.7% decrease) and 0.18 ± 0.00 mmol/g-C (CD-E, ~60.1% decrease); not a significant difference compared to CDI with formate ($p > 0.05$), which can be attributed to the similarity between the shape/size of chloride and formate ions.

Among different carboxylate ions and different electrode conditions, CDI with PR-E treating hexanoate resulted in the most IAC per molar basis (= 0.89 ± 0.06 mmol/g-C). For CDI using PR-E, total IACs from the largest to smallest were: hexanoate, butyrate (0.64 ± 0.05 mmol/g-C), acetate (0.52 ± 0.00 mmol/g-C), formate (0.49 ± 0.07 mmol/g-C), and chloride (0.46 ± 0.02 mmol/g-C). Total IAC of PR-E for hexanoate was calculated to be ~180% larger than for formate (statistically significant, $p<0.05$), indicating stronger overall interactions between the

hexanoate and ACC surface under voltage application than the smaller carboxylates. There is also a strongly positive linear correlation between carbon number of straight-chain carboxylate with the adsorption capacity of CDI with PR-E ($R^2 = 0.95$, $p < 0.05$) (See Appendix B.1). On the other hand, for CDI using ST-E, total IACs among different anions varied differently than of PR-E. Per molar basis, total IACs for all anions ranged between 0.21 ± 0.00 mmol/g-C (for hexanoate) to 0.26 ± 0.02 mmol/g-C (for formate), revealing the difference across anions to be statistically insignificant ($p>0.05$) though carbon number versus total IAC showed negative, strong correlation ($R^2 = 0.99$). An opposite trend for total IAC was observed for CDI using CD-E, with formate had the largest value of IAC among all carboxylate with 0.17 ± 0.02 mmol/g-C. The trend flipped from PR-E, in which the larger carboxylate had smaller IACs.

From our capacity results, we observed that pristine electrodes (i.e., PR-E) had greater adsorptive ability for all anions than previously saturated electrodes (ST-E), and consequently ST-E > CD-E. This is consistent with previous studies in which ST-E and CD-E contained less adsorption sites on its surface for the ions to attach. Adsorptive sites for saturated electrodes were expected to be reduced after physical/chemical adsorption of charged species occupied the previously free sites [19,20,36]. Meanwhile, for conditioned electrodes, in addition to physical/chemical adsorption, previous study has found that available adsorption sites were further diminished by the collapse of structural integrity of electrodes which resulted in the decrease of pores volume/area [37]. To prove this assumption, we tested our electrodes to measure its pores volume and area; we further explained the findings in Section 3.5.2.

.

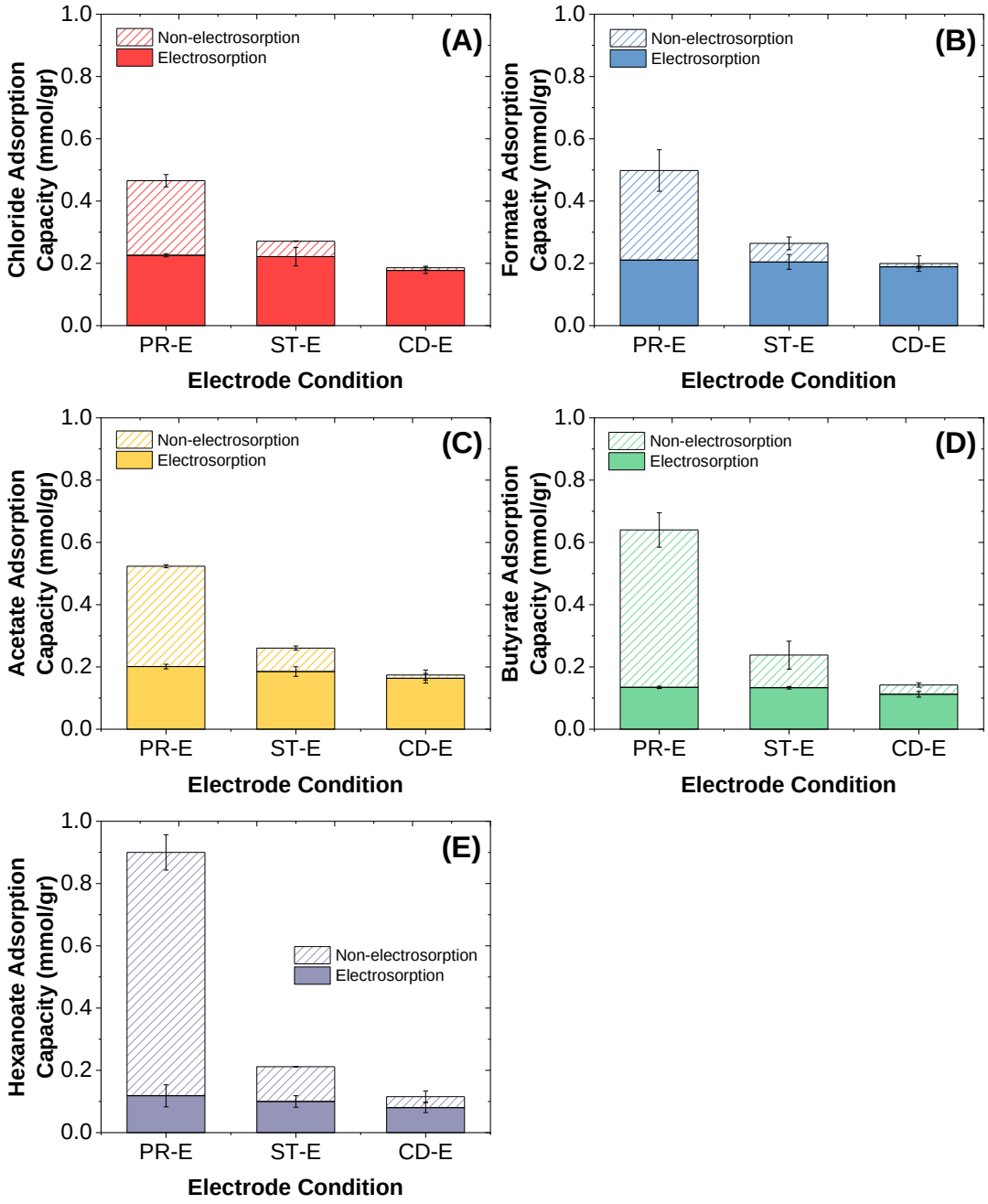

Figure 3.2. Ion Adsorption Capacity (IAC) of Capacitive Deionization (CDI) cell treating (A) chloride, (B) formate, (C) acetate, (D) butyrate, (E) hexanoate-containing solution using Activated Carbon Cloth (ACC) electrodes at three different conditions: pristine electrode (PR-E), previously saturated (ST-E), and previously conditioned (CD-E). The patterned portion of each bar graph represents the IAC due to non-electrosorption interactions and the block portion represents electrosorption capacity. Error bars represent triplicate experiments (n = 3)

We argued that this discrepancy was rooted in the more pronounced negative impact of physical/chemical adsorption form larger carboxylate on the availability of adsorption sites for CDI experiment. Moreover, previous studies for organic ion adsorption found that physical/chemical adsorption would also change the chemical properties of a carbon surface, of which may impact the overall ability of CD-E of hexanoate to adsorb more anions under voltage applications, when compared to CD-E of formate. Performing linear regression on carbon number of carboxylates with IACs of CD-E resulted in strong negative correlation.

Electrosorption versus Physical-Chemical Adsorption

In this study, we looked at the contribution of these adsorption mechanisms when they simultaneously take place under voltage applications and how they behaved differently across different carboxylate (and chloride) ions, as well as different electrode conditions. We calculated the percentage contribution of electrosorption IAC to the total IAC using Eq.3.3 and as shown in **Figure 3.3**.

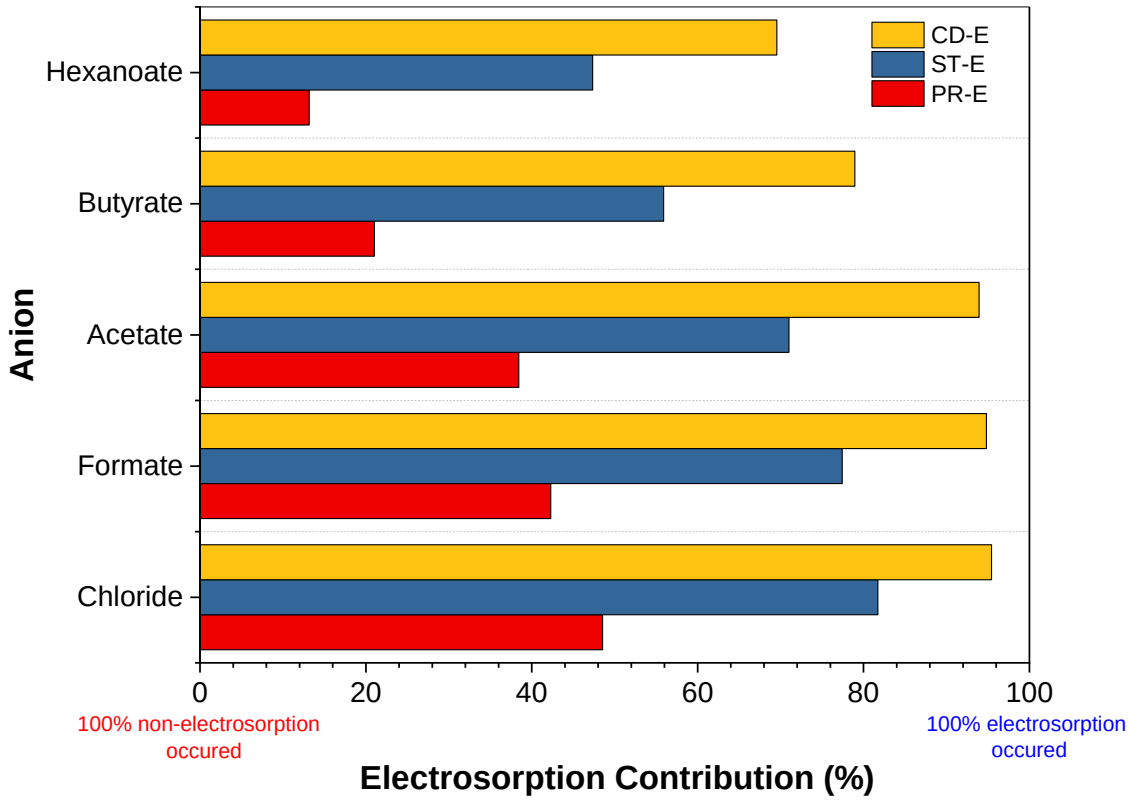

Figure 3.3. Percent contribution of ion adsorption capacity (IAC) due to electrosorption over total IAC for CDI using electrodes at three different conditions treating carboxylate-containing solutions.

Looking at **Figure 3.3**, we observed that for CDI using CD-E, the majority of total IAC came from electrosorptive interactions, particularly for smaller carboxylates such as formate and acetate, with the electrosorption contribution ratio to be >90%. For CDI treating hexanoate, however, 30.45% of total IAC came from the non-electrosorption interactions between ion and ACC electrode, while for butyrate, ~21.04% of total IAC. Conditioning the electrodes was typically performed to equilibrate the electrodes with numerous charging-discharging sequence to make sure that the electrode reached its limit cycle and full electrosorption capacity [38,39]. Given the total of 24 hours exposure of feed solution (12-hr saturation and 12-hr conditioning),

we were expecting that the electrosorption contribution for all anions to be closer to ~100%. However, our results suggested that for larger carboxylate (butyrate and hexanoate), there were still physical/chemical electrosorption occurring for CDI using CD-E. We argued that, in addition to physical/chemical adsorption processes, carboxylate ions could still be retained through complexation or entrapment even after the electrodes have gone through multiple cycles, thus facilitating the ion removal by means of non-electrosorptive forces [40]. The electrode needed to be conditioned for more than 12 cycles would also be a possible explanation. Typically for CDI with NaCl solution, 5 cycles of 30 min charging – 30 min discharging was enough to condition the ACC electrodes [39]. However, given that we were dealing with a more complex ionic species, a prolonged conditioning cycles might have eliminated the non-electrosorption contribution to overall ion removal. Further research to investigate the effectiveness of electrode conditioning would be needed to answer this question.

For CDI using PR-E, the majority of ion adsorbed was attributed to the non-electrosorption, with only 13.16% of hexanoate's total IAC came from electrosorption, the lowest among all carboxylate ions (and chloride). At this stage of electrode condition, most of adsorption sites were still available while the chemical properties of carbon surface were relatively uniform for all CDIs. The difference in IACs comes from the fact that every anion has different affinity towards the ACC surface, which in turn affects surface's adsorptive properties [41]. Polar or hydrophobic groups on ACC functioned as adsorption sites for physical adsorption which, and hydrophobicity of larger carboxylate ions played major role in pushing them towards the ACC more so than inorganic or smaller carboxylate ions. There is also possibility of the impact of pH on the magnitude of physical adsorption, as different protonated forms of organic acid play a dominating role in the physical adsorption process [5]. However, given that all the carboxylate

ions used in this study relatively have the same pKa values for its acid forms (~4 – 5), we assumed its impact to be negligible.

As for CDI with ST-E, the electrosorption contribution ratios for all ions fall between that of CDI with PR-E and CD-E. For saturated conditions, most adsorption sites might have been occupied by physically adsorbed carboxylates, reducing available micropores for EDL formation. Though total IACs of all anions in CDI with ST-E were significantly indifferent, we started to notice there was a shift in overall trend regarding the ratio of electrosorption contribution, in which for CDI treating formate, acetate, and butyrate, electrosorption was more predominant than non-electrosorption (77.42%, 71.02%, 55.90%). By contrast, hexanoate was mostly (52.64%) adsorbed by non-electrosorption interaction.

3.5.2. Electrode Properties Characterizations

3.3.1.1.Surface Chemical Charge Concentration (σ_{chem})

Figure 3.4.(A-E) shows the micropore chemical charge concentration (σ_{chem}) for all electrode pretreatments and ions used in this study. We report σ_{chem} as a total concentration of acidic groups on the electrode surface as well as the fraction of σ_{chem} that is attributed to carboxylic groups. As can be seen from the **Figure 3.4.(A-E)**, the chemical charge concentration for PR-E was 1.7 ± 6.9 μmol/g-ACC for carboxyl and 42.1 ± 17.2 μmol/g-ACC for total acidic groups. The concentration of carboxyl groups on PR-E was almost negligible (~4.02 %). The other acidic functional groups were likely lactones and phenols. For ST-E, we observed that saturation with butyrate and hexanoate increased the chemical charge concentration to 86.2 ± 5.0 μmol/g-ACC for butyrate and 278.4 ± 3.7 μmol/g-ACC for hexanoate. These values were 2-times and 7-

times larger than PR-E, respectively. These results showed that the physically/chemically adsorbed butyrate and hexanoate modified the surface properties of ACC and raised its overall chemical charge concentration by the end of saturation process. Given that carboxylic groups are negatively charged, the saturation would result in the ACC surface to be more negative, thus improving the attractive force for counterions. On the other hand, exposing the ACC to smaller carboxylate such as acetate did not increase σ_{chem} of carboxyl groups significantly (6.9 ± 0.7 μmol/g-ACC) (p-value > 0.05), while the total acidic groups remained relatively unchanged (41.2 ± 3.5 μmol/g-ACC). Furthermore, in the case of formate, we observed a different trend in that total acidic groups decreased sharply by almost ~85% to 6.4 ± 0.7 μmol/g-ACC. As comparison, we also tested the chemical charge concentration on ACC that went through an acid treatment process (HNO_3, 70%). Treating ACC material with concentrated HNO3 was found to be effective to affix negatively charged carboxyl groups onto its surface [39]. We found that the total acidic groups and carboxylic groups of the treated ACC to be 596.2 ± 3.0 μmol/g-ACC and 234.6 ± 3.5 μmol/g-ACC respectively. This finding shows that saturating an ACC with hexanoate-containing solution could achieve the same objective, albeit smaller in magnitude, as acid treatment to introduce more chemical charge concentration to carbon surface. We argued that the ability of butyrate/hexanoate to modify the surface charge concentration of ACC surface is proportional to the length of hydrocarbon portion of carboxylate ions which defined its hydrophobic nature. Unlike larger carboxylates, smaller species such as formate and acetate are not hydrophobic enough to adsorb onto the ACC surface thus increasing the chemical charge concentration. It is well established that the longer the hydrocarbon chain of carboxylate, the more hydrophobic the species is, though previous studies have found that there is a limit to the hydrophobicity of the alkyl chain dissolved in solvent [42]. With regard to the adsorptive ability

of ACC, the increased concentration of acidic groups on ACC surface could be beneficial for the removal of cations from bulk solution due to its increased affinity. In the case of removing anion, however, acidic groups on ACC would reduce the uptake of negatively charged species, ended up resulting in the decrease of anion adsorption capacity [13].

Figure 3.4. also highlights the difference in chemical charge concentrations of conditioned electrodes (CD-E) not only versus PR-E but also ST-E. Conditioning the electrode is different than saturation in which it resulted in the establishment of anode and cathode under voltage application. Based on our results for butyrate-CDI and hexanoate-CDI, for CD-E, two different trends were observed with regard to the chemical charge concentration of CD-E, each for anode and cathode. For CD-anode, σ_{chem} was further increased by conditioning when compared to ST-E, confirming that the physical/adsorption of carboxylate still took place even after electrode was saturated. In contrast, for CD-cathode, the σ_{chem} dropped back to the level of pristine electrode, which can be attributed to the repulsion of co-ion of previously adsorbed carboxylate. The further increase of σ_{chem} on CD-anode for butyrate and hexanoate worked against the anode in its ability to remove more anions. Presence of acidic functional groups shifted the anode potential even less positive and the increase electronegativity on the ACC surface would repel the anion more.

Another key finding from our measurements of ACC chemical charge concentrations is how we ended up with negative values of σ_{chem}. As explained in Section 2, for an indirect BT method, we calculated the σ_{chem} by using reference samples which excluded sources of error such as the titer of the reaction bases and HCl solution [25]. Using Equation 3.4-3.5, positive value from the calculation means that our aliquot samples contained less reaction base due to its reaction with acidic functional groups from ACC, compared to reference sample (reference = only reaction

base, no ACC sample). On the other hand, a negative σ_{chem} value from calculation indicated that our aliquot now contained more basic species than the reference sample. Furthermore, these added base in the aliquot seemed to be present only in ACC samples saturated or conditioned by formate and chloride, but not butyrate and hexanoate. Although, looking at pKa for carboxylic acids, pKa for for formic acid is 3.76, lower than the other three carboxylates (pKa for acetic = 4.72, butyric = 4.82, and hexanoic acid = 4.8).

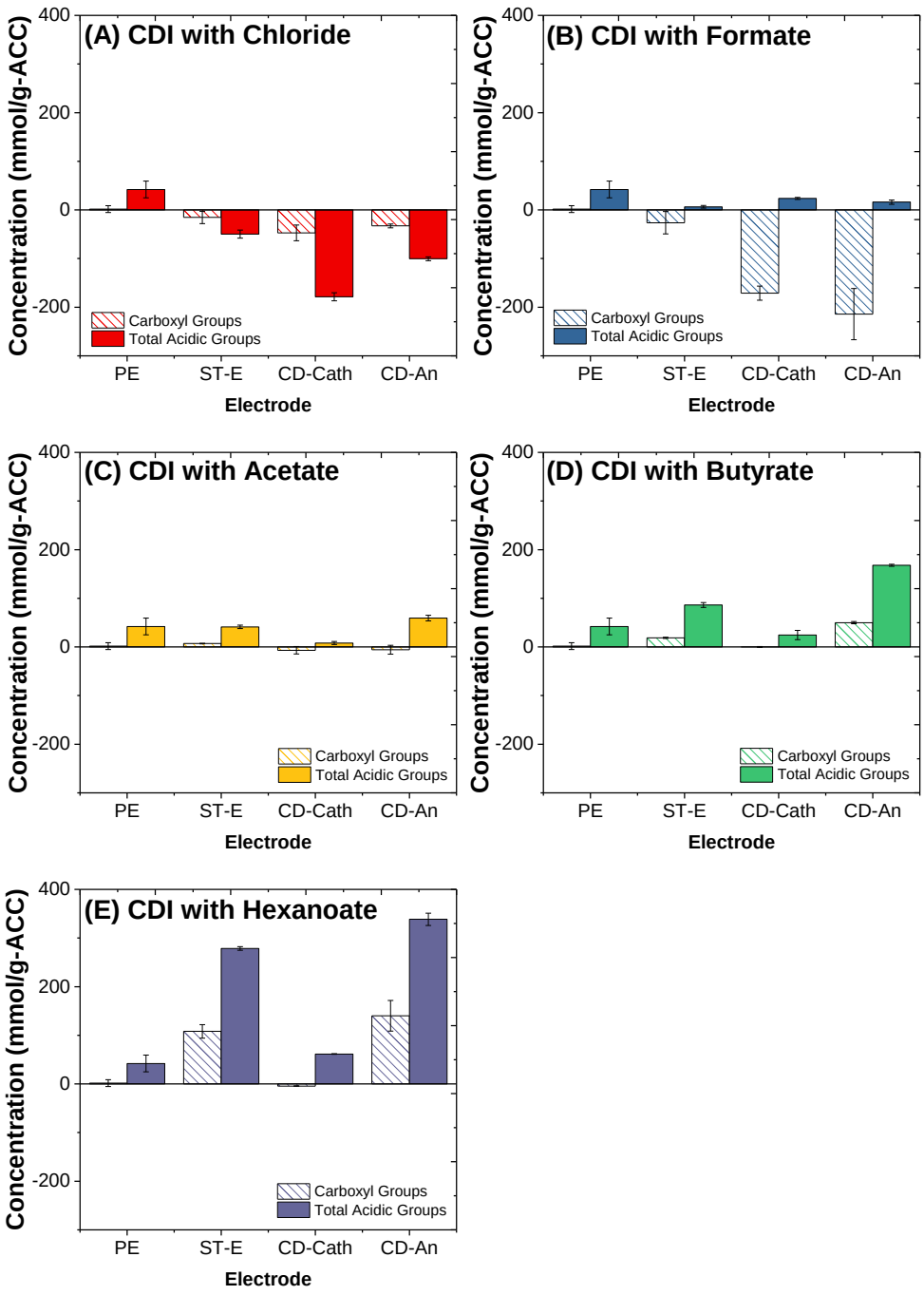

Figure 3.4 Surface chemical charge concentration (σ_{min}) of ACC electrodes used in CDI treating (A) chloride, (B) formate, (C) acetate, (D) butyrate, (E) hexanoate-containing solution. ACC electrodes tested were pristine electrode (PR-E), previously saturated (ST-E), and previously conditioned cathode/anode (CD-Cath, CD-An). The patterned portion of each bar graph represents concentration of carboxyl groups while the color-block portion represents total acidic groups on ACC electrodes. Error bars represent the standard deviation of triplicate experiments (n = 3)

Given that we did not determine the basic functional groups of the ACC, it is rather difficult to accurately determine what happened to the carbon sample which caused it to contain more bases than references. However, previous study by Bernal et al., (2018) showed that activated carbon materials typically have higher total basicity than acidity [43]. When our ACC materials were flushed with DI water, an increase of pH in the effluent was observed. Such increase was attributed to the theory that basal planes of carbon (C_π) behaved as a Lewis base against molecules of H_2O, generated hydroxide ions and $-C_\pi H_3O^+$ surface groups, thus resulting in positively charged sites on electrode surface [44,45]. The reaction is shown below:

$$-C_{\pi(surface)} + 2H_2O \rightarrow C_\pi H_3O^+_{(surface)} + OH^-$$

For carboxylate ions with strong affinity towards the surface of ACC such as hexanoate and butyrate, the positively charged sites from ACC – water interaction were simultaneously encountered by negatively charged groups introduced by the physical / chemisorption of these ions. Given that both chloride and formate do not have similar affinity, the saturation of ACC electrodes with this solution would only increase basicity of the carbon surface, ultimately resulting in the negative value of chemical charge concentration from Boehm titration.

3.3.1.2.E_{pzc} Measurement

Since grafting the carbon surface with carboxylic groups is known to positively shift the E_{pzc} of carbon electrodes [33,46–48], we determined if adsorption of carboxylates onto our electrodes was associated with a shift in E_{pzc}. A positive shift of E_{pzc} would decrease of voltage window in the anode thus resulting in less adsorption of anion [44]. We measured the E_{pzc} for the PR-E, ST-E, and CD-E pretreatments using the differential capacitance approach (see Section 3.4.4) in

electrolytes specific for each ion (e.g., electrode saturated with hexanoate). Our findings are shown in **Figure 3.5**(A-B) below.

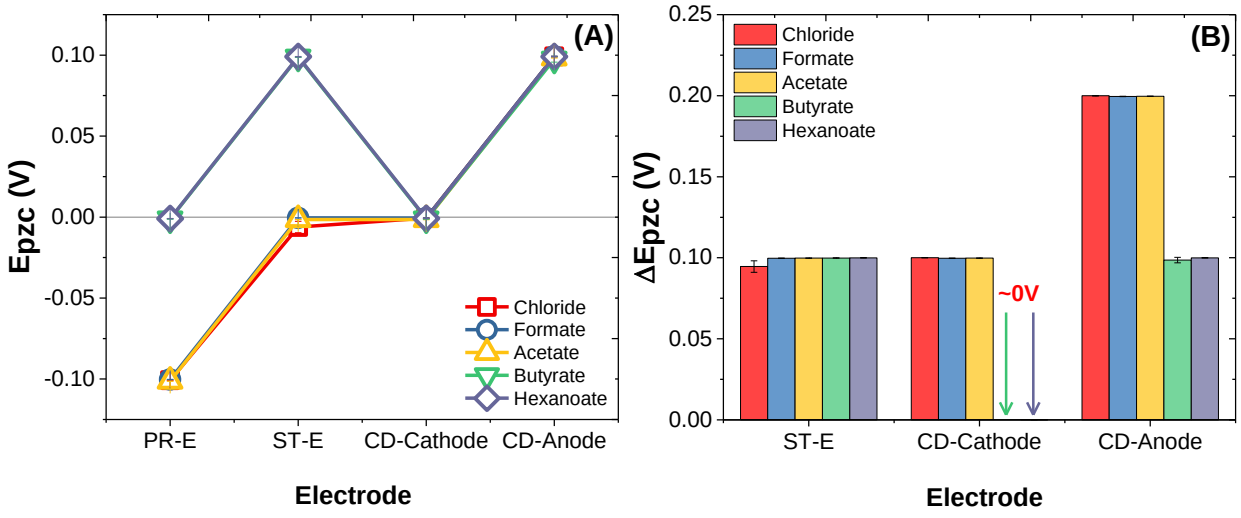

Figure 3.5. (A) Potential of Zero Charge (E_{pzc}) of ACC electrodes at different conditions treating four carboxylate and chloride-containing solutions, and (B) Change in E_{pzc} (ΔE_{pcz}) of saturated and conditioned electrodes from its pristine condition. Error bars represent the standard deviation of triplicate experiments (n = 3)

Figure 3.5(A) showed the E_{pzc} of each electrode used in this study. For PR-E and ST-E, the E_{pzc} can be categorized into two groups: formate and acetate with E_{pzc} = -0.1 V, and butyrate and hexanoate with E_{pzc} = 0 V. However, for CD-E (anode or cathode), all electrodes showed the same E_{pzc} values, which indicates that once the electrodes were conditioned the E_{pzc} was independent to the type of carboxylate ion. The first shift of E_{pzc} occurred after the electrode was saturated with carboxylate (increased by +0.1 V, See **Figure 3.5**(B), however the same trend was observed for all electrodes, indicating that the shift may not be due to the physical/chemical adsorption of carboxylate. The shift for CD-Anode for all electrodes, on the other hand, may indicate the impact of carbon oxidation [46,48] during voltage application. However, the anode potential reading gave indication that the faradaic reaction of carbon oxidation during charging

might be limited since the potential distribution for anode (See **Figure 3.7**) did not result in overpotential that could theoretically promote carbon oxidation (E^o = 0.7 – 0.9 V vs SHE) [49]. pH monitoring (See Appendix B.2) and the fact that the CDI cell was continuously purged with N_2 support the argument that carbon oxidation should be limited.

Previous studies showed that the change in E_{pzc} was typically achieved by significant change in structural and chemical properties of the ACC [31], and we argued that from our results, the E_{pzc} shift due to electrode saturation or oxygen-minimized charging process was not signicant and independent to the types of ions adsorbed on the ACC surface.

3.3.1.3.Pores volume and Pores distribution

Figure 3.6.(A-C) show the pores volume and specific surface area ACC electrodes for CDI. We investigated the change in total volume and area for CDI treating formate versus hexanoate, with chloride as inorganic comparison. We determined that pristine ACC 5092-20 used in this study has large surface areas (DFT-SSA 1658.1 ± 21.7 m2/g) and pore volumes (0.80 ± 0.02 mL/g) with average pore sizes of 0.72; these values are comparable to previous CDI works using the same electrode materials [50]. Across different anions: both formate and chloride did not show any significant changes ($p > 0.05$) in both pores volume and surface area for different electrode conditions (PR-E, ST-E, and CD-E), indicating that these ions did not physically modify the structural integrity of ACC electrodes. This result is consistent with previous study which observed that treatment of activated carbon fibers with acetic acid or 60 min at room temperature did not change its surface area and micropore volumes [51,52]. In CDI studies, pores volume is directly proportional to the adsorption capacity of CDI, and given that electrode's pores for CDI treating formate and chloride did not significantly change throughout different condition, we can

infer that any discrepancy between IAC for fomate and chloride might not be due to structural properties of the ACC.

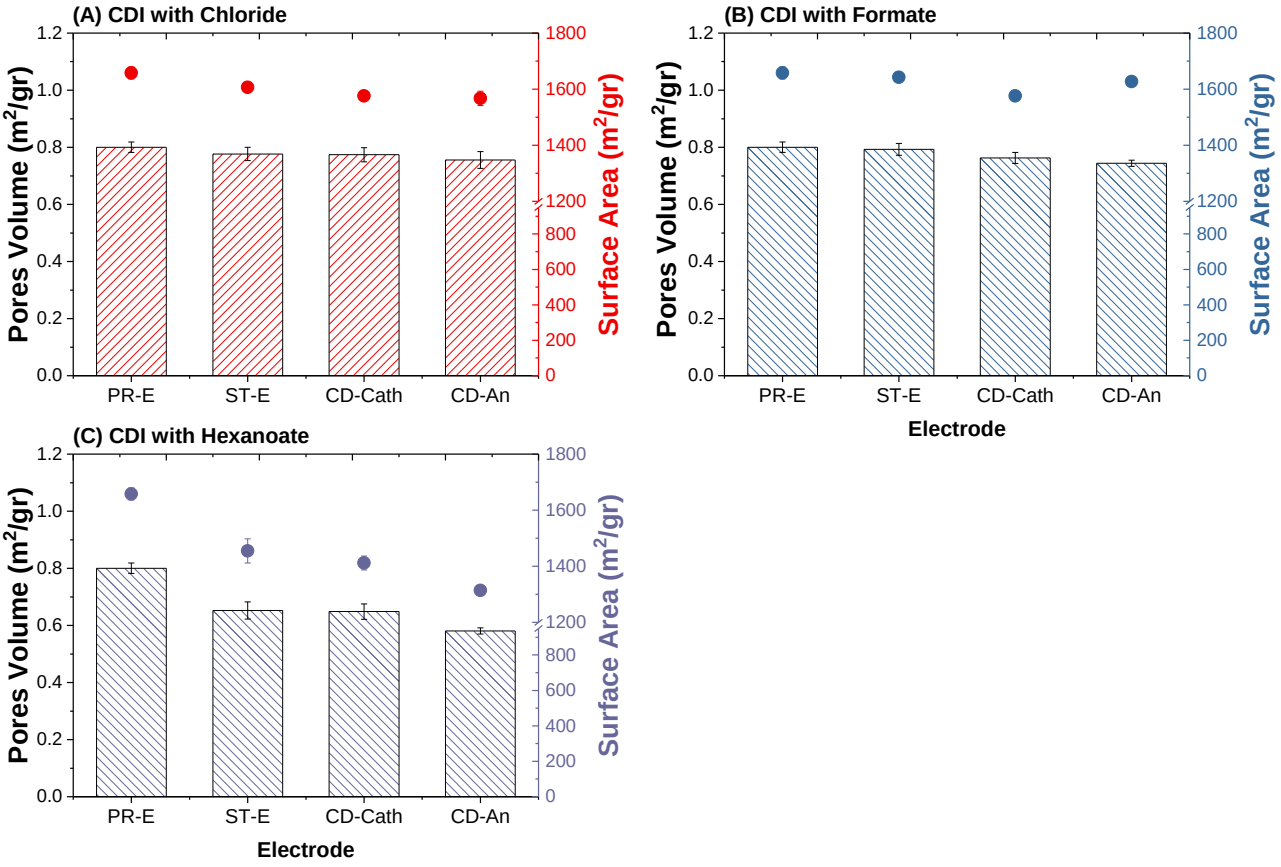

Figure 3.6. Pores volume and Specific Surface Area of ACC electrodes at different conditions used for CDI treating (A) chloride, (B) formate, and (c) hexanoate-containing solution. Bar charts refer to pores volume, while scattered plots refer to surface area. Error bars represent the standard deviation of triplicate experiments (n = 3)

On the other hand, our results showed that saturation of ACC with hexanoate significantly reduced the pores volume as well as surface area, indicated by a 18.5% decrease for pores volume and 12.3% of surface area in ST-E compared to PR-E. The further decrease was observed for CD-Anode, which now has 27.4% less pores volume and 20.7% less surface area

than PR-E. Meanwhile, no significant decrease ($p > 0.05$) in structural property of CD-Cathode from ST-E, meaning the saturation of ACC was minimal on CD-Cathode. We argued that this was a result of co-ion repulsion which blocked the further adsorption of hexanoate onto negatively charged cathode while the voltage is being applied. In contrast, voltage application resulted in a positively charged Anode, further attracting hexanoate ion onto its surface.

Previous studies have well-characterized that a decrease in available pores volume would lead to a lower adsorption capacity [16,33], so we expect CDI treating hexanoate to have a lower electrosorption-IAC compared to smaller carboxylate ions.

Using the information provided by Autosorb instrument, we further explored the structural properties of ACC exposed to hexanoate ions. The current established theory for CDI relied on modified Donnan (mD) potential model to describe the EDL formation on the surface of carbon materials, in which inorganic ions were assumed to be represented by the spherical shape of its hydrated form [22,53,54]. However, little is known about larger, more complex species such as organic ions. In the case of straight-chain aliphatic carboxylate ion like hexanoate in bulk solution, it has two edges with different properties: one is the charged deprotonated end, and the other is alkyl hydrocarbon whose hydrophobicity gets more significant as the chain becomes longer. There is still limited information on the impact of size and shape of the organic ions, particularly regarding their affinity towards the carbon surface and how exactly they are attached to the carbon surface. Looking at the information on pore-size distribution of electrode saturated and conditioned with hexanoate, we observed that the decrease in overall micropores volume were particularly noticeable for pores with half-pore width of 0.51 – 1.1 nm, meaning the hexanoate ions predominantly occupied carbon pores on the “larger” size of micropores., and in turn limiting access for ions to reach the EDL. Given that any pores < 2 nm in width are

considered micropores and important factor to the formation of EDL [55], presence of hexanoate on ACC surface decreased the electrosorption capacity. Further studies are needed to confirm this, but this result could give an educated guess of the size and shape of organic ions like hexanoate in relation to its interaction with electrode surface.

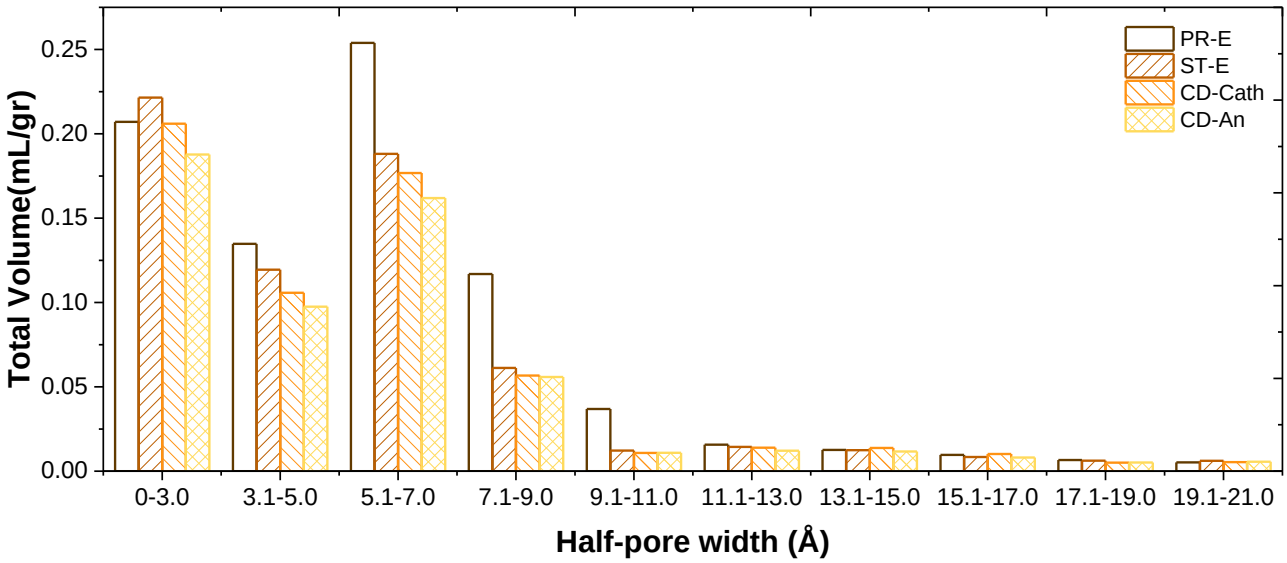

Figure 3.7. Histogram of pore size distribution for ACC electrodes at different conditions treating hexanoate-containing solution.

3.3.2. Applied Voltage Distribution and Electrode Potentials

To further investigate the possible sources of discrepancy in CDI performance treating carboxylate ions, we measured electrode half-cell potentials by putting in-place Ag/AgCl reference electrodes in the reservoirs adjacent to anode and cathode. We recorded electrode potential during the 3-hr charging and 3-hr discharging of CDI experiment for 3 different electrode conditions, PR-E, ST-E, and CD-E, and presented in **Figure 3.8**. From all the curves shown in **Figure 3.8**, we observed relatively symmetric distributions of applied potential for CDI

treating formate and acetate (and chloride), but not for butyrate and hexanoate. For PR-E, anode and cathode potentials were around ~0.06 – 0.12 V prior to CDI experiment for all CDIs. However, after the 3-hr of cell charging at 1.2 V, the anode potentials of CDI treating different anions followed a trend, where formate CDI reached a potential of ~0.41 V while butyrate and hexanoate-CDI hovered around ~0.31 V. Overall, the trend for anode potential is as follows: chloride-CDI > formate-CDI > acetate-CDI > butyrate-CDI > hexanoate-CDI. This trend is consistent with the IAC due to electrosorption (**Figure 3.2**), in which CDI adsorbed formate (0.21 ± 0.00 mmol/g-C) more than hexanoate (0.12 ± 0.04 mmol/g-C). The stark differences were even noticeable for their cathodes, in which the potential for butyrate and hexanoate-CDI dropped to -0.81 V at the end of charging, significantly more negative than CDI with smaller ions). It is known that more negative cathode potential would lead to better removal of cation by the cathode, i.e., higher IAC. However, our results for sodium removal (See Appendix B.3) did not confirm this argument, as we did not see significant difference between sodium adsorption for formate-CDI versus hexanoate-CDI ($p > 0.05$). A possible explanation for this, we argued that instead of sodium ion, the lower cathode potential in hexanoate-CDI preferably adsorbed H^+, and this assumption was supported by the pH reading (See Appendix B.2) which shows that effluent pH increased to the values larger than 7, indicating the proton adsorption and the release of OH- ion. We did not observe this pH increase for formate-CDI during charging which is consistent with previous study [49].

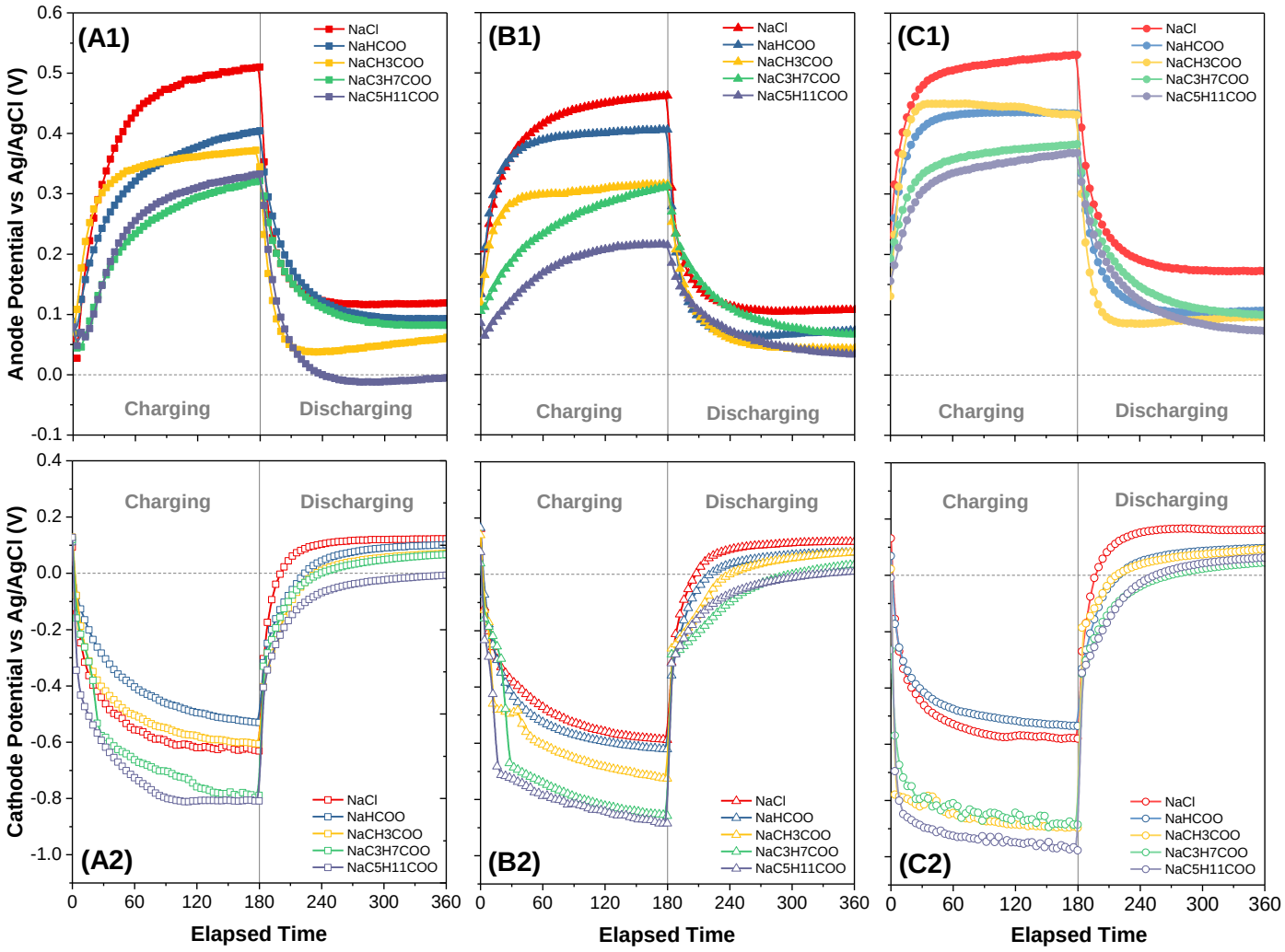

Figure 3.8. Applied Voltage Distribution and Anode-Cathode cell potentials reading during 1.2 V charging and 0 V discharging step in CDI experiment treating four carboxylate and chloride containing solutions using (A.1-2) pristine ACC electrodes (PR-E), (B.1-2) previously saturated ACC electrodes ST-E), and (C.1-2) previously conditioned ACC electrodes. Solid vertical lines separate the charging and discharging step

It is interesting to note such imbalance potential distribution between anode and cathode of hexanoate-CDI could be traced to the exposure of hexanoate onto the surface of ACC by means of physical/chemical interaction. Bouhadana et al., (2011) assumed that the asymmetric distribution of voltage on CDI may indicate possible leakage current due to faradaic side reaction of electrode oxidation which would primarily occur with minimum O_2 level [56]. However, we argued that in the case of CDI treating organic ions such as hexanoate, the imbalance might be the result of the asymmetric conditioning of cathode and anode. Prior to CDI experiment, we started with pristine electrodes for both electrodes where the electrode potential was identical, but once the voltage being applied establishing the opposite charge of anode versus cathode, a negatively charge hexanoate with its affinity towards carbon surface would be physically/chemically adsorbed onto anode but repulsed by the cathode, resulting in hexanoate-exposed anode and hexanoate-free cathode. We argued that the presence of carboxylate ions on anode surface resulted in the applied voltage favoring the cathode because of its less resistance. Previous study showed that the sorption of oxygen-containing groups such as carboxylic acid can lead to the increase in electrical resistivity of activated carbon, which can be attributed to the changes in electron mobility, introduction/removal of electron traps which restricts electron movement across planar surface, or change in activation energy [57,58]. Consequently, unequal surface electric fields or different charge density due to asymmetric configurations would induce the imbalance of potential distribution between the electrodes [31,59]. When the voltage application stopped and the cells were maintained at 0V for discharging step, all electrode potentials returned to their initial potential, except for hexanoate-CDI where potential for both electrodes at the end of discharging were lower than prior the charging step, indicating exposure to hexanoate affected the potential state of the electrode.

In CDI using ST-E and CD-E, the electrode potentials followed similar trend as in CDI with PR-E except for several observations. During charging step, anode potential for formate-CDI (using ST-E and CD-E) reached ~0.40 – 0.43 V while hexanoate-CDI decrease to ~0.21 V for ST-E but reached similar anode potential of 0.36 V for CD-E as PR-E. Anode potential for hexanoate-CDI using ST-E was notably lower by 36% when compared to hexanoate-CDI using PR-E. On the other hand, the cathode potential slightly decreased from -0.81 to -0.88 V. The significant difference between CDI treating larger carboxylates (i.e., butyrate and hexanoate) versus formate and acetate was observed from its asymmetric potential distribution which seemed to be consistent throughout the experiment. One observation regarding the distribution of applied voltage is how for several CDI system, the summation of measured anode and cathode potential did not result in 1.2 V. We argued that this voltage drop is typical in CDI setup as previously observed in several studies. The voltage drop could be associated with the overall cell resistance which resulted in voltage dissipation [31].

3.6. Conclusion

In this study, we investigated the contribution of electrosorption and non-electrosorption process of organic species represented by four carboxylate ions**,** formate ($HCOO^-$), acetate (CH_3COO^-), butyrate ($C_3H_7COO^-$), and hexanoate ($C_5H_{11}COO^-$), onto an activated carbon cloth (ACC) electrodes using electrodes at three different conditions based on their pretreatment process (pristine electrode (PR-E), saturated electrode (ST-E), and conditioned electrode (CD-E)). We quantify the ion adsorption capacity (IAC) due to electrosorption and non-electrosorption and how each component contributed overall. The following points summarize our major findings:

- We found that when PR-E used in CDI experiment, physical/chemical adsorption was the dominant adsorption mechanism. Ions with high affinity towards carbon surface from physical/chemical attraction standpoint such butyrate and hexanoate relied heavily on non-electrosorptive force when the adsorption sites were abundant. In contrast, the percent contribution of electrosorption on total adsorption ion followed the opposite trend where formate-CDI had the highest ratio (42.3%) among carboxylates and hexanoate was the lowest (13.16%).
- Total-IAC dropped from PR-E to ST-E, and now the difference across different ions were not significantly different, with values ranging between 0.21 – 0.27 mmol/g-C. However, there was a dynamic shift in the percent contribution of electrosorption on total-IAC with CDI using ST-E. ST-E for each ion now had different chemical/physical properties, since for hexanoate, most adsorption sites were now occupied resulting in the decrease of free micropores thus limiting the EDL formation. With ST-E, contribution of electrosorption became more predominant (>50%) for smaller ions since very limited physical/chemical adsorption occurred (ratio for electrosorption/total IAC = 69.5%).
- For CDI with CD-E, the majority of ion removal further shifted towards electrosorption, with electrosorption capacity contributes more than 90% of total IAC in CDI treating formate, acetate, and chloride. Physical/chemical adsorption were mostly non-existent for all ions. Electrosorption capacity is independent to chemical charge concentration, free micropores, and electrode potential distribution.
- Saturating ACC with butyrate and hexanoate ions increased the surface charge concentration of the ACC electrode in the form of acidic groups by 2-times and 7-times larger, confirming our assumptions that physical/chemisorption of organic ions may alter

ACC's surface chemical properties. The change in charge concentration did not improve the removal of anion due to co-ion repulsion. .

- E_{pzc} measurement for showed that in our CDI types of ions did not significantly impact the E_{pzc} shift. Saturating and conditioning the electrodes for all ions resulted in minimum change in E_{pzc}, indicating more impactful treatment such as surface oxidation or acid treatment is needed to significantly affect E_{pzc}.
- Electrode saturation with hexanoate solution affected the structural properties of ACC, decreasing the availability of micropores volumes as well as specific surface are by 18.5% and 12.3% respectively. Further decrease was observed for conditioned anode in which the electrode had 27.4% and 20.7% less pores volume and surface area. Investigating the change in pore size distribution revealed that physically/chemically adsorbed hexanoate predominantly filled up the micropores with 0.7 – 1.1 nm half-width size.

3.7. References

[1] A. Al-Karaghouli, L.L. Kazmerski, Energy consumption and water production cost of conventional and renewable-energy-powered desalination processes, Renew. Sustain. Energy Rev. 24 (2013) 343–356. doi:10.1016/j.rser.2012.12.064.

[2] K. Walha, R. Ben Amar, L. Firdaous, F. Quéméneur, P. Jaouen, Brackish groundwater treatment by nanofiltration, reverse osmosis and electrodialysis in Tunisia: performance and cost comparison, Desalination. 207 (2007) 95–106. doi:10.1016/j.desal.2006.03.583.

[3] H.H. Kyaw, M.T.Z. Myint, S. Al-Harthi, M. Al-Abri, Removal of heavy metal ions by capacitive deionization: Effect of surface modification on ions adsorption, J. Hazard. Mater. 385 (2020). doi:10.1016/j.jhazmat.2019.121565.

[4] N. Kim, J. Jeon, R. Chen, X. Su, Electrochemical separation of organic acids and proteins for food and biomanufacturing, Chem. Eng. Res. Des. 178 (2022) 267–288. doi:10.1016/j.cherd.2021.12.009.

[5] R. Wagner, S. Winger, M. Franzreb, Predicting the potential of capacitive deionization for the separation of pH-dependent organic molecules, Eng. Life Sci. 21 (2021) 589–606. doi:10.1002/elsc.202100037.

[6] R.G. Simon, M. Stöckl, D. Becker, A.D. Steinkamp, C. Abt, C. Jungfer, C. Weidlich, T. Track, K.M. Mangold, Current to Clean Water – Electrochemical Solutions for Groundwater, Water, and Wastewater Treatment, Chemie-Ingenieur-Technik. 90 (2018) 1832–1854. doi:10.1002/cite.201800081.

[7] X. Su, H.J. Kulik, T.F. Jamison, T.A. Hatton, Anion-Selective Redox Electrodes: Electrochemically Mediated Separation with Heterogeneous Organometallic Interfaces,

Adv. Funct. Mater. 26 (2016) 3394–3404. doi:10.1002/adfm.201600079.

[8] S. Porada, G. Feng, M.E. Suss, V. Presser, Capacitive deionization in organic solutions: Case study using propylene carbonate, RSC Adv. 6 (2016) 5865–5870. doi:10.1039/c5ra20786j.

[9] X. Su, H.J. Kulik, T.F. Jamison, T.A. Hatton, Anion-Selective Redox Electrodes : Electrochemically Mediated Separation with Heterogeneous Organometallic Interfaces, (2016) 3394–3404. doi:10.1002/adfm.201600079.

[10] P.A. Fritz, P. Zhang, T. Bruschinski, S. Sahin, L.C.P.M. de Smet, M.B. Chan-Park, R.M. Boom, C.G.P.H. Schroën, Steering protein and salt ad- and desorption by an electrical switch applied to polymer-coated electrodes, Sep. Purif. Technol. 250 (2020) 117195. doi:10.1016/j.seppur.2020.117195.

[11] E. Hack, D. Hümmer, M. Franzreb, Concentration of crotonic acid using capacitive deionization technology, Sep. Purif. Technol. 209 (2019) 658–665. doi:10.1016/j.seppur.2018.08.049.

[12] B. Boulinguiez, P. Le Cloirec, Adsorption on activated carbons of five selected volatile organic compounds present in biogas: Comparison of granular and fiber cloth materials, Energy and Fuels. 24 (2010) 4756–4765. doi:10.1021/ef901346f.

[13] C. López-velandia, J.J. Moreno-barbosa, R. Sierra-ramirez, Adsorption of Volatile Carboxylic Acids on Activated Carbon Synthesized from Watermelon Shells, (2014) 227–242. doi:10.1260/0263-6174.32.2-3.227.

[14] M. Belhachemi, Adsorption of organic compounds on activated carbons, Elsevier Inc., 2021. doi:10.1016/B978-0-12-820042-1.00006-7.

[15] S.M. Korotta-Gamage, A. Sathasivan, A review: Potential and challenges of biologically activated carbon to remove natural organic matter in drinking water purification process, Chemosphere. 167 (2017) 120–138. doi:10.1016/j.chemosphere.2016.09.097.

[16] S. Porada, R. Zhao, A. Van Der Wal, V. Presser, P.M. Biesheuvel, Review on the science and technology of water desalination by capacitive deionization, Prog. Mater. Sci. 58 (2013) 1388–1442. doi:10.1016/j.pmatsci.2013.03.005.

[17] Q. Yao, H.L. Tang, Effect of Desorption Methods on Electrode Regeneration Performance of Capacitive Deionization, 143 (2017) 1–6. doi:10.1061/(ASCE)EE.1943-7870.0001245.

[18] D. Liu, X. Wang, Y.F. Xie, H.L. Tang, Effect of capacitive deionization on disinfection by-product precursors, Sci. Total Environ. 568 (2016) 19–25. doi:10.1016/j.scitotenv.2016.05.219.

[19] M. Ryoo, J. Kim, G. Seo, Role of titania incorporated on activated carbon cloth for capacitive deionization of NaCl solution, 264 (2003) 414–419. doi:10.1016/S0021-9797(03)00375-8.

[20] M.W. Ryoo, G. Seo, Improvement in capacitive deionization function of activated carbon cloth by titania modification, Water Res. 37 (2003) 1527–1534. doi:10.1016/S0043-1354(02)00531-6.

[21] Z. Ge, X. Chen, X. Huang, Z.J. Ren, Capacitive deionization for nutrient recovery from wastewater with disinfection capability, Environ. Sci. Water Res. Technol. 4 (2018) 33–39. doi:10.1039/c7ew00350a.

[22] E.N. Guyes, T. Malka, M.E. Suss, Enhancing the ion-size-based selectivity of capacitive deionization electrodes, Environ. Sci. Technol. 53 (2019) 8447–8454.

doi:10.1021/acs.est.8b06954.

[23] S. Rezma, I. Ben Assaker, Y. litaiem, R. Chtourou, A. Hafiane, H. Deleuze, Microporous activated carbon electrode derived from date stone without use of binder for capacitive deionization application, Mater. Res. Bull. 111 (2019) 222–229. doi:10.1016/j.materresbull.2018.11.030.

[24] H. Liu, H. Li, K. Yang, Response surface methodology and performance analyses of the activated carbon electrode for electrosorptive deionization, Int. J. Electrochem. Sci. 15 (2020) 6122–6134. doi:10.20964/2020.07.14.

[25] J. Schönherr, J. Buchheim, P. Scholz, P. Adelhelm, Boehm Titration Revisited (Part I): Practical Aspects for Achieving a High Precision in Quantifying Oxygen-Containing Surface Groups on Carbon Materials, C. 4 (2018) 21. doi:10.3390/c4020021.

[26] J. Schönherr, J.R. Buchheim, P. Scholz, P. Adelhelm, Boehm Titration Revisited (Part II): A Comparison of Boehm Titration with Other Analytical Techniques on the Quantification of Oxygen-Containing Surface Groups for a Variety of Carbon Materials, C. 4 (2018) 22. doi:10.3390/c4020022.

[27] J. Adorna, M. Borines, V.D. Dang, R.A. Doong, Coconut shell derived activated biochar–manganese dioxide nanocomposites for high performance capacitive deionization, Desalination. 492 (2020) 114602. doi:10.1016/j.desal.2020.114602.

[28] A. Thamilselvan, K. Govindan, A.S. Nesaraj, S.U. Maheswari, Y. Oren, M. Noel, E.J. James, Investigation on the effect of organic dye molecules on capacitive deionization of sodium sulfate salt solution using activated carbon cloth electrodes, Electrochim. Acta. 279 (2018) 24–33. doi:10.1016/j.electacta.2018.05.053.

[29] A. Thamilselvan, K. Govindan, A.S. Nesaraj, S.U. Maheshwari, M. Noel, Investigation of carbonaceous materials electrosorption attributes and its performance for capacitive deionization process within the presence of humic acid, Environ. Sci. Pollut. Res. (2021). doi:10.1007/s11356-021-15542-6.

[30] J. Chang, F. Duan, C. Su, Y. Li, H. Cao, Removal of chloride ions using a bismuth electrode in capacitive deionization (CDI), Environ. Sci. Water Res. Technol. 6 (2020) 373–382. doi:10.1039/c9ew00985j.

[31] Y. Algurainy, D.F. Call, Improving Long-Term Anode Stability in Capacitive Deionization Using Asymmetric Electrode Mass Ratios, ACS ES&T Eng. 2 (2022) 129–139. doi:10.1021/acsestengg.1c00348.

[32] A. Omosebi, X. Gao, J. Rentschler, J. Landon, K. Liu, Continuous operation of membrane capacitive deionization cells assembled with dissimilar potential of zero charge electrode pairs, J. Colloid Interface Sci. 446 (2015) 344–350. doi:10.1016/j.jcis.2014.11.013.

[33] X. Gao, S. Porada, A. Omosebi, K.L. Liu, P.M. Biesheuvel, J. Landon, Complementary surface charge for enhanced capacitive deionization, Water Res. 92 (2016) 275–282. doi:10.1016/j.watres.2016.01.048.

[34] X. Che, S. Wang, C. Li, G. Wang, C. Li, S. Wang, D. Li, J. Qiu, Inverted Capacitive Deionization with Highly Enhanced Stability Performance Utilizing Ionic Liquid-Functionalized Carbon Electrodes, ACS Sustain. Chem. Eng. 7 (2019) 15715–15722. doi:10.1021/acssuschemeng.9b03888.

[35] T. Wu, G. Wang, F. Zhan, Q. Dong, Q. Ren, J. Wang, J. Qiu, Surface-treated carbon electrodes with modified potential of zero charge for capacitive deionization, Water Res.

93 (2016) 30–37. doi:10.1016/j.watres.2016.02.004.

[36] D. Liu, X. Wang, Y.F. Xie, H.L. Tang, Effect of capacitive deionization on disinfection by-product precursors, Sci. Total Environ. 568 (2016) 19–25. doi:10.1016/j.scitotenv.2016.05.219.

[37] J. Ma, L. Wang, F. Yu, Water-enhanced performance in capacitive deionization for desalination based on graphene gel as electrode material, Electrochim. Acta. 263 (2018) 40–46. doi:10.1016/j.electacta.2018.01.041.

[38] J.J. Lado, R.E. Pérez-Roa, J.J. Wouters, M. Isabel Tejedor-Tejedor, M.A. Anderson, Evaluation of operational parameters for a capacitive deionization reactor employing asymmetric electrodes, Sep. Purif. Technol. 133 (2014) 236–245. doi:10.1016/j.seppur.2014.07.004.

[39] E.N. Guyes, T. Malka, M.E. Suss, Enhancing the ion-size-based selectivity of capacitive deionization electrodes, Environ. Sci. Technol. 53 (2019) 8447–8454. doi:10.1021/acs.est.8b06954.

[40] L. Chang, Y.H. Hu, Surface-microporous graphene for high-performance capacitive deionization under ultralow saline concentration, J. Phys. Chem. Solids. 125 (2019) 135–140. doi:10.1016/j.jpcs.2018.10.018.

[41] L. Wang, I. Siretanu, M.H.G. Duits, M.A.C. Stuart, F. Mugele, Ion effects in the adsorption of carboxylate on oxide surfaces, studied with quartz crystal microbalance, Colloids Surfaces A Physicochem. Eng. Asp. 494 (2016) 30–38. doi:10.1016/j.colsurfa.2016.01.019.

[42] R. Smith, C. Tanford, Hydrophobicity of Long Chain n -Alkyl Carboxylic Acids, as

Measured by Their Distribution Between Heptane and Aqueous Solutions , Proc. Natl. Acad. Sci. 70 (1973) 289–293. doi:10.1073/pnas.70.2.289.

[43] V. Bernal, L. Giraldo, J. Moreno-Piraján, Physicochemical Properties of Activated Carbon: Their Effect on the Adsorption of Pharmaceutical Compounds and Adsorbate–Adsorbent Interactions, C. 4 (2018) 62. doi:10.3390/c4040062.

[44] X. Gao, A. Omosebi, Z. Ma, F. Zhu, J. Landon, M. Ghorbanian, N. Kern, K. Liu, Capacitive deionization using symmetric carbon electrode pairs, Environ. Sci. Water Res. Technol. 5 (2019) 660–671. doi:10.1039/c8ew00957k.

[45] C.T. Hsieh, H. Teng, Influence of oxygen treatment on electric double-layer capacitance of activated carbon fabrics, Carbon N. Y. 40 (2002) 667–674. doi:10.1016/S0008-6223(01)00182-8.

[46] A. Omosebi, X. Gao, J. Landon, K. Liu, Asymmetric electrode configuration for enhanced membrane capacitive deionization, ACS Appl. Mater. Interfaces. 6 (2014) 12640–12649. doi:10.1021/am5026209.

[47] A. Omosebi, X. Gao, J. Landon, K. Liu, Improving Electrosorption Performance in Membrane Assisted Capacitive Deionization Cells Using Asymmetric Electrodes Configuration, ECS Meet. Abstr. MA2015-01 (2015) 1213–1213. doi:10.1149/ma2015-01/16/1213.

[48] Y. Cheng, Z. Hao, C. Hao, Y. Deng, X. Li, K. Li, Y. Zhao, A review of modification of carbon electrode material in capacitive deionization, RSC Adv. 9 (2019) 24401–24419. doi:10.1039/c9ra04426d.

[49] Y. Algurainy, D.F. Call, Asymmetrical removal of sodium and chloride in flow-through

capacitive deionization, Water Res. 183 (2020) 116044. doi:10.1016/j.watres.2020.116044.

[50] C. Kim, P. Srimuk, J. Lee, S. Fleischmann, M. Aslan, V. Presser, Influence of pore structure and cell voltage of activated carbon cloth as a versatile electrode material for capacitive deionization, Carbon N. Y. 122 (2017) 329–335. doi:10.1016/j.carbon.2017.06.077.

[51] C.L. Mangun, K.R. Benak, M.A. Daley, J. Economy, Oxidation of activated carbon fibers: Effect on pore size, surface chemistry, and adsorption properties, Chem. Mater. 11 (1999) 3476–3483. doi:10.1021/cm990123m.

[52] C.L. Mangun, K.R. Benak, J. Economy, K.L. Foster, Surface chemistry, pore sizes and adsorption properties of activated carbon fibers and precursors treated with ammonia, Carbon N. Y. 39 (2001) 1809–1820. doi:10.1016/S0008-6223(00)00319-5.

[53] P.M. Biesheuvel, M. van Soestbergen, Counterion volume effects in mixed electrical double layers, J. Colloid Interface Sci. 316 (2007) 490–499. doi:10.1016/j.jcis.2007.08.006.

[54] S. Porada, M. Bryjak, A. Van Der Wal, P.M. Biesheuvel, Effect of electrode thickness variation on operation of capacitive deionization, Electrochim. Acta. 75 (2012) 148–156. doi:10.1016/j.electacta.2012.04.083.

[55] L. Han, K.G. Karthikeyan, M.A. Anderson, K.B. Gregory, Exploring the impact of pore size distribution on the performance of carbon electrodes for capacitive deionization, J. Colloid Interface Sci. 430 (2014) 93–99. doi:10.1016/j.jcis.2014.05.015.

[56] Y. Bouhadana, E. Avraham, M. Noked, M. Ben-Tzion, A. Soffer, D. Aurbach, Capacitive

deionization of NaCl solutions at non-steady-state conditions: Inversion functionality of the carbon electrodes, J. Phys. Chem. C. 115 (2011) 16567–16573. doi:10.1021/jp2047486.

[57] Z. Hashisho, M.J. Rood, S. Barot, J. Bernhard, Role of functional groups on the microwave attenuation and electric resistivity of activated carbon fiber cloth, Carbon N. Y. 47 (2009) 1814–1823. doi:10.1016/j.carbon.2009.03.006.

[58] M. Polovina, B. Babić, B. Kaluderović, A. Dekanski, Surface characterization of oxidized activated carbon cloth, Carbon N. Y. 35 (1997) 1047–1052. doi:10.1016/S0008-6223(97)00057-2.

[59] K. Laxman, L. Al Gharibi, J. Dutta, Capacitive deionization with asymmetric electrodes: Electrode capacitance vs electrode surface area, Electrochim. Acta. 176 (2015) 420–425. doi:10.1016/j.electacta.2015.07.036.

Chapter 4: Kinetic and thermodynamic modeling of short-chain carboxylate ions removals in flow-through capacitive deionization (CDI)

4.1. Abstract

Capacitive deionization (CDI) is an emerging water treatment technology for brackish water desalination. Applications of CDI have broadened and include contaminant removal and resource recovery. The previous chapters demonstrated that organic ions (i.e., longer chain carboxylates) are removed in CDI through electrosorption and non-electrosorption mechanisms when activated carbon cloth (ACC) electrodes are used. Modeling their removal is challenging because there are two mechanisms involved. Traditional CDI models have focused on inorganic ion removals that exhibit little to no non-electrosorption. Those models may therefore not accurately describe ions removed through non-electrosorptive mechanisms. In this chapter, we looked at two theoretical approaches to develop a model for the organic ions studied in the prior chapters: (1) Dynamic Langmuir (DL) for kinetic modeling, and (2) modified Donnan (mD) with fused hard-sphere equation of state (mD-FHS) for thermodynamic. For DL, we followed an open-source, grey-box model previously developed to fit our basic experimental parameters and find constants that translated into ion adsorption capacity (IAC). For mD-FHS, we modified previous mD mathematical models to incorporate the effect of size and shape from non-spherical charged species like carboxylates. We verified both models with experimental data obtained from previous chapters of this dissertation. Our results show that the DL model can estimate experimental effluent concentration profiles with ~70% fit estimation. Integrating a FHS component into the mD model resulted in accurate prediction of the electrosorption capacity of

formate across different electrode conditions. However, the mD-FHS model overestimated the IAC of hexanoate, the largest of the carboxylates studied. This overestimation was likely due to using an alkane-based, fused-hard sphere assumption, instead of carboxylate ions, which eliminated the impact of carboxyl functional groups into the equation. We argued, however, given the limited information on geometrical shapes of carboxylates as reference, using alkane substitutes to represents carboxylate ions still provide valuable groundwork for the model development of CDI treating organic ions. Both models require further validation with performance data from other studies. The work described here provides a foundation for modeling ions that exhibit both electrosorptive and non-electrosorptive processes in CDI.

4.2. Significance

This chapter provides a foundation for modeling the removal of organic ions that exhibit both electrosorptive and non-electrosorptive behavior in CDI. Virtually all prior modeling efforts in CDI have focused on small, inorganic ions. Many organic ions do not behave the same as inorganic ions during adsorption processes. Using short-chain carboxylates as model ions, we developed models that incorporate their unique shapes, sizes, and non-electrosorptive behaviors.

4.3. Introduction

Theoretical simulation of ion adsorption is a powerful tool to understand the process occurring inside a CDI cell. Previous CDI models have been developed to guide optimal configurations, operating conditions, and electrode design. Almost all models developed to date have focused on the removal of small, inorganic ions. Those models have been used to explore

voltage windows approach, kinetic adsorption isotherms, extended Randal circuits, as well as electrical double layer (EDL) theory for CDI electrode-electrolyte interfaces [1–10].

Charge storage EDL theory with the modified Donnan model based on Donnan

potential theory was found to accurately predict how many ions can be electrosorbed into electrode micropores [11–21]. On a microscopic level, the mD model can incorporate variables that predict electrosorption performance of porous carbon materials (as well as its selectivity) based on ion valence and size. Suss et al. [22] recently improved the predictive capability of the mD model by including ion volume exclusion interactions in the description of micropore which explained the selectivity between counterions as well as co-ion. Guyes et al. (2019) [23] incorporated chemical charge concentration in their mD model which led to an enhanced size-based selectivity.

Kinetic transport models including Langmuir adsorption isotherms and pseudo-first order kinetics have been used to fit experimental data and explain the adsorption / desorption of different ions. The Langmuir isotherm was found to describe the experimental data better than Freundlich isotherm with regards to electrosorption processes [8], even when the model was used to study the selective adsorption of ions with different charges in solution [24]. A disadvantage of the Langmuir isotherm model is that it does not include system properties, such as charge storage, that can affect adsorption sites on an electrode's surface [2]. Nordstrand et al. [3,8] established an extended version of the Langmuir isotherm called the dynamic Langmuir (DL), which introduces electrode charge into the classical Langmuir model. Through validation with previous experimental CDI performance data, the DL was found to accurately predict CDI performance over a range of relevant parameters while taking into account the effects of co-ion repulsion, asymmetric electrodes, and/or voltage dependence [25]. Similar to the mD model

described above, the DL model has focused on small, inorganic ions. It is unclear if removal of ions that exhibit both electrosorptive and non-electrosorptive behavior in CDI can be accurately captured in the DL model.

Our objective was to explore how well existing thermodynamic and kinetic models describe the removal of organic ions that exhibit both electrosorptive and non-electrosorptive behaviors. For thermodynamics, we used the mD model, and for kinetics, we used the DL. For mD, we started with a proven model used in previous studies to understand the electrosorption process of organic ions. We used an open-source, previously developed DL model and verified it with our organic ion removal data. Since the majority of EDL models for CDI were developed for typical small, inorganic ions that have an assumed spherical shape, we updated the mD model to account for the unique physical properties of our model carboxylates by including a shape factor. We tested both models by experimental verification from data obtained in previous chapters and validated them with data from other experiments.

4.4. Theory

4.4.1. Kinetic Modeling: Dynamic Langmuir (DL)

Dynamic Langmuir is the extended version of Langmuir isotherm which was developed by Nordstrand & Dutta [2,3] for CDI removing small inorganic ions. It utilizes the theory that adsorption is dependent on the number of available sites on the electrode surface as well as its tendency to facilitate simultaneous adsorption and desorption process due to electrostatic interaction between charged surface and counterions as well as co-ion repulsions, which in turn determines the equilibrium [2].

Langmuir adsorption kinetics describes the adsorption process for charged species onto the surface of carbon electrodes with the concentration control equation and the boundary conditions of solid-liquid interfaces as follows [3,8,26]:

$$\frac{dq}{dt} = k_{ads}C(q_m - q) - k_{des}q \quad \text{.....(4.1)}$$

Where q (mol) is the amount of ion adsorbed at time t, q_m (mol) is the amount adsorbed at equilibrium, k_{ads} (1/M.s) and k_{des} (1/s) are the adsorption and desorption rate constants respectively, and C (mol/L) is the bulk concentration of the ion in solution.

In a system involving charged species like CDI, q is replaced with the concentration of only the charged species in solution (σ) leading to the following expression for the adsorption/desorption process:

$$\frac{d\sigma_{ads}}{dt} = k_{ads}\sigma(S - \sigma_{ads}) - k_{des}\sigma_{ads} \quad \text{.....(4.2)}$$

σ (mol/L) is defined as the product of ion concentration in the bulk, C (mol/L), times the ion valence (z; e.g., 1 for Cl^-). The number of voltage-induced electrosorptive sites, S (unitless), which represent stored electronic charge, are introduced into the equation and assumed to be proportional to the applied voltage. When a voltage is applied, opposite charges between the electrode surface and counter-ions results in attraction while co-ions are repulsed. The DL model assumes two key mechanisms which lead to co-ion repulsion: 1) presence of co-ions too close to the electrode surface reduces the available sites for counter-ion adsorption, which contributes to the blockage proportional to the initial concentration in bulk (defined as $\beta_1 C_o$, where β_1 is a constant), and 2) the presence of charged functional groups on the electrode surface reduces the charge storage capacity since they will be neutralized by ions in the solutions even without voltage application (defined as β_0, a constant, and equal to the chemical charge concentration of

the electrode surface, i.e., σ_{chem}). Including these repulsion terms into Eq. 4.2 and that $\sigma = C.z$ with z = 1 (i.e., monovalent ions) yields equation 4.3:

$$\frac{dC_{ads}}{dt} = k_{ads}C(S - \beta_0 - \beta_1 C_o - C_{ads}) - k_{des}C_{ads} \quad \text{.....(4.3)}$$

Assuming the variation in concentration inside the cell during CDI operation is negligible (i.e., C = influent concentration = C_o), Eq.4.3 becomes:

$$\frac{dC_{ads}}{dt} = \left(k_{ads}(S - \beta_0)C_o - k_{ads}\beta_1 {C_o}^2\right) - (k_{ads}C_o z + k_{des})C_{ads} = K_a - K_b C_{ads} \quad \text{.....(4.4)}$$

Where K_a (M/s) and -K_b (1/s) are the two fitting parameters for the DL model representing the intercept (c) and slope (m) from $y = mx + c$, where $y = dC_{ads}/dt$ and $x = C_{ads}$. .

Using equation 4.4, we can then determine the effluent concentration of a CDI cell at any given time using the following mass balance equation (Nordstrand et al., 2019):

$$\frac{dC_{eff}}{dt} = -\frac{dC_{ads}}{dt} + \frac{Q}{v_{cell}}(C_0 - C) \quad \text{.....(4.5)}$$

Where Q (mL/min) is the volumetric flow rate and v_{cell} (mL) is the working volume inside the CDI cell. In this study, both K_a and K_b were obtained by fitting experimental data using Eq. 4.4 and Eq. 4.5 together. Fitting was done using the experimentally obtained effluent concentration profiles for each organic ion and was assisted by a publically available program run on MATLAB (the open-source codes are included in the Appendix C.1).

At equilibrium when no more ions are being adsorbed, $dC_{ads}/dt = 0$, we can calculate the concentration of ions adsorbed as $C_{ads} = K_a/K_b$. Using this value, we can calculate ion adsoption capacity (IAC) using the following equation:

$$IAC\ (mmol/g - C) = \frac{\frac{v_{cell}MW}{m_e}K_a}{K_b} \quad \text{.....(4.6)}$$

Where v_{cell} (L) is the working volume of the cell, MW (g/mol) is the molecular weight of the salt, and m_e (g) is the total mass of electrodes used.

4.4.2. Thermodynamic Modeling: modified Donnan (mD)

There are several models in the literature focused on electrosorption in micropores with overlapped EDLs. We selected the modified Donnan (mD) model because it has been shown to accurately predict the electrosorption performance of inorganic ions in CDI. We only focused on formate and hexanoate because we wanted two ions that exhibit dramatic differences in non-electrosorptive behavior. Based on our experimental results in Chapter 3, hexanoate showed greater non-electrosorptive removal than formate. All parameters needed to predict CDI performance using the mD model come from Chapter 3. We assumed the CDI cell and electrode design were identical to our experimental cell in Chapter 3. In all cases, a 1:1 salt solution with counterions of equal but opposite valence [i.e., one cation (Na^+) and one anion (carboxylates)] was used. Monovalent salt solutions were selected so we can focus primarily on the effect of ion size.

According to the mD model, at equilibrium the relationship between ion concentration in the micropores and macropores of the electrodes can be described as [22,23]:

$$ln\frac{c_{\mathrm{mi,i,j}}}{c_{\mathrm{ma,i,j}}} + z_i\Delta\phi_{D,j} + \Delta\mu_{i,j}^{ex} = 0 \quad (4.7)$$

Where $c_{\mathrm{mi,i,j}}$ (mol/L) is the concentration of ion *i* in the micropores of electrode *j*, while $c_{\mathrm{ma,i,j}}$ is the concentration of ion *i* in the macropores of electrode *j* (assumed to be equal to the ion concentration in bulk solution), z_i is the valence of ion *i* ($z_c = -z_a = 1$), $\Delta\phi_{D,j}$ is the nondimensional Donnan drop between micropores and micropores, and $\Delta\mu_{i,j}^{ex}$ (mM) is the

excess chemical potential (i.e., the difference in concentration) of ion *i* between micropores and macropores of electrode *j*. Subscript *i* = cation (c) or anion (a), and subscript *j* = cathode (C) or anode (A).

In this study we will employ a new approach to calculate $\Delta\mu_{i,j}^{ex}$. Previous studies have used the Boublik-Mansoori-Carnahan-Starling-Leland (BMCSL) equation-of-state (EoS) to determine the excess chemical potential based on ion size and volume. Instead of treating the ion as a hard sphere, which is valid for small, inorganic ions like Cl^-, we treated the organic ions as fused-hard spheres (FHS) EoS, which resemble dumbbell-like structures (**Figure 4.1**).

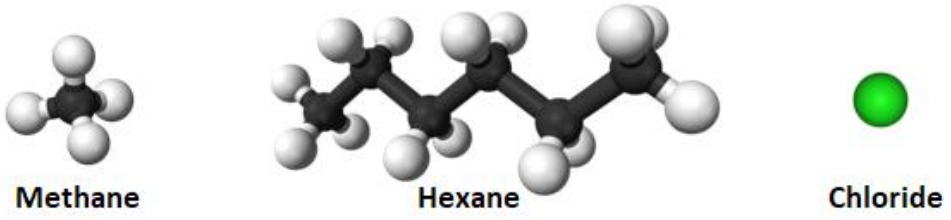

Figure 4.1. 3D structures of methane and hexane represent formate and hexanoate shape and size for mD model in this study. A spherical chloride ion is included and sized accordingly for comparison.

This assumption better represents the actual 3D structure of the carboxylate ions in water. The FHS equation is given by [27]:

$$\frac{\Delta\mu_i^{ex}}{kT} = -\ln(1-y) + \frac{(\rho V_i + rS_i + sR_i)}{(1-y)} + \frac{\left[rsV_i + \left(s^2R_i^2 + 2qsS_2\right)\left(\frac{3}{2}-\frac{y}{3}\right)\right]}{9(1-y)^2} + \frac{qs^2(8-y)V_i}{27(1-y)^3} \quad \text{.....(4.8)}$$

Where $\Delta\mu_i^{ex}$ is the excess chemical potential, k is the Boltzmann constant ($J.K^{-1}$), *T* is the temperature (K), *y* is the packing fraction ($y = \frac{\pi\rho d^3}{6}$, where d is particle diameter), R_i, S_i, V_i are

the geometric functionals (mean radius, surface area, and volume) of ion *i*, ρ is the number density, *r,s,q,v* are functionals of a mixture defined as:

$$r = \rho \sum x_i R_i \quad \text{.....(4.9)}$$

$$q = \rho \sum x_i R_i^2 \quad \text{.....(4.10)}$$

$$s = \rho \sum x_i S_i \quad \text{.....(4.11)}$$

$$v = \rho \sum x_i V_i \quad \text{.....(4.12)}$$

Where x_i is the concentration of ion *i* (mol/L). Regarding the geometric functionals of the carboxylates, an extensive investigation of molecular physics would be necessary and is better suited for a separate study. For our study, we used published information relating to the equation of state of alkanes, which are similar chained hydrocarbon molecules as the carboxylates tested in this study. For simplification, we assumed the geometric functionals of both formate and hexanoate of our carboxylates could be represented by methane and hexane respectively. One limitation of this assumption is that it disregards the presence of the carboxyl group of the ions. The information for the geometric functionals of alkanes were obtain from a study by Jirsak & Boublik (2004) [28].

The final parameter from Eq.4.6. that needs to be defined is $\Delta\phi_{D,j}$. According to Donnan theory, the potential drop between electrode and bulk solution is equal to the sum of the Donnan and Stern potentials of the surface EDL, as given by:

$$\phi_j - \phi_{ma,j} = \Delta\phi_{D,j} + \Delta\phi_{St,j} \quad \text{.....(4.13)}$$

Where ϕ_j is the electrode potential, which is determined by the applied voltage. $\phi_{ma,j}$ is the potential of the macropore and assumed to be zero [22]. $\Delta\phi_{St,j}$ is the potential drop across the Stern layer, and is given by [23]:

$$\Delta\phi_{st,j} = -\frac{F}{V_T C_{St}}(\sigma_{ionic,j} + \sigma_{chem,j}) \quad (4.14)$$

Where C_{St} is the Stern layer capacitance, F is the Faraday constant, and V_T is thermal voltage (i.e., the voltage due to the action of temperature, defined as $V_T = RT/F$, where T is the temperature and R is the ideal gas constant).

We define a balance between different types of charge concentration (mM) in the electrode micropores according to the following equation [22,23]:

$$\sigma_{elec,j} + \sigma_{ionic,j} + \sigma_{chem,j} = 0 \quad (4.15)$$

Where $\sigma_{elec,j}$ is the electric charge concentration at electrode j, which is defined based on the total system charge according to:

$$m_A v_{mi,A} \sigma_{elec,A} + m_C v_{mi,C} \sigma_{elec,C} = 0 \quad (4.16)$$

Where m_A and m_C (g) are the mass of anode and cathode respectively, $v_{mi,A}$ and $v_{mi,C}$ (mL) are the total micropores volume of anode and cathode.

$\sigma_{ionic,j}$ is the ionic charge concentration at electrode j and is given by:

$$\sigma_{ionic,j} = c_{mi,c} - c_{mi,a} \quad (4.17)$$

Where $c_{mi,a}$ and $c_{mi,c}$ are the total ion concentrations inside the micropores of anode and cathode respectively.

Lastly, $\sigma_{chem,j}$ is the chemical charge concentration at electrode *j*, which is defined as the net charge concentration of every charge group (both positive and negative) in the electrode surface. $\sigma_{chem,j}$ depends on the local pH of the electrode surface. It changes dynamically during voltage application. To simplify the model and focus on the size and shape of ions, we assumed that $\sigma_{chem,j}$ is constant over time.

In a two-electrode system, the applied voltage ϕ is distributed between the two electrodes via:

$$\phi - \phi_A + \phi_C = 0 \quad \text{(4.18)}$$

Eqs. 4.6 – 4.17 can be solved simultaneously for the equilibrium ion micropore concentrations of at the anode and cathode at given applied potential (See Appendix C.2 for its MATLAB source code). Ion adsorption capacity (*IAC*) for single-pass charging was calculated from the following equation [23]:

$$IAC = \frac{1}{2} v_{mi} m \left(c^0_{mi,i,C} - c^f_{mi,i,C} + c^0_{mi,i,A} - c^f_{mi,i,A} \right) \quad \text{(4.19)}$$

4.5. Results and Discussions

4.5.1. Dynamic Langmuir (DL) model

4.5.1.1. Model Fitting

We first fitted the DL model with experimental data on NaCl removal in our CDI cell from Chapter 3 (**Figure 4.2**). We did this first because the DL model was originally developed for small, inorganic ions such as Na^+ and Cl^- that exhibit little to no non-electrosorptive behavior. three different conditions: pristine (PR-E), saturated (ST-E), and conditioned (CD-E).

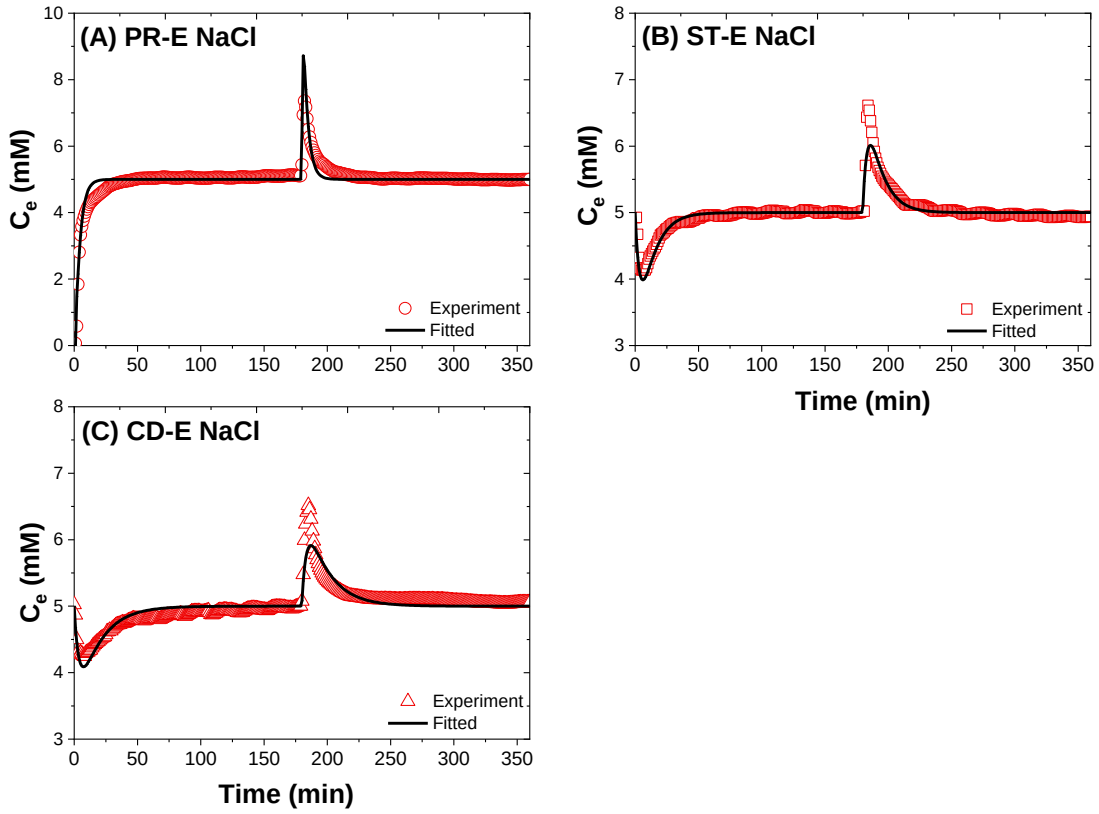

Figure 4.2. Dynamic Langmuir (DL) model fitting to concentration profiles during charging and discharging step of CDI experiment using NaCl at three different conditions: (A) pristine (PR-E), (B) saturated (ST-E), and (C) conditioned (CD-E).

Overall, the DL model agreed well with the NaCl effluent concentration profiles. The fit to estimation values ranged from 53.6 to 70.6% (fit to estimation data represents the measure of how well the response of the model fits the estimation data as calculated from simulation, calculated as percentage = 100*[1-NRMSE], where NRMSE = Normalized Root Mean Squared Error). The lowest effluent concentration reached during the charging step from the fitting agreed well with experimental data. On the other hand, the peak concentrations at the discharging step did not align well, indicating the model slightly overestimated the desorption of NaCl in PR-E while underestimated it in ST-E and CD-E. These disagreements can be traced back to the

development of the DL model. The model follows reversible adsorption-desorption cycles, in which all ions being adsorbed during adsorption will be released during desorption. Based on the DL model fitting, we obtained values for K_a and K_b which represent the fitting parameters and can be later used to calculate equilibrium adsorption capacity (Eq. 4.6). K_a for NaCl was 0.140 mM/s for PR-E, 0.008 mM/s for ST-E, and 0.006 mM/s for CD-E. This decrease was likely due to differences in availability of pores resulting from the pretreatments. PR-E likely had the highest volume of available pores for adsorption during the CDI phase of the tests when compared to ST-E and CD-E since most of its micropores were still unaffected by electrode-electrolyte interaction or voltage application, which were confirmed by results in Chapter 3. On the other hand, Kb for CDI with NaCl is 0.026/s for PR-E, and 0.001/s for both ST-E and CD-E.

Results from the modeling with dynamic Langmuir also showed good agreement with experimental data for CDI treating carboxylate-containing solution. From **Figure 4.3** and **Figure 4.4**, we observed similar effectiveness of the fit to model the effluent concentration of CDI treating NaHCOO and $NaCH_3COO$ solutions compared to CDI with NaCl. The fit to estimation data ranged from 40.1 to 70.9% formate and 37.1 – 73.7% for acetate, with CDI using PR-E as the lowest fit to estimation data for both solutions. We observed this low fitness for PR-E to be consistent across different carboxylate ions (and chloride), hinting the possibility of DL model might not be consistent to represent any breakthrough-type of adsorption experiments. The fitted desorption peak for ST-E and CD-E underestimated the experimental data but overestimated the CDI using PR-E, a similarly observed in CDI with NaCl. Still, there is an overall good agreement visually between the model and experiment. We also obtained the values for K_a for CDI treating NaHCOO: 0.068 mM/s for PR-E, 0.005 mM/s for ST-E, and 0.008 mM/s for CD-E, for for NaCH3COO: 0.054 mM/s PR-E, 0.005 mM/s ST-E, and 0.006 mM/s for CD-E.

Meanwhile, K_b for NaHCOO is 0.011/s for PR-E, and 0.001/s for both ST-E and CD-E, while K_b for NaCH3COO was 0.008/s for PR-E, and 0.001/s for both ST-E and CD-E.

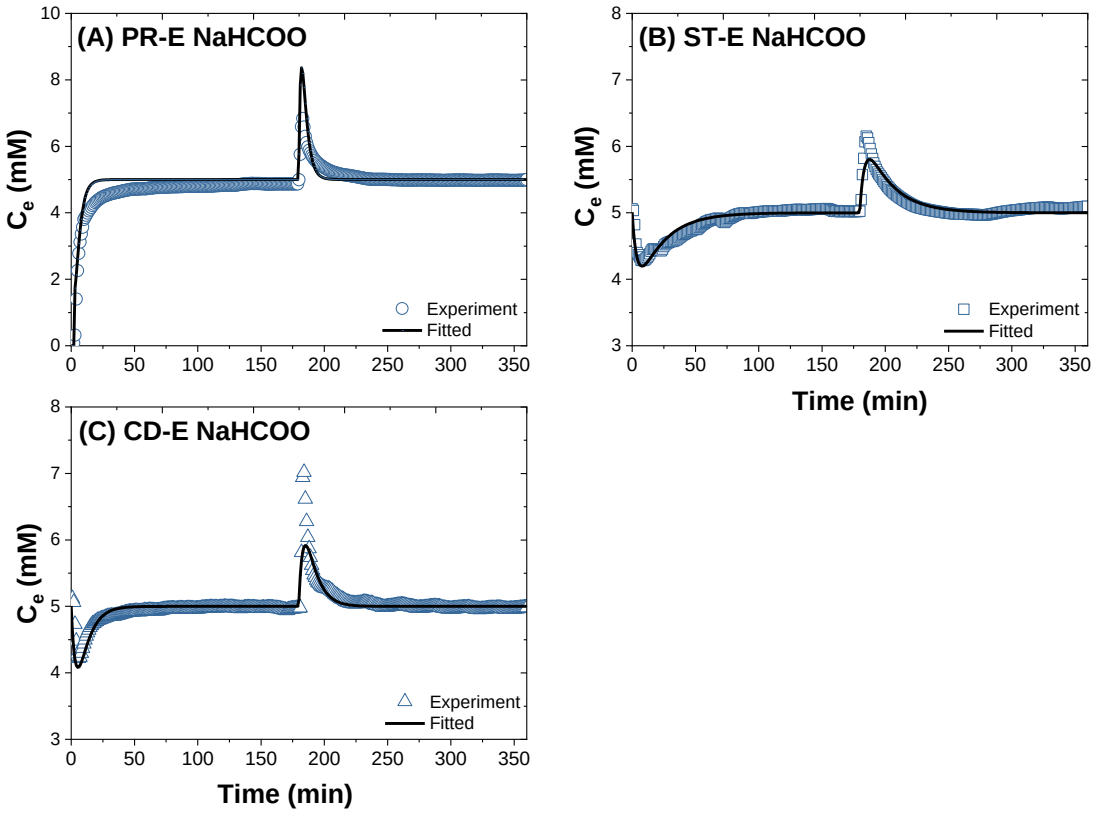

Figure 4.3. Dynamic Langmuir (DL) models were fitted to concentration profile during charging and discharging step of CDI experiment treating NaHCOO using electrodes at three different conditions: (A) pristine (PR-E), (B) saturated (ST-E), and (C) conditioned (CD-E).

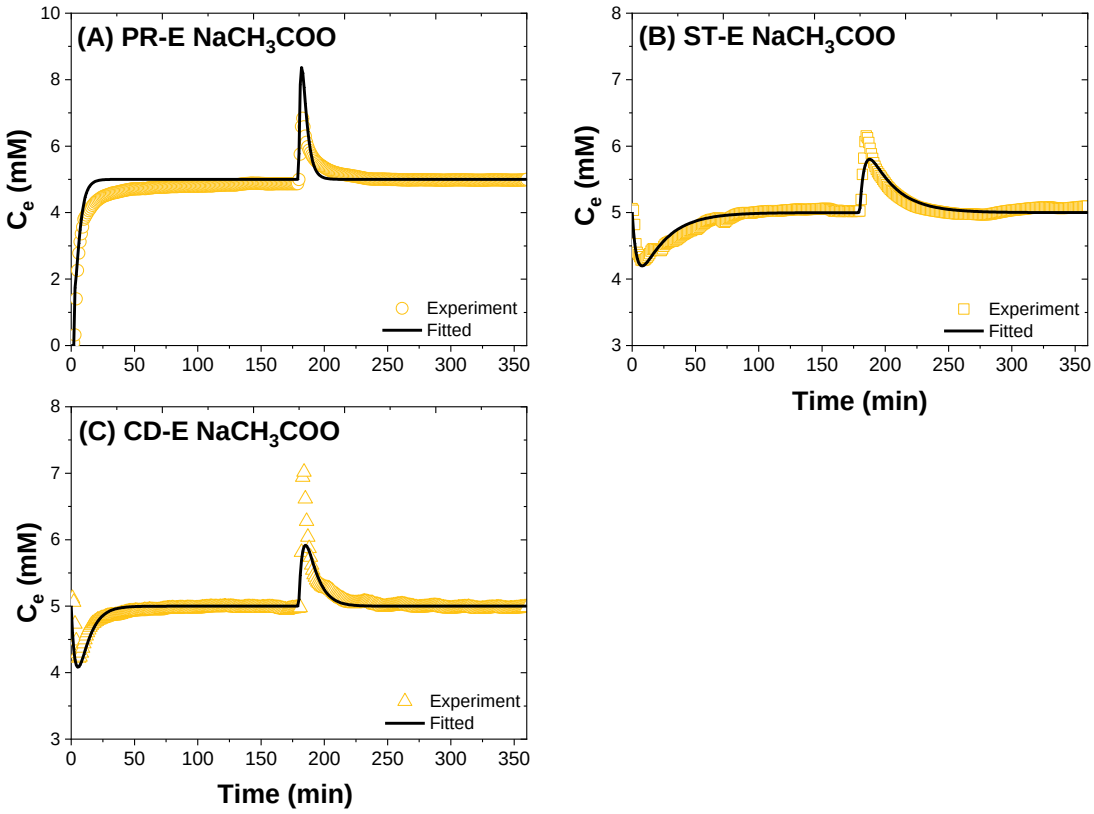

Figure 4.4. Dynamic Langmuir (DL) models were fitted to concentration profile during charging and discharging step of CDI experiment treating $NaCH_3COO$ using electrodes at three different conditions: (A) pristine (PR-E), (B) saturated (ST-E), and (C) conditioned (CD-E).

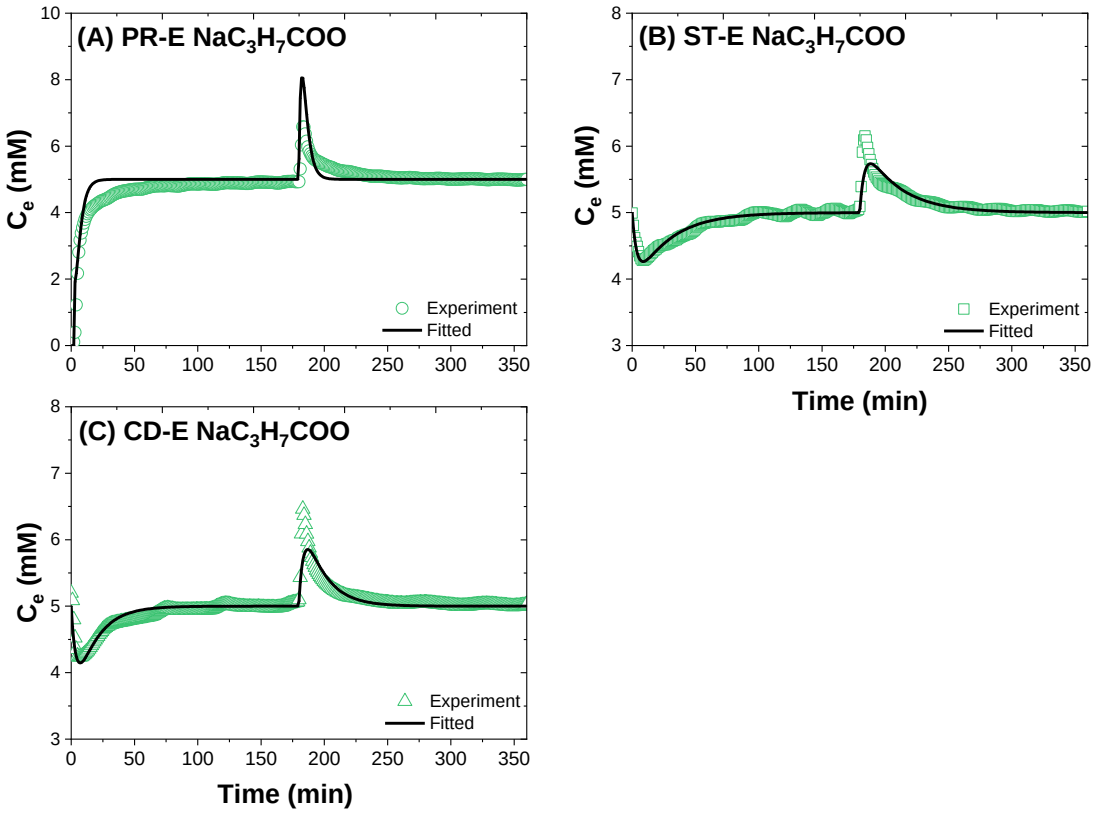

Figure 4.5. Dynamic Langmuir (DL) models were fitted to concentration profile during charging and discharging step of CDI experiment treating NaC_3H_7COO using electrodes at three different conditions: (A) pristine (PR-E), (B) saturated (ST-E), and (C) conditioned (CD-E).

Lastly, **Figure 4.5** and **Figure 4.6** showed the fitting results for CDI treating butyrate- and hexanoate-containing solutions. Once again, DL model closely predicted the effluent concentration profile for the CDI using ST-E and CD-E electrodes for both larger carboxylates. For CDI using PR-E however, the model fit to estimation data is only 32% for $NaC_5H_{11}COO$ and 35% for NaC_3H_7COO. Still, there is an overall relatively good agreement visually between the model and experiment, even for larger carboxylates. We obtained the values for K_a for CDI treating NaC_3H_7COO: 0.088 mM/s for PR-E, 0.007 mM/s for ST-E, and 0.008 mM/s for CD-E; while for $NaC_5H_{11}COO$: 0.047 mM/s for PR-E, 0.005 mM/s for ST-E, 0.003 for CD-E. For

desorption parameters, K_b for CDI treating butyrate ranged from 0.002/s for CD-E to 0.018/s for PR-E; and K_b for CDI with hexanoate solution ranged from 0.001/s for CD-E and ST-E to 0.008/s for PR-E.

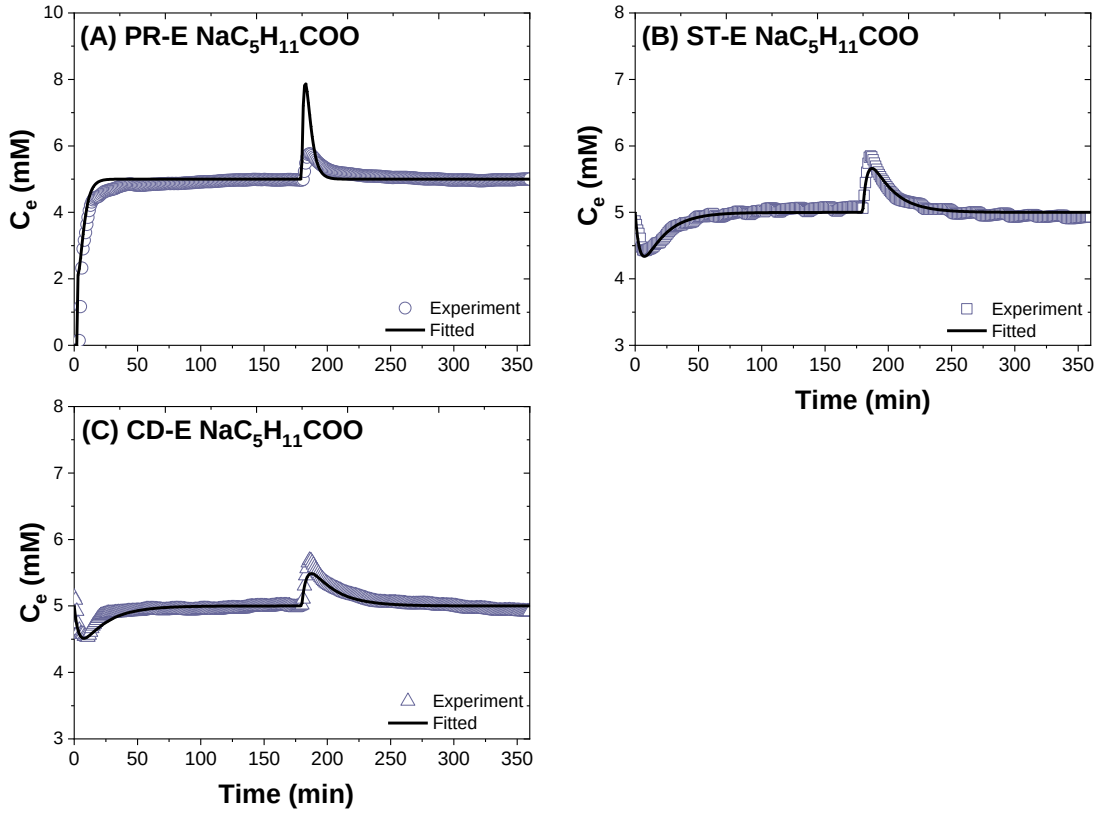

Figure 4.6. Dynamic Langmuir (DL) models were fitted to concentration profile during charging and discharging step of CDI experiment treating $NaC_5H_{11}COO$ using electrodes at three different conditions: (A) pristine (PR-E), (B) saturated (ST-E), and (C) conditioned (CD-E).

4.5.1.2.Ion Adsorption Capacity (IAC)

With the adsorption parameters from fitting the DL model to our experimental data (i.e., K_a and K_b as shown in Table 4.1) we could then calculate equilibrium IACs using Eq. 4.6.

Table 4.1. Fitting parameters of the Dynamic Langmuir model obtained using experimental data from Chapter 3

Treatment	Feed Solution	Ka (mM/s)	Kb (1/s)
Pristine Electrode	NaCl	0.1403	0.0258
	NaHCOO	0.0676	0.0106
	NaCH3COO	0.0538	0.0084
	NaC_3H_7COO	0.0884	0.0185
	$NaC_5H_{11}COO$	0.0472	0.0076
Saturated Electrode	NaCl	0.0080	0.0009
	NaHCOO	0.0053	0.0008
	NaCH3COO	0.0046	0.0006
	NaC_3H_7COO	0.0069	0.0017
	$NaC_5H_{11}COO$	0.0046	0.0009
Conditioned Electrode	NaCl	0.0063	0.0009
	NaHCOO	0.0081	0.0012
	NaCH3COO	0.0060	0.0010
	NaC_3H_7COO	0.0078	0.0016
	$NaC_5H_{11}COO$	0.0032	0.0008

Next, we compared the IAC values calculated from the fitting parameters with the experimental IACs using a parity plot (**Figure 4.7**), first with total-IACs. As previously mentioned in Chapter 3, total-IAC consists of all adsorption mechanisms that removed ions from bulk solutions during CDI charging step. Based on parity plot of modeled IAC with total-IAC (**Figure 4.7A**), modeled IACs underestimated the experimental total IACs, particularly for the PR-E, and to lesser extent, ST-E. For the PR-E pretreatment, the experimental IACs were almost three times larger than the model-fitted IACs, indicating our model failed to accurately estimate the actual CDI performance using pristine electrodes, regardless of the types of ions. This difference was one and a half times for the ST-E pretreatment. Only CD-E showed a 1:1 ratio between experimental IACs and modeled IACs. The coefficients of determination (R^2) from linear regression of the ST-E and CD-E pretreatments were both around 0.99 and significant

(p<0.05), indicating strong linear relationships between experimental total-IAC and the modeled IACs. For PR-E, R2 was 0.02, showing that there was no linear relationship. We can infer from this plot that DL model does not work in predicting the performance of CDI using PR-E in treating carboxylate and chloride ions and will require further modification.

Next, we compared the modeled IACs to the experimental elec-IAC values (**Figure 4.7B**). Elec-IAC is ion adsorption capacity due to electrosorption only. As shown in the parity plot, the points aligned much better with the 1:1 ratio line, indicating that the modeled values agreed well with the experimental values for elec-IAC. The R^2 value for ions across all pretreatments showed a strong and significant correlation (R^2 = 0.967, p<0.05), indicating that the fitted parameters from DL model accurately predicts the actual electrosorbed fraction of ions.

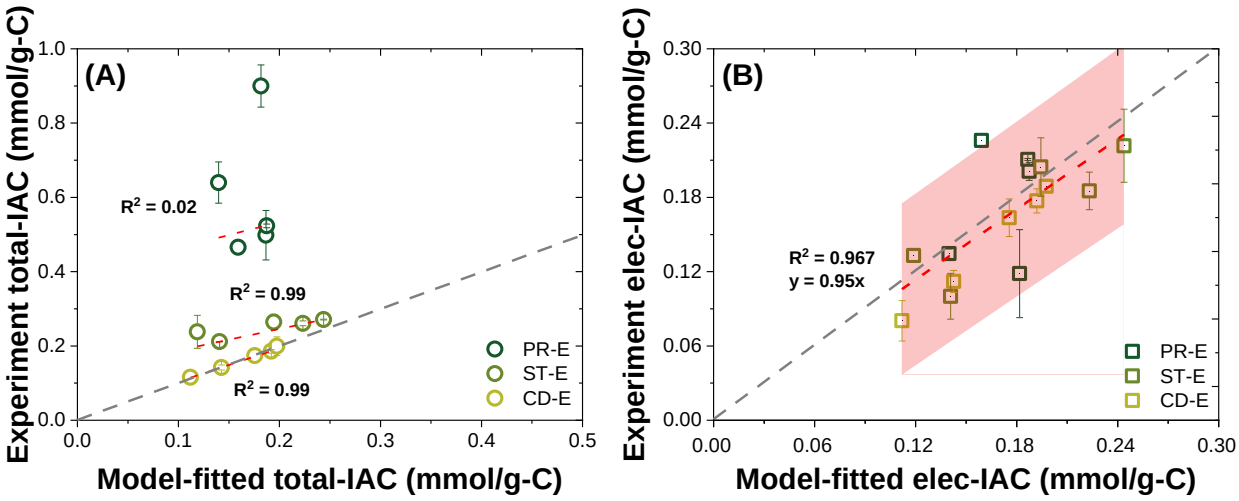

Figure 4.7. Parity plot between modeled and observed ion adsorption capacity (IAC) for all scenarios from experimental data where (A) is for total IAC and (B) for electrosorption IAC. The different shades of green indicate different electrode conditions (PR-E, ST-E, CD-E). The dashed gray line represents a 1:1 relationship while the dashed red line shows the linear regression between the experimental and model data.

Looking at our results comparing calculated IAC from model to total-IAC and elec-IAC, we can infer that the DL model can be used to accurately describe the electrosorbed fraction of ions but not necessarily capture the non-electrosorptive ion removal mechanisms. Although the DL model incorporates charge-induced adsorption and that the fitting is generated from experimental data, we argue that there are underlying assumptions in the model which limited its ability to accurately predict total-IAC.

Particularly for how significant the difference between total-IAC to modeled IAC in the case of CDI with PR-E, we first tried to look more into how we calculate total-IAC. One argument is that total-IAC calculated might also consist of non-sorptive interactions which technically removed ions from its bulk phase but not necessarily by sorption mechanisms; we argued there could be a contribution of pore filling by the ions included in the total-IAC values. To confirm this, we revisited Chapter 3 and calculated how much ions that could be filling the pores of electrode but not necessarily being adsorbed. From Chapter 3 results, we know that the pristine ACC electrode has an average of pores volume of 0.80 ± 0.02 mL/g. Taking chloride ion as an example, we calculated the volume of hydrated chloride using radius of 0.32 nm to be 0.151 nm^3 (or $1.51x10^{-22}$ mL). This means one pristine electrode could be filled by 8.83 mmol of Cl^-/g-electrode mass, further showing that the non-electrosorption result for chloride could be a result of pore-filling and not a sorptive interaction.

Another source of explanation for the discrepancy in modeled-IAC and experimental total-IAC for PR-E may be associated with how the simulation being run with the model. In the current DL model, multi-iterations were done to find the optimum fitting parameters (i.e., K_a and K_b) applicable to all steps, meaning one value of K_a and K_b for both charging and discharging. This assumption would work fine for a system where reversible adsorption-desorption is

observed, such as that of CDI with CDI-E. However, in the case of PR-E, our results showed that ions removed during charging were actually larger in quantities than the ions being released back during the discharging, meaning K_a and K_b values will be compromised to satisfy both steps. A new strategy to find fitting parameters separately for charging and discharging would be an option to develop a more accurate DL model.

In a previous study, Nordtstrand & Dutta [2] has stated that the DL model they have developed is best suited for initial ion concentrations in the middle of the 8.5 – 170 mM range. Outside of that range, impacts such as diffusion limitation for low influent concentration and ion volume exclusion effects in the case of high influent concentrations could cause ion removal to deviate from DL model assumptions. It is possible that the ion concentrations of 5 mM that we used in this study may be out of range to be accurately modeled by the DL model. Tests at higher concentrations and within the range reported are needed to validate this hypothesis. Another possible explanation is DL model does not consider chemical reactions and faradaic effects [3]. Meanwhile from our results, parasitic reactions indeed occurred, as shown by the leakage current during the charging process (See Chapter 3 results). We believe further modification to the model is needed to improve the accuracy of DL in verifying the actual performance of CDI treating organics, where multiple adsorption mechanisms could occur simultaneously.

4.5.1.3.K_a and K_b

As previously defined above, K_a and K_b are the fitting parameters obtained when we fit the experimental data of concentrations profile using two equations: Eq. 4.4 and Eq. 4.5. These two fitting parameters are defined with the following equations:

$$K_a = k_{ads}(S - \beta_0)C_o - k_{ads}\beta_1 {C_o}^2 \quad \text{.....(4.20)}$$

$$K_b = k_{ads} C_o z + k_{des} \quad (4.21)$$

According to Eq.4.4, when the system at equilibrium (meaning no ions being adsorbed and desorbed any further, $dC_{ads}/dt = 0$), we can use the values of K_a and K_b to calculate the concentration of ions adsorbed (C_{ads}) with the equation:

$$C_{ads} = \frac{K_a}{K_b} \quad (4.22)$$

From the above relationship we know that adsorption of ion at equilibrium, C_{ads}, is determined by K_a and K_b values. In this study, we focused on K_a and what parameters could influence its values according to Eq. 4.20:

1. Voltage-induced electrosorptive sites, *S*

Voltage application (*E*) is a critical operational parameter for CDI process since it is the driving force for carbon electrode to form EDL and electrosorb ions. In DL model, how much voltage being applied onto CDI determines the number of voltage-induced sites, *S*, which in turn determines the ion adsorption capacity [3]. This assumption, however, is applicable when charge efficiency is high enough to ensure proportionality relationship between voltage (*E*) and voltage-induced sites (*S*). Looking at the DL model development, if we assumed that $E \sim S$ and $S \sim K_a$, any increase or decrease in *E* would be proportional to K_a. Consequently, assuming K_b is constant, higher K_a would result in higher C_{ads}.

Knowing that K_a depends on the voltage application (*E*), we can develop prediction for CDI performances over varying potentials to provide preliminary guidance of how our CDI treating carboxylate-solution would perform. Here we chose 3 different applied voltages: 0.8, 1.2, and 1.6 V. Using K_a obtained from experiment for $E = 1.2$V, we can calculate K_a for $E = 0.8$ V and 1.6 V using the following equation:

$$K_{a2} = \frac{E_2}{E_1} K_{a1} \quad \text{.....(4.23)}$$

The summary of K_a for each carboxylate ions at different voltage values are presented in the table below:

Table 4.2. K_a values for predicted CDI treating different organic ions at different voltage applications (E)

***E* (V)**	***K*a (mM/s)**			
	NaHCOO	**$NaCH_3COO$**	**NaC_3H_7COO**	**$NaC_5H_{11}COO$**
0.8	0.0054	0.0040	0.0052	0.0021
1.2	0.0081	0.0060	0.0078	0.0032
1.6	0.0108	0.0080	0.0104	0.0043

We can use the above K_a values (together with K_b, assumed to be constant across different voltages) as fitting parameters to simulate the effluent concentration profile and estimate C_{ads} of CDI at different voltage applications. **Figure 4.8(A-D)** showed the variability of the dynamic effluent concentration over time during charging-discharging steps in CDI treating carboxylate-containing solutions at different K_a values as determined by voltage application. The predicted IACs were inserted into respective figures to show the expected performance of CDI over variation in potential.

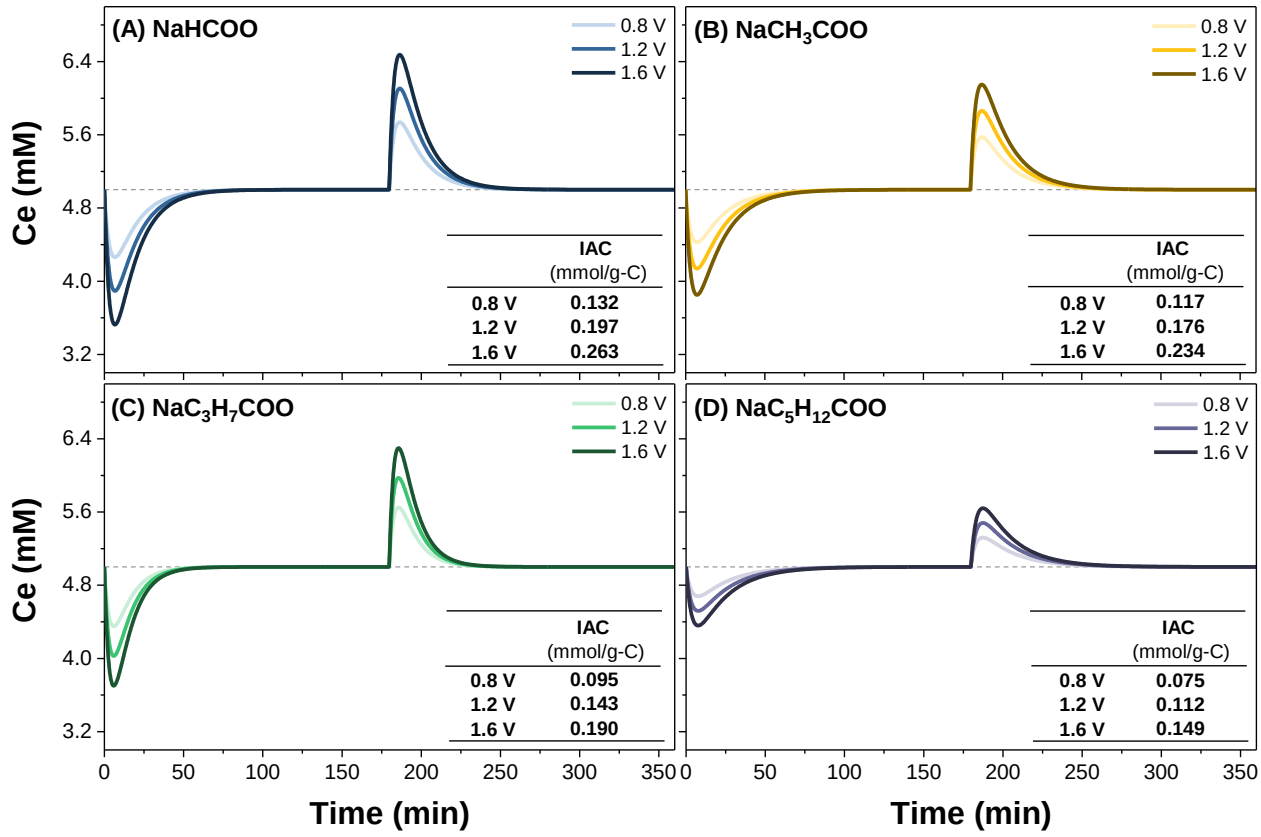

Figure 4.8. Predicted effluent concentration dynamic over time during charging – discharging step of CDI experiment treating: (A) NaHCOO, (B) $NaCH_3COO$, (C) NaC_3H_7COO, (D) $NaC_5H_{11}COO$, using conditioned electrodes (CD-E) at different voltage application. Fitting parameters include K_b obtained from experiment and K_a calculated based on proportionality

2. Blockage sites due to presence of charged functional group, β_0

In CDI, chemical charge concentration, σ_{chem}, on an electrode is directly associated with the charged functional groups in the micropores [23]. Depending on the objective of CDI, presence of charged functional groups on the electrode surface can be a positive or negative contributor to the overall performance of ion adsorption. In the case of anode to remove anions, presence of negatively charged functional groups would result in anion repulsion, eventually decrease adsorption capacity, while positively charged functional groups would enhance the

anion adsorption. For typical AC electrodes, the net micropore chemical charge is assumed to be zero, meaning the charge is balanced between positively and negatively charged functional groups.

In DL model specifically, β_o is associated with the presence of charged functional groups that could be neutralized by the ions from solution when there is no voltage, resulting in "blocked" sites for supposedly electrosorption once the voltage being applied ($\beta_o \sim \sigma_{chem}$). This means the more charged functional groups presence, the less voltage-induced adsorptive sites, *S*, will be available for electrosorption, ultimately decreasing K_a.

Knowing that the Ka is affected by charged functional groups, we can make prediction for CDI performances over varying chemical charge concentrations. Here we chose 3 different chemical charge concentrations of electrode (σ_{chem}): 0, -0.25, and 0.50 mmol to simulate. Negative values for σ_{chem} indicating the predominant presence of negatively charged functional groups (e.g., carboxyls, phenols, etc) which would lead to anion (i.e., carboxylates) repulsion. Now, to calculate the magnitude of impact from negatively charged functional group, we proposed the following approach: assuming that for electrode without surface charge functional group (e.g., typical untreated electrodes), the voltage-induced sorptive sites, *S*, would be 100% available. For electrode with certain chemical charge concentration, we can calculate its impact on *S* by assuming that the mass of surface functional groups would cover some sorptive sites thus reducing the number of *S*:

$$S_{\sigma chem} = S_0 \left(1 - \frac{\sigma_{chem} MW_{COO}}{m_{elec}}\right) \quad (4.24)$$

$$K_{a,\sigma chem} = \frac{S_{\sigma chem}}{S_0} K_{a0} \quad (4.25)$$

Where S_0 is the voltage-induced sorptive sites at 100% (i.e., neutral net surface charge), $S_{\sigma chem}$ is the voltage-induced sorptive sites of electrode with negative net surface charge, MW_{COO} (gr/mol) is the molecular weight of carboxyl functional groups, and m_{elec} (g) is the mass of 1 electrode (here equal to 0.1 g). Summary of K_a for each carboxylate ions at different chemical charge concentration of the electrode are presented below:

Table 4.3. K_a values for predicted CDI treating different organic ions from different chemical charge concentration (σ_{chem}) of the electrode

σ_{chem}	K_a (mM/s)			
(mM)	**NaHCOO**	**$NaCH_3COO$**	**NaC_3H_7COO**	**$NaC_5H_{11}COO$**
0	0.0081	0.0060	0.0078	0.0032
-0.25	0.0072	0.0053	0.0069	0.0028
-0.50	0.0063	0.0047	0.0061	0.0025

We then use the above K_a values as fitting parameter to simulate the effluent concentration profile and estimate C_{ads} of CDI at different σchem of electrode, resulting in **Figures 4.9(A-D)** below.

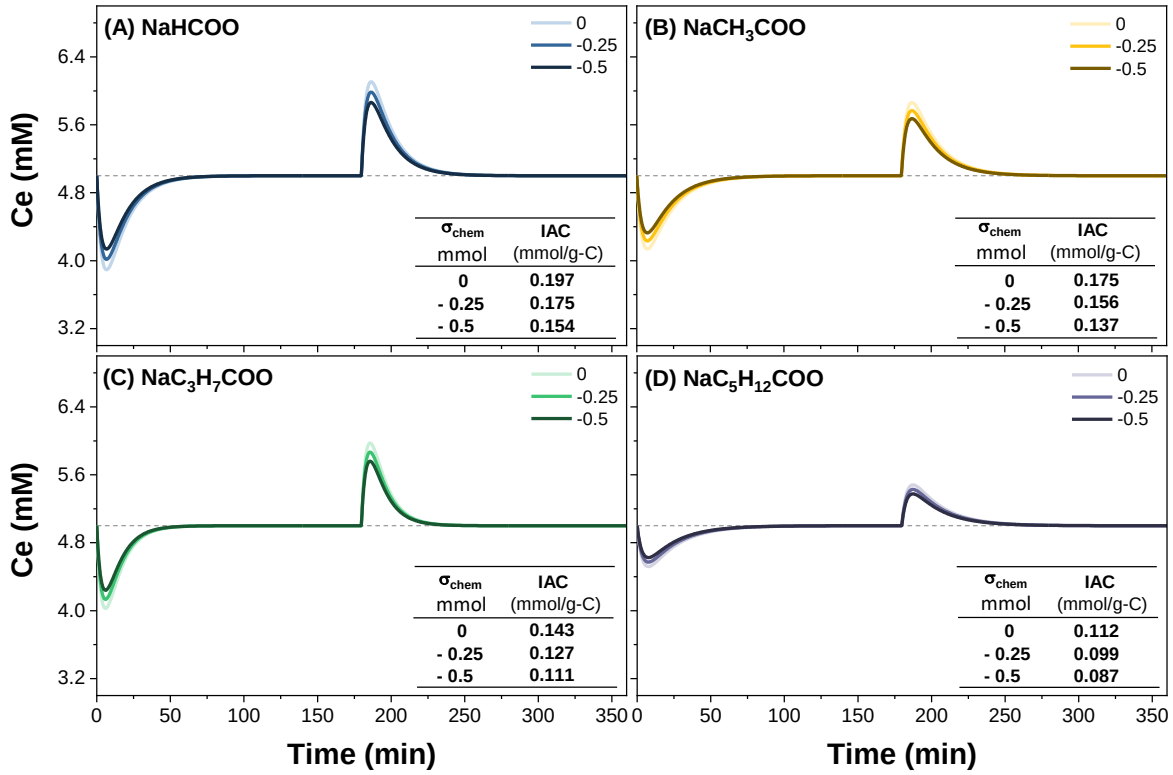

Figure 4.9. Predicted effluent concentration dynamic over time during charging – discharging step of CDI experiment treating: (A) NaHCOO, (B) $NaCH_3COO$, (C) NaC_3H_7COO, (D) $NaC_5H_{11}COO$, using conditioned electrodes (CD-E) at different chemical charge concentration (σ_{chem}) of the electrode. Prediction curves were generated using the K_a and K_b parameters obtained from model fitting of experimental data at 1.2 V.

3. Blockage due to the presence of co-ions, $\beta_1 C_0$

Another mechanism that leads to the decrease of voltage induced adsorptive sites according to DL model is co-ion expulsion by the electrode surface [2,29]. Nordstrand argued that the presence of co-ions close to the electrode wall might work against the objective of CDI in adsorbing targeted counter-ions since the adsorptive sites now being occupied to repel the co-ions, instead of attracting counter-ions into its pore. The presence of co-ions will contribute to the blockage of sites and are proportional to the initial concentration of ions, Co. The more co-

ions presence in the bulk initially, the more blockages are expected to occur, eventually leading to the decrease of voltage induced electrosorptive sites, S. Therefore, in order to maximize the ion adsorption, we would want to choose a lower concentration of ions in the bulk.

However, it is rather difficult to evaluate the performance of overall CDI and make a predictive output just by looking what initial ion concentration would do to Ka. Based on DL model, increase in Co would reduce the Ka by means of increasing co-ion repulsion. However, from operational CDI standpoint, increasing Co solution concentration would also improve the solution conductivity thus minimizing parasitic reactions. We argued there are contradicting impact of Co onto the overall performance of CDI and making performance prediction would need to consider more factors than just proportionality of the fitting parameter Ka. Further study pertaining to this discussion would be needed.

4.5.1.4.Dynamic Langmuir model validation

The next step towards the development of DL model for CDI treating organic ions is the model validation using different sets of experimental data. Unfortunately, reports on CDI system treating carboxylate ions are very limited and irrelevant for the use to validate the DL model. Therefore, in this chapter, we used data from our own previous experiments for CDI treating 3 different carboxylate-solutions: NaHCOO, $NaCH_3COO$, and NaC_3H_7COO. These experiments were conducted using the same setup for our CDI with CD-E in this study with notable differences: 1) each charging and discharging step were done in 30 minutes period instead of 3 hours, 2) C_o for solution was 10 mM instead of 5 mM, and 3) flow rate used was 2 mL/min instead of 3 mL/min. We only input these relevant parameters into our model and did not consider other operational parameters. We fitted the data using the same DL model approach and

generate the concentration profile for each CDI system in **Figure 4.10(A-C)**, highlighting the results from experiment and fitted curve.

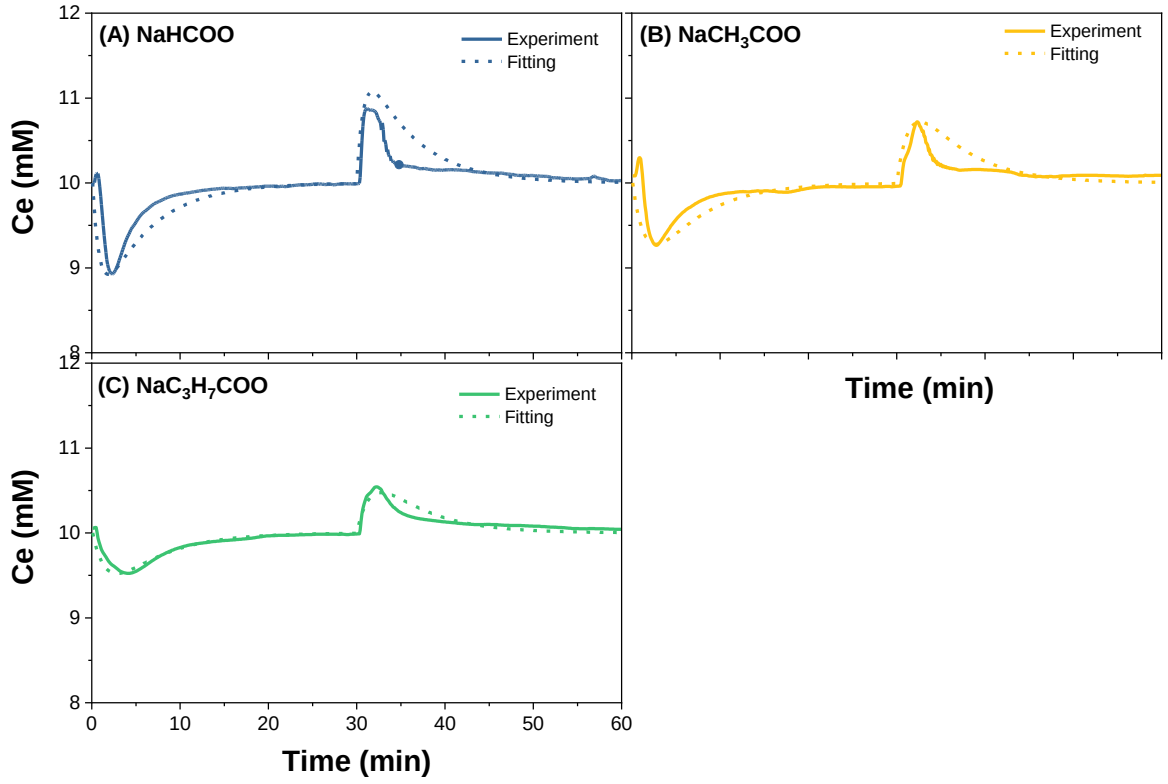

Figure 4.10. DL model validation using dataset from different experiment setup of CDI treating carboxylate ions showed good agreement between the model and actual observation of the effluent concentration profile over charging and discharging steps. Prediction curves were generated using the K_a and K_b parameters obtained from model fitting of experimental data at 1.2 V.

As **Figure 4.10(A-C)** shows, DL model can estimate the performance of another CDI system treating carboxylate ions well with fit to estimation data falls within 65-75% range. These results showed that DL model can accurately model the actual performance of CDI with carboxylate ions, assuming CD-E is used as the electrode condition. Using fitting parameters (K_a and K_b) obtained from the simulation, we can also calculate the expected IAC for the datasets:

43.3 μmol/g-C for formate, 32.2 μmol/g-C for acetate, and 23.1 μmol/g-C for butyrate. The model predicted the IAC to be within ~15% of that actual IAC for all three carboxylates, indicating a good agreement between model and experiment.

4.5.1.5. Proposed modification to Dynamic Langmuir model simulation approach

Using current DL model as developed by Nordstrand & Dutta [2,4-6], we found that though DL model can fit the experimental results of CDI using CD-E well, but it still has limitations when dealing with PR-E and to a lesser extent, ST-E electrode conditions, particularly in estimating the performance of CDI, i.e., the adsorption capacity. We argued that with CDI using PR-E and ST-E, multiple adsorption processes occur simultaneously: reversible electrosorption and irreversible non-electrosorption. Previously non-electrosorbed ions were assumed to remain in the electrode even after the cell was short-circuited, resulting in asymmetrical adsorption-desorption cycle. MATLAB simulation using DL model, on the other hand, was executed to find the K_a and K_b which best fit both adsorption and desorption, resulted in parameter values as shown in Table 4.1. This approach would did not work, given that in CDI system using PR-E, where irreversible non-electrosorption happened predominantly, the assumption of symmetrical adsorption-desorption would result in biased K_a and K_b values applicable for both steps. This is further confirmed by how well the DL model fitted CD-E data, given at this electrode condition, reversible electrosorption was the only sorption mechanism. Given original DL model developed by Nordstrand [1] assuming that all previously adsorbed ions during charging process will eventually desorb during discharging process (i.e., electrosorption only), we argued that working on asymmetrical adsorption-desorption system,

current DL model should fit the adsorption-desorption curves separately, obtaining K_a and K_b optimized for adsorption, and $K_{a'}$ and $K_{b'}$ for desorption cycle.

This approach resulted in 2-part simulation, in which the fitting separately applied to adsorption during charging and desorption during discharging:

During charging, the fitting equations are:

$$\frac{dC_{ads}}{dt} = K_a - K_b C_{ads}$$

$$\frac{dC_{eff}}{dt} = -\frac{dC_{ads}}{dt} + \frac{Q}{v_{cell}}(C_0 - C)$$

At the beginning of charging, no adsorption occurred, i.e., $C_{ads} = 0$. At equilibrium ($dC_{ads}/dt = 0$), C_{ads} reached its maximum, and can be calculated with the following equation:

$$C_{ads} = \frac{K_a}{K_b}$$

While during discharging, the fitting equations are:

$$-\frac{dC_{ads'}}{dt} = K_{a'} - K_{b'} C_{ads}$$

$$\frac{dC_{eff}}{dt} = \frac{dC_{ads'}}{dt} + \frac{Q}{v_{cell}}(C - C_0)$$

Unlike C_{ads} which constitutes total adsorbed ion concentration, $C_{ads'}$ represents only electrosorbed ions onto the electrode. The negative value on $dC_{ads'}/dt$ represents the net negative change in ion concentration on the electrode surface during desorption. $K_{a'}$ and $K_{b'}$ represent fitting parameters applicable only to the discharging only.

At the beginning of discharging, $C_{ads'}$ is at the highest concentration (due to previous adsorption), and can be derived by integrating the above equation:

$$dC_{ads'} = (-K_{a'} + K_{b'}C_{ads'})dt$$

$$\int \frac{1}{-K_{a'} + K_{b'}C_{ads'}} dC_{ads'} = \int dt$$

$$\frac{1}{K_{b'}} ln(-K_{a'} + K_{b'}C_{ads'}) = t$$

$$C_{ads'} = \frac{e^{K_{b'}t} + K_{a'}}{K_{b'}}$$

At $t = 0$,

$$C_{ads} = \frac{1 + K_{a'}}{K_{b'}}$$

On the other hand, at equilibrium ($dC_{ads'}/dt = 0$) of discharging step, all previously electrosorbed ions assumed to be released back onto the bulk, i.e., $C_{ads'} = 0$.

Using this new approach, we could then perform the simulation on each charging and discharging effluent concentration profile using MATLAB to obtain K_a, K_b, $K_{a'}$, $K_{b'}$. Future work can focus on proving this concept and verifying its accuracy.

4.5.2. Modified Donnan with Fused Hard Sphere (FHS) Equation-of-State (EoS)

Figure 4.11 displays the calculated values of IAC from mD model with FHS EoS assumption, compared to the actual performance from experiments. After we calculated $\Delta\mu_{i,j}^{ex}$ using the EoS equation (Eq.4.7), we solved for the concentration of ion in micropores ($c_{mi,i}$) by

solving multiple equations simultaneously. This $c_{mi,i}$ value was then used to calculate the IAC using Eq.4.14 relevant for single-pass continuous CDI operation mode.

From **Figure 4.11(A-B)**, we observed that the calculated IACs from mD-FSH are in good agreement with the electrosorption capacity for CDI treating NaCl or NaHCOO. Across different electrode conditions, IAC for PR-E was calculated slightly higher than ST-E, and ST-E higher than CD-E, although not significant ($p>0.05$). If we looked at the chemical and structural properties of PR-E, ST-E, and CD-E, for electrode pretreated with NaCl or NaHCOO, the change in pores volume (v_{mi}) and surface charge functional group (σ_{chem}) across different electrode conditions (but same solution) were not significant ($p>0.05$). Given that for mD-FSH we input the parameter values into the mathematical model, we expect relatively similar IAC output as a result. Between NaCl and NaHCOO, we did not see significant difference in terms performance, an observation we attributed to the size of the two ions to be similar with indifferent ionic mobility. During CDI experiments, we also monitored the change in anode/cathode potential, and our reading showed that the potential windows for electrosorption between NaCl and NaHCOO and across different electrode conditions are not significantly different. We noticed one key observation pertaining the calculated IAC and experimental IAC comparison, in that our mD model did not factor in ions being adsorbed due to physical/chemical adsorption, especially when physical/chemical adsorption significantly contributed to the overall total IAC. This can be seen by total IAC obtained from experiment of CDI with PR-E being 1.83x larger than calculated IAC for NaCl, and 1.90x larger for NaHCOO respectively. It was previously discussed in mD model development that the excess chemical potential difference ($\Delta\mu_{i,j}^{ex}$) consists of attractive forces between ion and the uncharged part of microporous carbons [30] which should explain the physical/chemical adsorption contribution. However, our results indicated that using relevant

excess potential value did not closely approach the actual total IAC, leaving a portion of IAC unexplained. Further study to investigate the integration of physical/chemical adsorption into mD model is needed to answer this question.

From **Figure 4.11(C)**, we observed a different trend in terms of calculated IAC for CDI treating hexanoate-containing solution, in which IAC values decreases across different electrode conditions. Calculated IACs for CDI treating hexanoate are 0.182 mmol/g-C for PR-E, 0.169 mmol/g-C for ST-E, and 0.146 mmol/g-C for CD-E. This observation actually supports our expectation in which IAC for PR-E should be the highest among three electrode conditions as PR-E has the largest pores volume and its surface was not yet affected by introduction of carboxyl groups by means of physical/chemical adsorption from hexanoate. Previous finding showed that physically/chemically adsorbed modified the surface charge concentration of the electrode to be more negative, which would be contra-productive to adsorbing more hexanoate ions. From the **Figure 4.11(C)** we also observed that generally the calculated IAC values are slightly higher than the electrosorption-IAC from the experiment, a different observation than NaCl and NaHCOO, in which the calculated IACs closely matched experimental electrosorption IAC. We argued that this discrepancy may be due to two possible reasons: 1) the use of alkanes geometrical function as opposed to carboxylate ion, since given the lack of carboxyl groups in alkanes, the shape and size of hexanoate might not be accurately represented by hexane, resulting in an overestimation with regard to electrosorption capacity, and 2) acid-base dissociation of the chemical surface groups, where this reaction is found to affect the performance of CDI and resulting in the mD model to overestimate the predicted performance [31]. Future study would be needed to improve the model and to validate with more experimental data points.

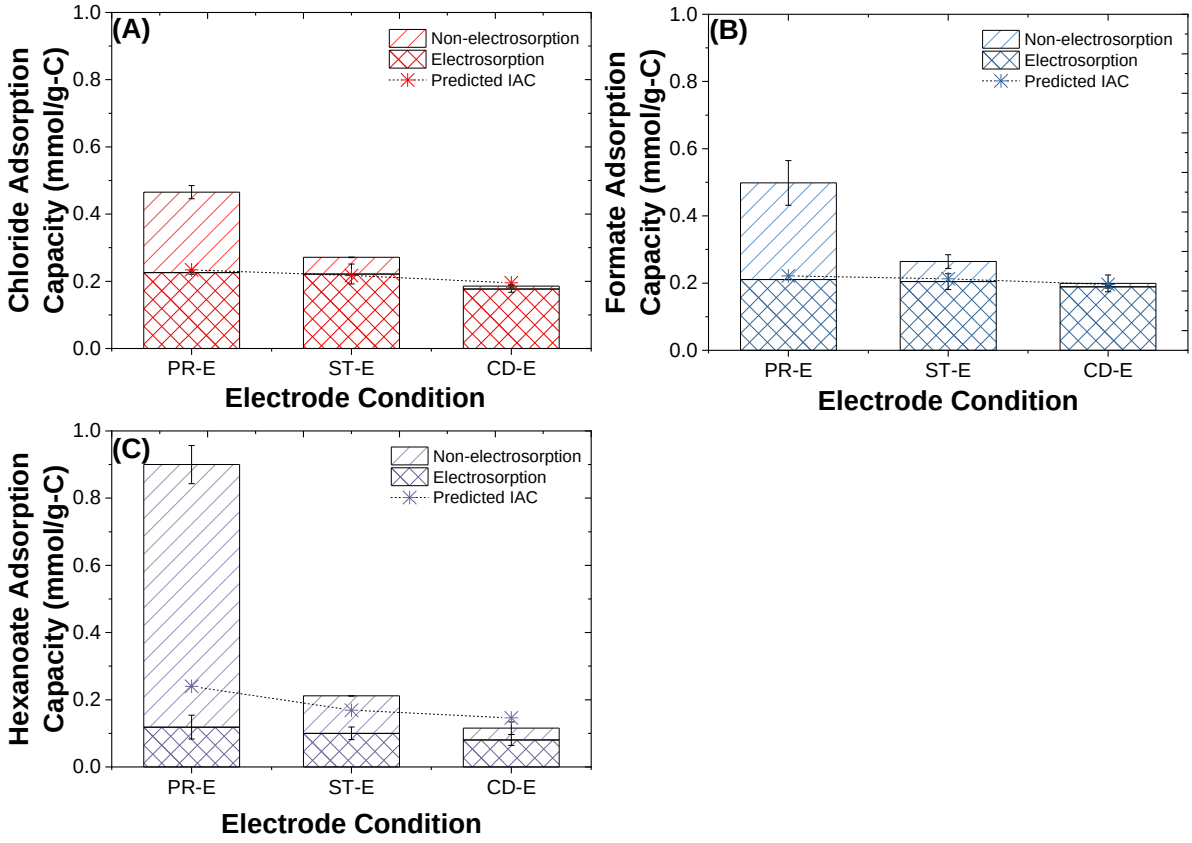

Figure 4.11. Estimated IAC obtained from modified Donnan (mD) model with fused hard-sphere (FSH) equation-of-state (EoS) assumption to calculate excess chemical potential difference between micro and macropores ($\Delta\mu_i^{ex}$). The estimated values from model are calculated using relevant parameters for each ion at different electrode conditions and are compared with the experimental results to verify its accuracy.

4.6. Conclusions

Our overall objective was to develop a mathematical modeling of modified Donnan with fused hard-sphere (FHS) equation-of-state (EoS) as well as proposed grey-box model of dynamic Langmuir (DL) to predict from thermodynamic and kinetic approach the ion adsorption capacity of capacitive deionization (CDI) treating carboxylate-containing solution using carbon electrode at different pretreating condition. The following points summarize our findings:

1. Dynamic Langmuir (DL) was able to model the effluent concentration profile of CDI treating carboxylate-containing solutions using conditioned electrode (CD-E) with good fit and agreement. The DL model was also able to estimate the ion adsorption capacity (IAC) within 5% of the electrosorption capacity from the experiment. Specifically for CDI using CD-E, DL model was validated with other experimental data, showing it can be used to predict CDI performance treating carboxylate-containing solution.
2. Dynamic Langmuir (DL) model could not explain the adsorption capacity due to non-electrosorption interaction. We found that DL has still limitations in explaining the discrepancy in performance of CDI using electrodes at different state of conditions prior to CDI operations (especially for pristine electrode, PR-E). However, we argue that since most CDI operation uses conditioned electrode and not pristine, DL model is still a valuable predictive tool of CDI performances.
3. Modified Donnan (mD-FHS) model developed to predict ion adsorption capacity (IAC) overestimated the electrosorption IAC from experiment but could not explain the contribution of non-electrosorptive interactions likely because of the general assumption made in mD model that interactions between ions and electrode are driven by electrostatic force only, neglecting any physical or chemical attraction which are commonly observed with more complex organic ions.
4. Incorporating physical/chemical adsorption factor into DL model may improve the model ability to predict the total IAC with multiple adsorption mechanisms. We also proposed to modify the simulation approach with the fitting for effluent concentration profile, in which curve fitting should be separately performed for charging and discharging step. On the other hand, further adjustment is needed to improve the overall credibility of mD-

FHS model in predicting the performance of CDI treating organic ions, one of which is to use a more representative structural sizes and shapes of carboxylate ions in order to accurately estimate the performance of CDI using mD model. Strategy to combine physical adsorption isotherm into modified Donnan theory shall be explored for future outlook.

4.7. References

[1] J. Nordstrand, An Extended Randles Circuit and a Systematic Model-Development Approach for Capacitive Deionization An Extended Randles Circuit and a Systematic Model- Development Approach for Capacitive Deionization, (2021). doi:10.1149/1945-7111/abd82f.

[2] J. Nordstrand, J. Dutta, Dynamic Langmuir Model: A Simpler Approach to Modeling Capacitive Deionization, J. Phys. Chem. C. 123 (2019) 16479–16485. doi:10.1021/acs.jpcc.9b04198.

[3] J. Nordstrand, K. Laxman, M.T.Z. Myint, J. Dutta, An Easy-to-Use Tool for Modeling the Dynamics of Capacitive Deionization, J. Phys. Chem. A. 123 (2019) 6628–6634. doi:10.1021/acs.jpca.9b05503.

[4] J. Nordstrand, J. Dutta, Basis and Prospects of Combining Electroadsorption Modeling Approaches for Capacitive Deionization, (2020) 309–324.

[5] J. Nordstrand, J. Dutta, Flexible modeling and control of capacitive-deionization processes through a linear-state-space dynamic Langmuir model, Npj Clean Water. 4 (2021) 1–7. doi:10.1038/s41545-020-00094-y.

[6] J. Nordstrand, J. Dutta, Predicting and Enhancing the Ion Selectivity in Multi-Ion Capacitive Deionization, Langmuir. 36 (2020) 8476–8484. doi:10.1021/acs.langmuir.0c00982.

[7] Z. Wang, L. Yue, Z.T. Liu, Z.H. Liu, Z. Hao, Functional graphene nanocomposite as an electrode for the capacitive removal of FeCl 3 from water, J. Mater. Chem. 22 (2012) 14101–14107. doi:10.1039/c2jm32175k.

[8] S. Yao, X. Ding, Y. Ji, X. Kan, R. Liu, Pore Scale Study of Dynamic Adsorption Process in Capacitive deionization Porous Electrode Based on Lattice Boltzmann Method, Int. J. Electrochem. Sci. 16 (2021) 1–18. doi:10.20964/2021.08.16.

[9] Y. Han, X. Quan, X. Ruan, W. Zhang, Integrated electrochemically enhanced adsorption with electrochemical regeneration for removal of acid orange 7 using activated carbon fibers, Sep. Purif. Technol. 59 (2008) 43–49. doi:10.1016/j.seppur.2007.05.026.

[10] X. Gao, S. Porada, A. Omosebi, K. Liu, P.M. Biesheuvel, J. Landon, Complementary surface charge for enhanced capacitive deionization, Water Res. 92 (2016) 275–282. doi:10.1016/j.watres.2016.01.048.

[11] W. Tang, P. Kovalsky, B. Cao, T.D. Waite, Investigation of fluoride removal from low-salinity groundwater by single-pass constant-voltage capacitive deionization, Water Res. 99 (2016) 112–121. doi:10.1016/j.watres.2016.04.047.

[12] S. Mao, L. Chen, Y. Zhang, Z. Li, Z. Ni, Z. Sun, R. Zhao, Fractionation of mono- and divalent ions by capacitive deionization with nanofiltration membrane, J. Colloid Interface Sci. 544 (2019) 321–328. doi:10.1016/j.jcis.2019.02.093.

[13] W. Tang, P. Kovalsky, D. He, T.D. Waite, Fluoride and nitrate removal from brackish groundwaters by batch-mode capacitive deionization, Water Res. 84 (2015) 342–349. doi:10.1016/j.watres.2015.08.012.

[14] S. Porada, M. Bryjak, A. Van Der Wal, P.M. Biesheuvel, Effect of electrode thickness variation on operation of capacitive deionization, Electrochim. Acta. 75 (2012) 148–156. doi:10.1016/j.electacta.2012.04.083.

[15] A. Rommerskirchen, B. Ohs, K.A. Hepp, R. Femmer, M. Wessling, Modeling continuous

flow-electrode capacitive deionization processes with ion-exchange membranes, J. Memb. Sci. 546 (2018) 188–196. doi:10.1016/j.memsci.2017.10.026.

[16] A. Hemmatifar, D.I. Oyarzun, J.W. Palko, S.A. Hawks, M. Stadermann, J.G. Santiago, Equilibria model for pH variations and ion adsorption in capacitive deionization electrodes, Water Res. 122 (2017) 387–397. doi:10.1016/j.watres.2017.05.036.

[17] A. Kalfa, I. Cohen, E. Avraham, D. Aurbach, The Ratio between the Surface Charge and Electrode's Capacitance as a Fast Tool for Assessing the Charge Efficiency in Capacitive Deionization Processes, J. Electrochem. Soc. 166 (2019) H119–H125. doi:10.1149/2.0221904jes.

[18] E.N. Guyes, A.N. Shocron, A. Simanovski, P.M. Biesheuvel, M.E. Suss, A one-dimensional model for water desalination by flow-through electrode capacitive deionization, Desalination. 415 (2017) 8–13. doi:10.1016/j.desal.2017.03.013.

[19] S. Porada, L. Borchardt, M. Oschatz, M. Bryjak, J.S. Atchison, K.J. Keesman, S. Kaskel, P.M. Biesheuvel, V. Presser, Direct prediction of the desalination performance of porous carbon electrodes for capacitive deionization, Energy Environ. Sci. 6 (2013) 3700–3712. doi:10.1039/c3ee42209g.

[20] L. Wang, P.M. Biesheuvel, S. Lin, Reversible thermodynamic cycle analysis for capacitive deionization with modified Donnan model, J. Colloid Interface Sci. 512 (2018) 522–528. doi:10.1016/j.jcis.2017.10.060.

[21] P.M. Biesheuvel, R. Zhao, S. Porada, A. van der Wal, Theory of membrane capacitive deionization including the effect of the electrode pore space, J. Colloid Interface Sci. 360 (2011) 239–248. doi:10.1016/j.jcis.2011.04.049.

[22] M.E. Suss, Size-Based Ion Selectivity of Micropore Electric Double Layers in Capacitive Deionization Electrodes, J. Electrochem. Soc. 164 (2017) E270–E275. doi:10.1149/2.1201709jes.

[23] E.N. Guyes, T. Malka, M.E. Suss, Enhancing the ion-size-based selectivity of capacitive deionization electrodes, Environ. Sci. Technol. 53 (2019) 8447–8454. doi:10.1021/acs.est.8b06954.

[24] S.Y. Huang, C.S. Fan, C.H. Hou, Electro-enhanced removal of copper ions from aqueous solutions by capacitive deionization, J. Hazard. Mater. 278 (2014) 8–15. doi:10.1016/j.jhazmat.2014.05.074.

[25] A. Suresh, G.T. Hill, E. Hoenig, C. Liu, Electrochemically mediated deionization: A review, Mol. Syst. Des. Eng. 6 (2021) 25–51. doi:10.1039/d0me00090f.

[26] W. Xiaobing, L. Jinqiu, L. Yang, L. Sen, L. Dong, M. Tingting, J. An, H. Yanshe, G. Fengwei, Numerical Analysis of Capacitive Deionization Process Using Activated Carbon Electrodes, Water. Air. Soil Pollut. 232 (2021). doi:10.1007/s11270-021-05320-y.

[27] T. Boublík, Equation of state of linear fused hard-sphere models, 8976 (2006). doi:10.1080/00268978900102051.

[28] J. Jirsák, T. Boublík, Enthalpies of vaporization of n-alkanes from the enlarged fused hard sphere model, Fluid Phase Equilib. 226 (2004) 295–300. doi:10.1016/j.fluid.2004.08.035.

[29] J. Nordstrand, J. Dutta, Simplified Prediction of Ion Removal in Capacitive Deionization of Multi-Ion Solutions, (2020). doi:10.1021/acs.langmuir.9b03571.

[30] P.M. Biesheuvel, S. Porada, M. Levi, M.Z. Bazant, Attractive forces in microporous carbon electrodes for capacitive deionization, J. Solid State Electrochem. 18 (2014) 1365–

1376. doi:10.1007/s10008-014-2383-5.

[31] L. Legrand, Q. Shu, M. Tedesco, J.E. Dykstra, H.V.M. Hamelers, Role of ion exchange membranes and capacitive electrodes in membrane capacitive deionization (MCDI) for CO2 capture, J. Colloid Interface Sci. 564 (2020) 478–490. doi:10.1016/j.jcis.2019.12.039.

APPENDICES

APPENDIX A. Supplementary information for Chapter 2

A.1. Linear Correlation between ionic conductivity and specific capacitance from CV measurement using 3-electrode setup

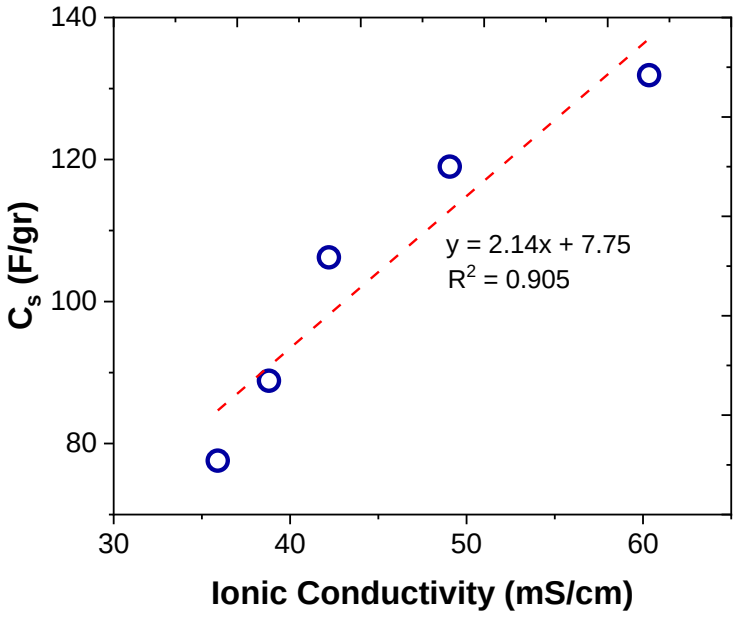

Figure A.1. Correlation between ionic conductivity and specific capacitance calculated from CV curve using 3-electrode setup

A.2. Component resistance for every solution measured with EIS in 3-electrode setup

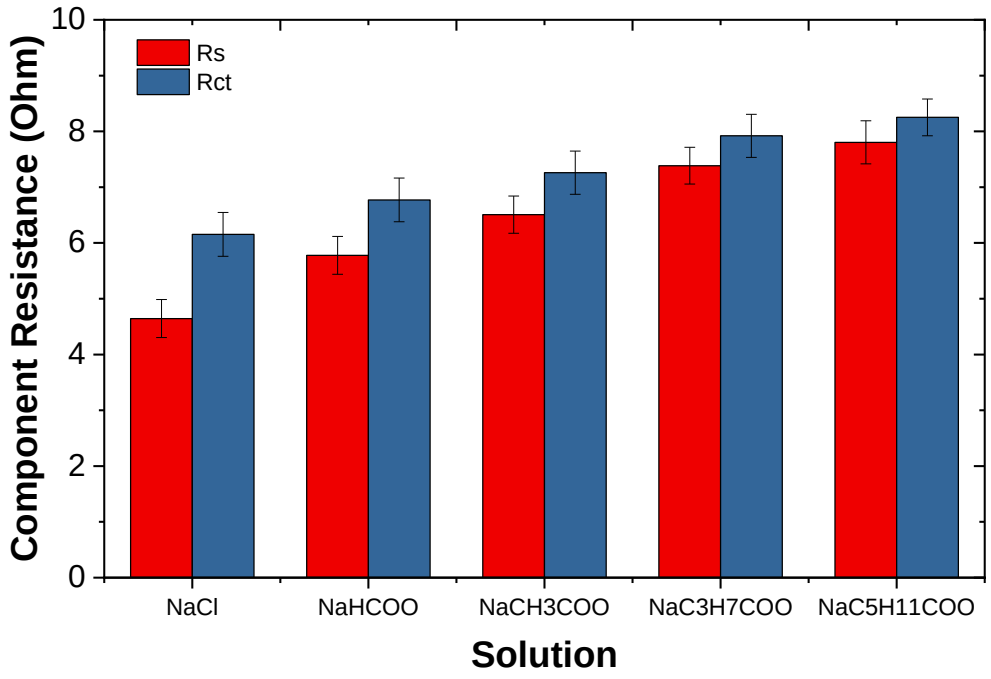

Figure A.2. Component resistance for solutions measured with EIS in 3-electrode cell setup. R_s represents the setup resistance which includes ionic solution and wire resistances. R_{ct} represents the charge transfer resistance between the electrolyte and electrode. Error bars represent the standard deviation of triplicate experiments (n = 3)

A.3. Capacitive and parasitic charge of CDI during charging and discharging

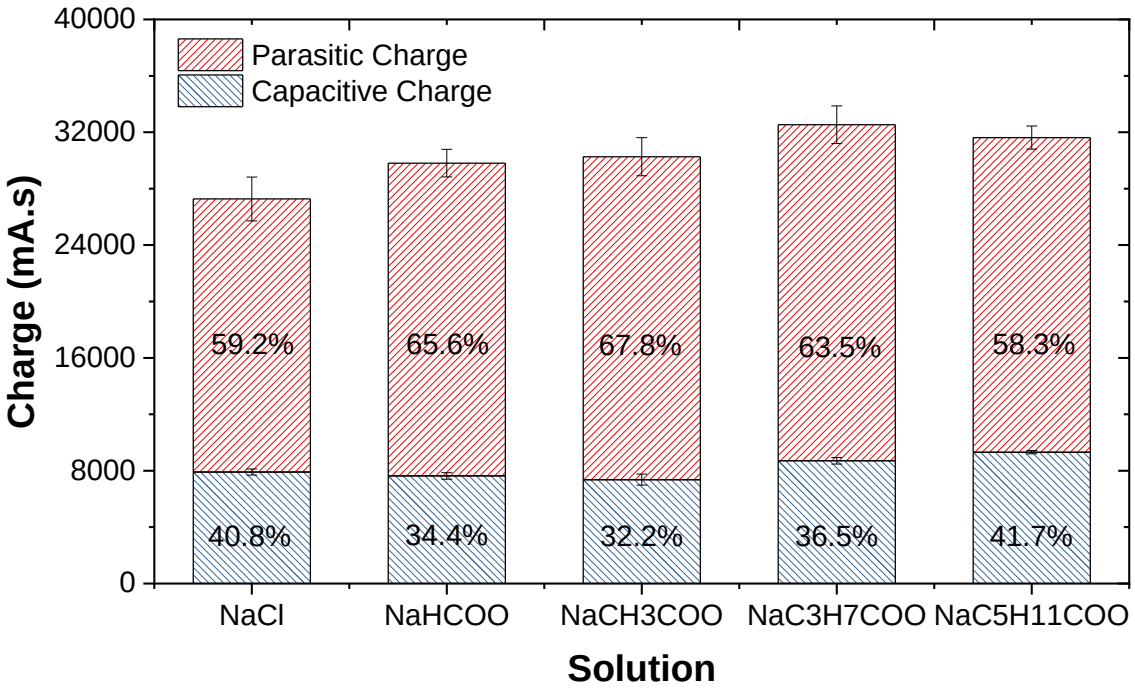

Figure A.3 Parasitic and capacitive charge during CDI experiment for different feed solution. The % values represent the percentage of each component charge from the total. Error bars represent the standard deviation of triplicate experiments (n = 3)

A.4. Sodium electrosorption capacity compared to its anion counterparts

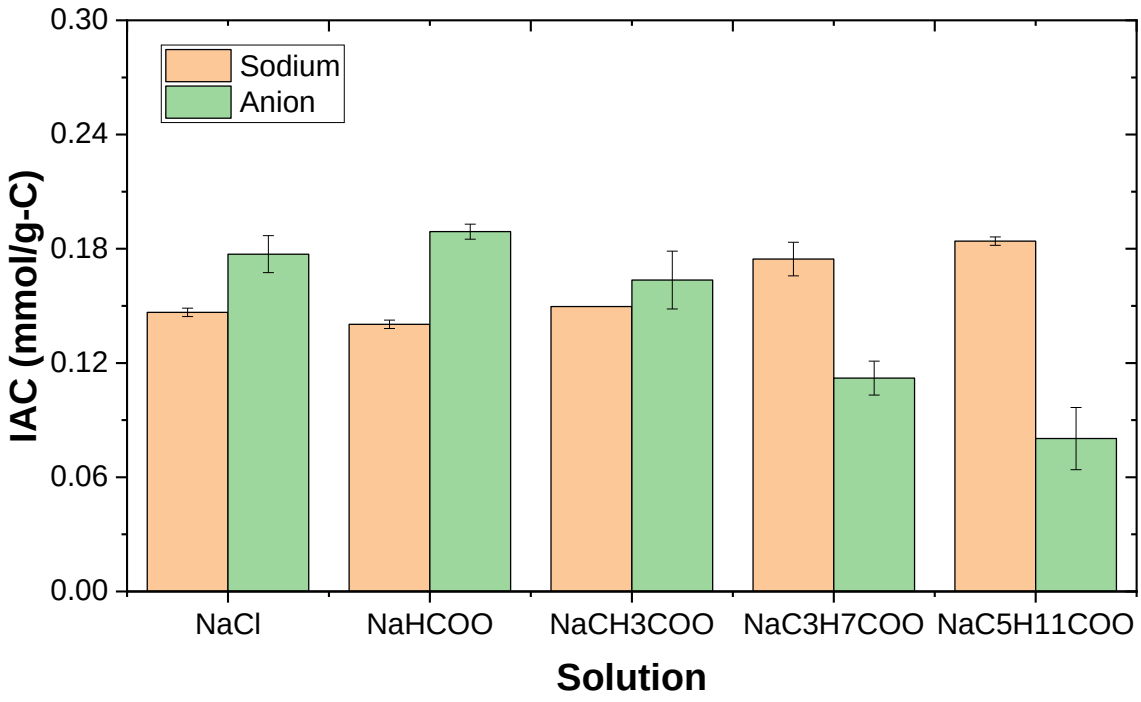

Figure A.4 Ion adsorption capacity of anions and its sodium counterpart. Parasitic and capacitive charge during CDI experiment for different feed solution. The % values represent the percentage of each component charge from the total. Error bars represent the standard deviation of triplicate experiments (n = 3)

A.5. Effluent pH reading during charging and discharging of CDI experiment

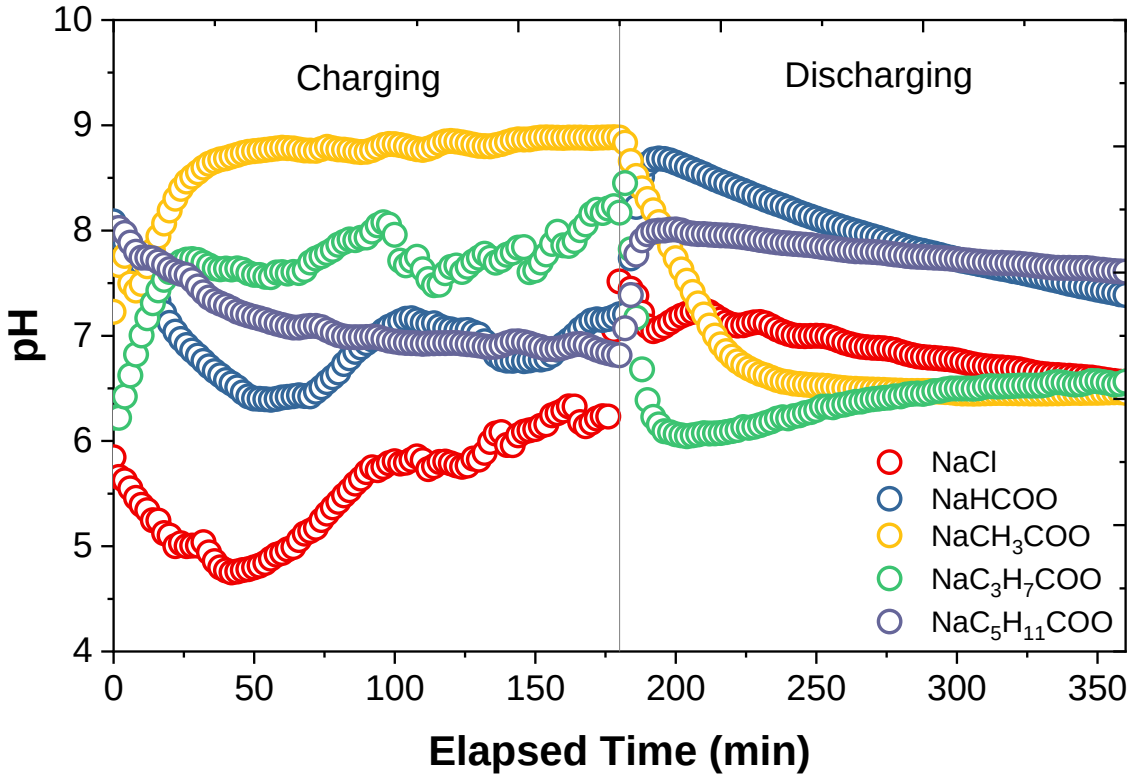

Figure A.5. Effluent pH reading during charging and discharging of CDI experiment. Solid gray line refers to the switch time between charging and discharging

APPENDIX B. Supplementary information for Chapter 3

B.1. Relationship between the C-number of carboxylate ions used in CDI study with total IAC

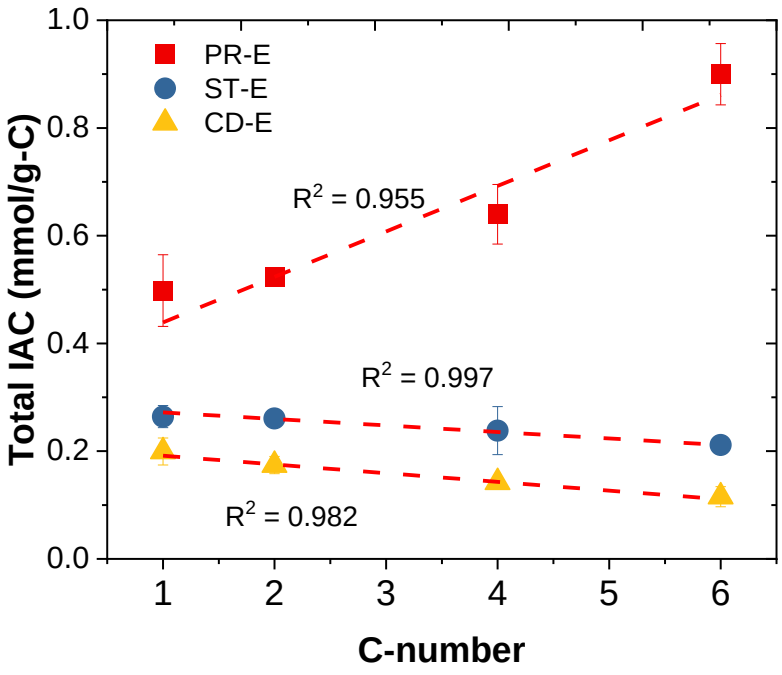

Figure B.1. Correlation between Total IAC and carbon number of carboxylate ions used in this CDI study. Red dashed lines represent the linear regression line. Error bars represent the standard deviation of triplicate experiments (n = 3)

B.2. Profile of effluent pH during charging and discharging of CDI using electrodes at different conditions

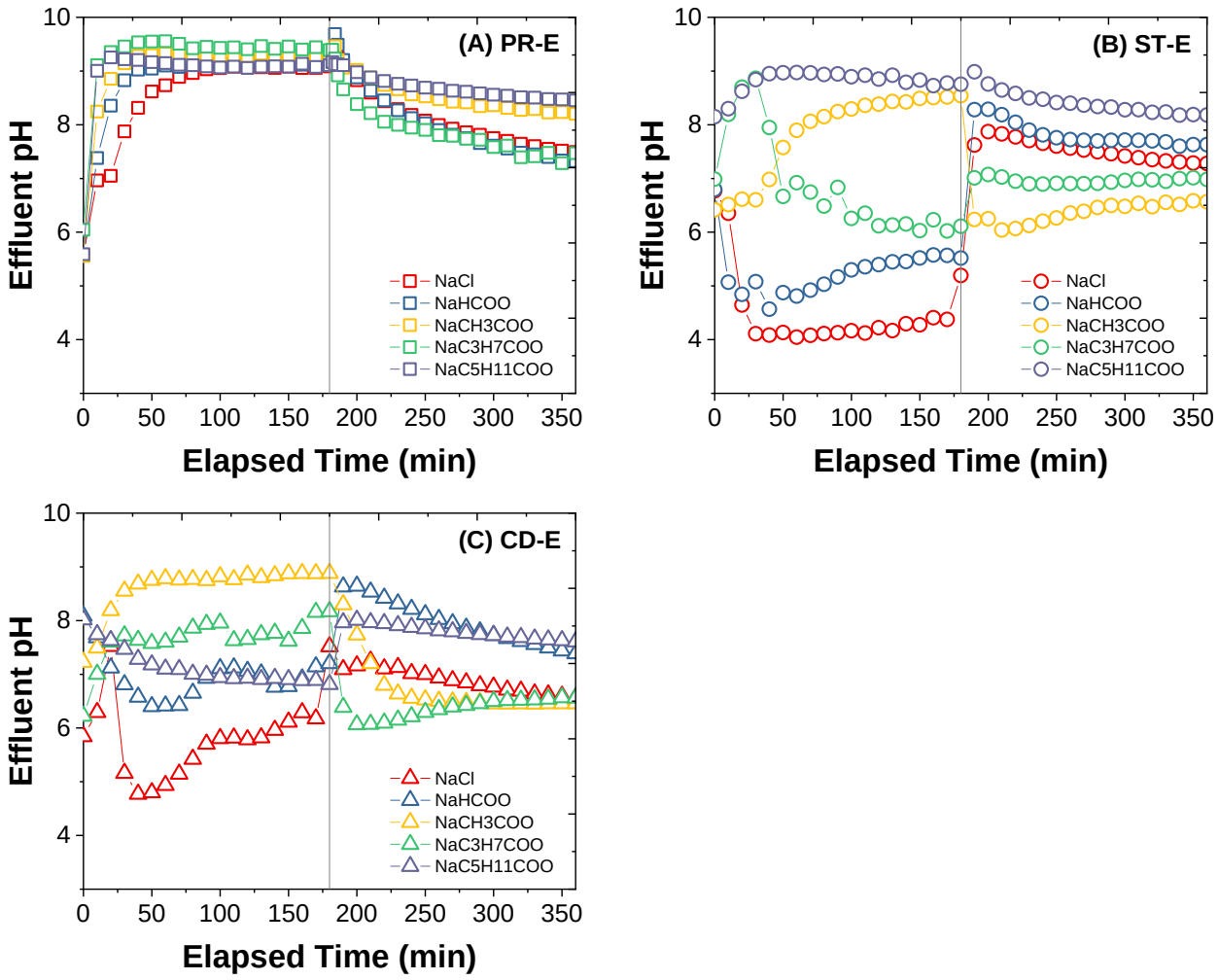

Figure B.2. Profile of effluent pH during charging and discharging of CDI treating organic solutions using: (A) pristine electrodes (PR-E), (B) saturated electrodes (ST-E), and (C) conditioned electrodes (CD-E)

B.3. Profile of effluent pH during charging and discharging of CDI using electrodes at different conditions

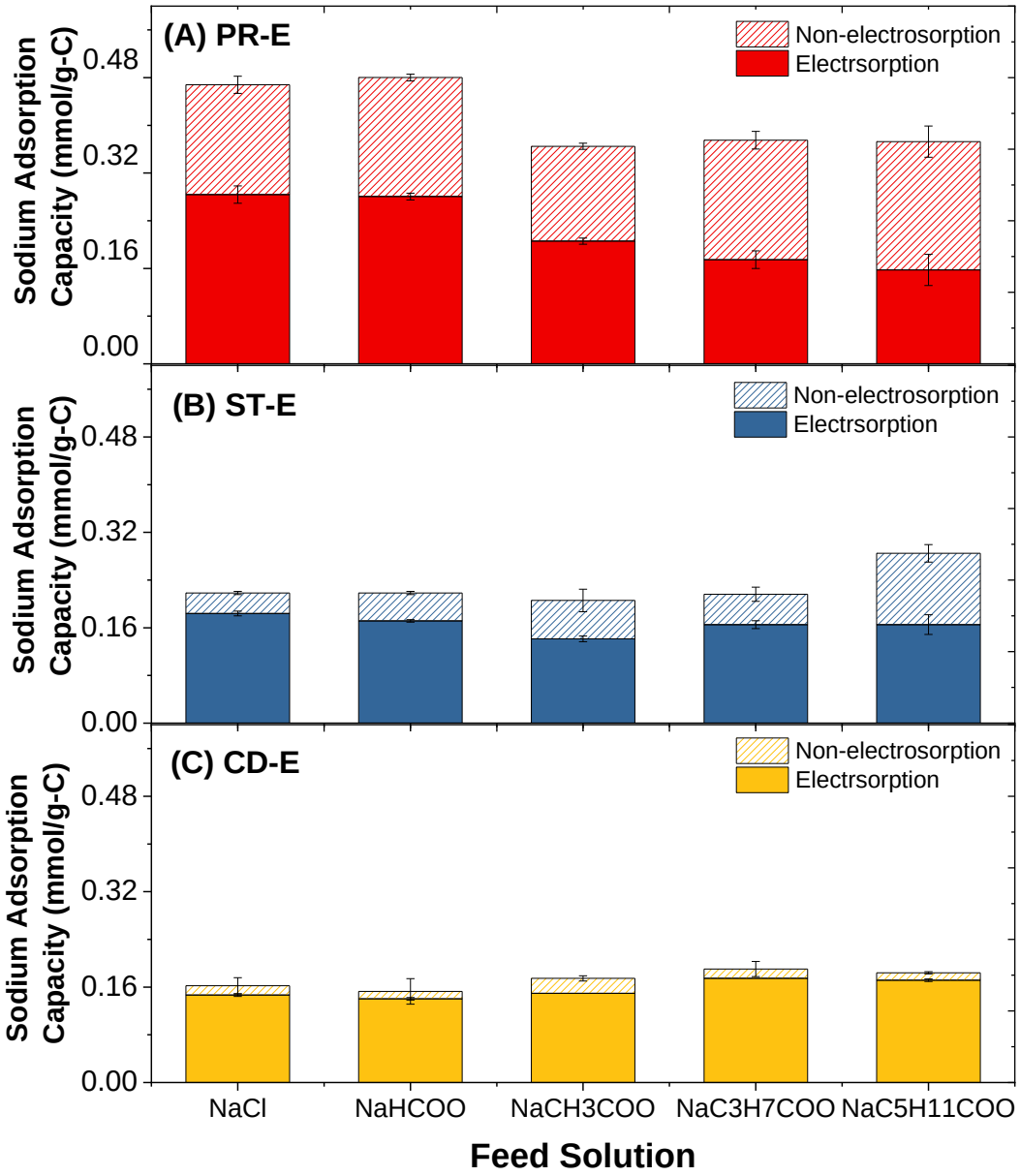

Figure B.3. Sodium adsorption capacity of CDI treating organic solutions using: (A) pristine electrodes (PR-E), (B) saturated electrodes (ST-E), and (C) conditioned electrodes (CD-E). Error bars represent the standard deviation of triplicate experiments (n = 3)

APPENDIX C. Supplementary information for Chapter 4

C.1. Source code for the fitting of dynamic Langmuir (DL) model

Configuration file

```
function Config = config()

ConFiguredataFileName = "D:\Dynamic Langmuir model\Data\chloride_a.txt";

ConFigurebatch = false;

ConFigureflow = 3/11.02/60;

ConFigurec0 = 5;

ConFigurepredict = false;

ConFigureKaStart = 0.1;

ConFigureKbStart = 0.0075;

ConFigureon = [0 10800];

ConFigurerepeatedCycles = false;

ConFiguretSample = 12;

ConFiguredataLabel = "ST-E for NaCl";


end
```

Equation file

```
function [dx,y] = equation(t,x,u,Ka,Kb,flow,c0,onMatrix,repeat,batch,...
                                                                varargin)

    nDataSet = length(flow);

    y  = zeros(nDataSet,1);

    dx = zeros(nDataSet*2,0);

    isOn = isonfunction(onMatrix,repeat,nDataSet,t);

    for i=1:nDataSet
```

```
    index = 2*i-1;
    dc       = -Ka*isOn{i} + Kb*x(index+1) - flow(i)*(x(index)-c0(i));
    dc_ads   =  Ka*isOn{i} - Kb*x(index+1);

    dx(index:index+1)   = [dc;dc_ads];
    if batch
        y(i) = -x(index+1)+c0;
    else
        y(i) = x(index);
    end
end
function isOn = isonfunction(onMatrix,repeat,nDataSet,t)
    for n = 1:nDataSet
        ind = 2*n-1;
        if repeat
            isOn{n} = mod(t,sum(onMatrix(ind:ind+1))) < onMatrix(ind);
        else
            if min(size(onMatrix)) == 1
                isOn{n} = (t>onMatrix(ind)) && (t<onMatrix(ind+1));
            else
                isOn{n} = 0;
                for j = 1:size(onMatrix,1
                    isOn{n} = isOn{n} || (t>onMatrix(j,ind)) && ...
                                         (t<onMatrix(j,ind+1));
                end
            end
        end
    end
end
```

```
end
```

Main file

```
function out = main()
Config = config();
yData = load(ConFiguredataFileName);
if ConFigurebatch
    yData  = yData.*ConFigurec0./yData(1);
else
    yData  = yData.*ConFigurec0./yData(1800);
end
nDataSet = size(yData,2);
parameters = {ConFigureKaStart,ConFigureKbStart,ConFigureflow, ...
    ConFigurec0,ConFigureon,ConFigurerepeatedCycles*1,ConFigurebatch*1};

data = iddata(yData,[],ConFiguretSample,'Name','Salt');
order = [1 0 2]*nDataSet;
Ts = 0;
tmp = [ConFigurec0;zeros(1,length(ConFigurec0))];
initial_states = tmp(:);
fileName = 'equation';
model = idnlgrey(fileName, order, parameters, initial_states, Ts,...
                 'Name','Salt');
if ConFigurepredict
    setpar(model,'Fixed', {true,true,true,true,true,true,true});
else
    setpar(model,'Fixed', {false,false,true,true,true,true,true});
end
opt = nlgreyestOptions('Display', 'Full');
```

```
opt.Regularization.Lambda = 0;
opt.SearchOptions.Advanced.MaxIter=100;

FinalModel = nlgreyest(data,model,opt);

out.KaEst = FinalModel.Parameters(1).Value;
out.KbEst = FinalModel.Parameters(2).Value;
[y,~,~] = compare(data,FinalModel);

Tmin = 1; Tmax = size(yData,1);
for i=1:nDataSet
    Figure;
    plot((Tmin:Tmax)*ConFiguretSample,yData(Tmin:Tmax,i),...
         (Tmin:Tmax)*ConFiguretSample,y.OutputData(Tmin:Tmax,i),'LineWidth',2);
    xlabel('Elapsed Time (sec)')
    ylabel('Ce (mM)')
    if ConFigurepredict
        legend('Experiment','Model predicted')
    else
        legend('Experiment','Model fitted')
    end
    if isfield(Config,'dataLabel')
        title(ConFiguredataLabel(i))
    end
end
end
```

C.2. Source code for solving multivariate multi equations for modified Donnan (mD)

```
syms cmi1C cma1C cmi2C cma2C cmi1A cma1A cmi2A cma2A miu1C miu2C miu1A miu2A z1 z2 mC
mA vmiC vmiA PhiDC PhiDA sigmaelecC sigmaelecA sigmaionC sigmaionA sigmachemC
sigmachemA PhiC PhiA PhimaC PhimaA PhiSC PhiSA F VT Cs

cma1C = 0.005;

cma2C = 0.005;

cma1A = 0.005;

cma2A = 0.005;

miu1C = 0.000578668;

miu2C = 0.000461497;

miu1A = 0.000578668;

miu2A = 0.000461497;

z1 = 1;

z2 = -1;

mC = 0.1848;

mA = 0.1848;

vmiC = 0.000774;

vmiA = 0.000774;

PhimaC = 0;

PhimaA = 0;

Vapp = 1.2;

VT = 0.02568;

Phi = Vapp / VT;

F = 96485;

Cs = 135000;

sigmachemC = 0;

sigmachemA = 0;


eqn1 = log(cmi1C) - log(cma1C) + miu1C + (z1 * PhiDC) == 0;
```

```
eqn2 = log(cmi2C) - log(cma2C) + miu2C + (z2 * PhiDC) == 0;

eqn3 = log(cmi1A) - log(cma1A) + miu1A + (z1 * PhiDA) == 0;

eqn4 = log(cmi2A) - log(cma2A) + miu2A + (z2 * PhiDA) == 0;

eqn5 = sigmaelecC + sigmaionC + sigmachemC == 0;

eqn6 = sigmaelecA + sigmaionA + sigmachemA == 0;

eqn7 = sigmaionC - cmi1C + cmi2C == 0;

eqn8 = sigmaionA - cmi1A + cmi2A == 0;

eqn9 = PhiC - PhimaC - PhiDC - PhiSC == 0;

eqn10 = PhiA - PhimaA - PhiDA - PhiSA == 0;

eqn11 = PhiSC + ((F / (VT * Cs)) * (sigmaionC + sigmachemC)) == 0;

eqn12 = PhiSA +((F / (VT * Cs)) * (sigmaionA + sigmachemA)) == 0;

eqn13 = (mC * vmiC * sigmaelecC) + (mA * vmiA * sigmaelecA) == 0;

eqn14 = Phi - PhiA + PhiC == 0;


sol = vpasolve(eqn1, eqn2, eqn3, eqn4, eqn5, eqn6, eqn7, eqn8, eqn9, eqn10, eqn11,
eqn12, eqn13, eqn14, cmi1C, cmi2C, cmi1A, cmi2A, PhiDC, PhiDA, sigmaelecC,
sigmaelecA, sigmaionC, sigmaionA, PhiC, PhiA, PhiSC, PhiSA);

xsol = sol.cmi1C

ysol = sol.cmi2C

wsol = sol.cmi1A

zsol = sol.cmi2A
```

APPENDIX D. Published article

Hossen, E.H., Gobetz, Z.E., Kingsbury R.S., Liu F., Palko, H.C., Dubbs, L.L., Coronell, O., Call, D.F. Temporal variation of power production via reverse electrodialysis using coastal North Carolina waters and its correlation to temperature and conductivity. Desalination, 491 (2020) 114562.

Temporal Variation of Power Production via Reverse Electrodialysis using Coastal North Carolina Waters and its Correlation to Temperature and Conductivity

Elvin H. Hossen[1], Zoe E. Gobetz[2], Ryan S. Kingsbury[3], Fei Liu[3], Hannah C. Palko[4], Lindsay L. Dubbs[4], Orlando Coronell[3], Douglas F. Call[1]*

[1]Department of Civil, Construction, and Environmental Engineering, North Carolina State University, Campus Box 7908, Raleigh, USA

[2]Department of Chemical and Biomolecular Engineering, North Carolina State University, Campus Box 7612, Raleigh, USA

[3]Department of Environmental Science and Engineering, Gillings School of Global Public Health, The University of North Carolina at Chapel Hill, Chapel Hill, USA

[4]Coastal Studies Institute, The University of North Carolina at Chapel Hill, Wanchese, USA

*Corresponding author: Douglas F. Call, dfcall@ncsu.edu

Abstract

Global estimates of electricity generation from coastal salinity gradient energy resources rely on the underlying assumption that these gradients are spatially and temporally stable. Refining these estimates requires a better understanding of coastal variations in water properties and their impact on power production. This study investigated power output in reverse electrodialysis (RED) cells by coupling seawater samples collected from three different sites along coastal

North Carolina at five different sampling dates between 2016 and 2017 with wastewater effluent from a wastewater treatment facility as the dilute solution. We found that power density did not vary substantially across the sampling dates except for one notable drop in power for a sample collected during an approaching hurricane. For all sites, power output peaked during the summer season. Using our experimental results, we developed a semi-empirical predictive model of RED power output as a function of temperature and conductivity. The model was able to predict power density within approximately 20% of the experimental power densities for the seawater samples used in this study and others in the literature. Combining our modeling approach with temporal conductivity and temperature data may help identify promising sites for coastal salinity gradient energy installations.

Keywords: salinity gradient energy, reverse electrodialysis, temporal variation, predictive model

1. Introduction

Electricity can be generated from the controlled mixing of coastal salinity gradient energy (SGE) resources [1–3]. Estimates of electricity production from mixing seawater and river water range from 0.23 to 3.13 TW [4–7], which is equivalent to 64% of global electricity consumption in 2017 [8]. These estimates are typically based on average ocean and freshwater salinities and freshwater flowrates (e.g., river flow) that are assumed to remain constant over time [3,9]. The maximum theoretical energy recovery of 1.4 $MJ.m^{-3}$ is often applied as well (i.e., when 1 m^3 each of seawater and freshwater are mixed) [9–11]. Some estimates have been refined by considering technical limitations relevant to actual energy conversion of SGE (e.g., efficiency losses) [3,12].

The accessibility and variability of SGE resources are important to consider when making energy recovery predictions. Alvarez-Silva et al. [13] developed global estimates of recoverable SGE resources at river mouths by taking into account variability in water quality, river discharge rates, and limitations imposed by potential environmental impacts of the technology. The constraints they considered resulted in a significantly lower estimate of electricity recovery potential, reaching only 3% of global electricity consumption [13]. In a separate study, Alvarez-Silva et al. [14] showed that strong tidal fluctuations can change the spatiotemporal variability of salinity gradients at river mouths, reducing SGE power predictions to 0.2% of the theoretical potential. A study by Reyes-Mendoza et al. [15] analyzed the seasonal climatology and thermohaline structure of tropical coastal lagoon over the course of one year and showed that the theoretical SGE potential from mixing energy was affected by the variability of atmospheric environmental forces and the seasonality of the region.

Experimentally determining power output from real SGE resources can help refine predictions because they capture natural water quality variations that affect SGE conversion to electricity. In an SGE technology such as reverse electrodialysis (RED), variations in the magnitude of the salinity gradient, water temperature, natural organic matter (NOM), and ionic composition, can impact ion exchange membrane performance, and in turn, power output [16–18]. These water quality properties may change as a result of natural and anthropogenic drivers [19]. Storm events and tidal changes may affect salinity gradient strength and composition, atmospheric factors such as wind speed, air pressure and temperatures always depend on annual cycles of geophysical phenomenon, water temperatures can vary across the seasons, and biological growth and/or accumulation of NOM can fluctuate as a result of temperature and nutrient discharges from point and non-point sources [15,19–21].

Many SGE studies extrapolated power predictions from one-time samples [16,17,22] or short (1-2 month) [23–27] operational periods, which limits their ability to capture temporal variations. Using a real water collected from a one-time sampling event, Pawlowski et al. [28] developed a mechanistic model to predict RED power output by taking into account operating parameters, such as flow rate, and water properties, including conductivity and temperature. Such models are a starting point for power predictions, but efforts to capture natural temporal variations in water quality properties are needed to advance these models. Additionally, models that can use readily obtainable inputs, such as conductivity and temperature, to approximate power output without full characterization of water quality (e.g., inorganic and organic constituents) could help with the selection of promising SGE recovery installations.

The objective of this study was to build upon prior efforts to predict power output from SGE resources by taking into consideration temporal changes in field-measurable properties of coastal seawater, specifically conductivity and temperature. Using RED as a representative SGE technology, we tested seawater samples collected from three different sites along coastal North Carolina (NC) on five different dates between 2016 and 2017. We coupled these waters with a low-salinity water [i.e., treated wastewater effluent from a coastal wastewater treatment plant (WWTP)] as the dilute solution and focused on how seawater temperature and conductivity influenced power production. We used these two metrics, which can be readily measured in the field with low-cost equipment, to develop a semi-empirical predictive model and validated it using data from previous studies that used real waters. Our findings show that power output was generally stable across the sampling dates, except during warmer months when power increased and after excessive rainfall from a hurricane that led to a drop in power at one site. Additionally, the model was able to predict power output for real waters within ~20% of experimental values,

suggesting that temperature and conductivity data from coastal zones may be useful for refining global electricity estimates from SGE resources.

2. Materials and Methods

2.1 Water sources

Seawater samples were collected from three different sites on the NC coast. The sites were located in the southeastern part of the coast at Bogue Sound (BS) near Indian Beach, Nelson Bay (NB), and Taylor's Creek (TC) (**Figure1**). Seawater from each site was collected on five different dates in 2016 (July 27-29, September 21-22, November 13-14) and 2017 (February 3, April 26-27). Treated wastewater (WW) effluent, which served as the dilute water for all tests, was obtained from a one-time collection (April 26, 2017) at the Beaufort WWTP in Beaufort, NC. Using a single dilute water allowed us to focus on how variation in seawater properties affected RED performance. Since the same dilute solution (domestic WW effluent) was paired with each seawater sample, we report the seawater sample site abbreviation (e.g., BS) to reduce redundancy, rather than the seawater/wastewater pair (e.g., BS/WW) that is conventionally used in the literature.

During collection, the seawater samples were analyzed for temperature and conductivity (YSI model 6560 Conductivity/Temperature probe, YSI Inc., Yellow Springs, OH), and pH (YSI model 6565 pH probe, YSI Inc., Yellow Springs, OH) (**Table S1**). The properties of the WW were measured after the sample arrived at the lab. In the lab, all samples were filtered through 10 μm polypropylene felt filters (McMaster Carr, Atlanta, GA) to remove suspended particles and then transferred to headspace-free plastic containers. Samples were stored at 4°C until needed for the RED tests. Prior to each test, the seawater samples were adjusted to the temperature that was

recorded in the field using a temperature-controlled water bath (Model G76D, New Brunswick Scientific, Enfield, CT), and the conductivity was again measured to represent the temperature-corrected values. The WW sample was adjusted to the same temperature as the seawater to eliminate temperature gradients within the membrane stack.

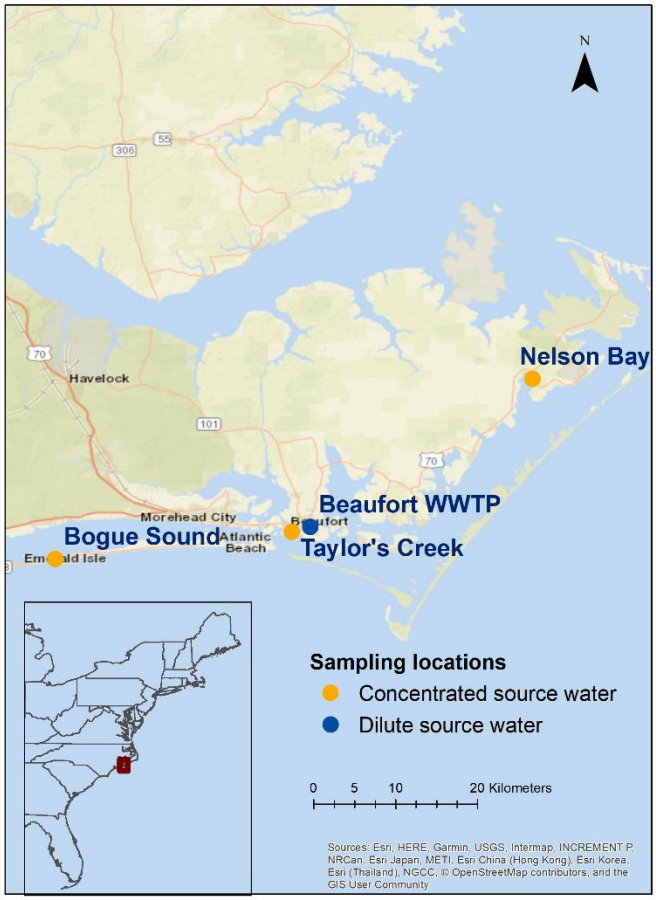

Figure 1. Map of North Carolina showing the location of the three seawater sampling sites at Nelson Bay, Bogue Sound, and Taylor's Creek. The dilute water sample that was used in all tests was obtained from the Beaufort wastewater treatment plant (WWTP) in April 2017.

2.2 Reverse electrodialysis cell design and operation

A commercially available electrodialysis cell (model 64002; PCCell GmbH, Germany) was used for the RED tests (**Figure S1**). The membrane stack consisted of five pairs of cation

exchange membranes (CEMs; PC-SA, PCA GmbH, Germany) and anion exchange membranes (AEMs; PC-SK, PCA GmbH, Germany) with a projected area of 64 cm^2, each separated by rubber gaskets and spacers (0.45 mm in thickness, 60% porosity). At both ends of the membrane stack, reference electrodes (Ag/AgCl; BaSi, Inc. RE-5B, West Lafayette, IN) were installed to measure the voltage across the membrane stack. The anode and cathode electrodes, located at opposite ends of the stack, were Pt/Ir-coated titanium and V4A steel, respectively. A solution of NaCl (30 $g.L^{-1}$) was continuously recirculated through the compartments containing the reference electrodes and anode/cathode. The interior membrane stack was shielded from Cl_2 and H_2 gases (generated at the anode and cathode, respectively) by an additional CEM placed adjacent to the electrode compartment [16,29,30].

During RED operation, both the seawater and WW were continuously pumped through the membrane stack at a constant flow rate (107 $mL.min^{-1}$), which corresponded to a crossflow velocity of 0.99 $cm.s^{-1}$ (calculated as $v = Q/(N_i.A)$, where Q is the flow rate, N_i is the total number of concentrated or dilute solution compartment, and A is the cross sectional area of each compartment). We selected this value because previous studies reported that velocities between 0.5 and 1.0 cm/s provided a good balance between maximizing power output and minimizing pumping losses [31–33] . Prior to testing a new water sample, the membrane stack and electrode compartments were cleaned by flushing first with deionized water, then 10% HCl for 15 min, then1% NaOH for 15 min, and finally with deionized water. After this cleaning procedure, approximately 250 mL each of the seawater and WW samples were flushed and recirculated for 15 minutes in their respective compartments. Afterwards, the recirculated seawater and WW were replaced, and the recirculation mode was switched to single-pass using counter-current flow at a rate of 107 $mL.min^{-1}$. We chose counter-current flow mode due to its advantage over co-current mode in improving the energy efficiency of RED [34]. For each water pair, the

electrochemical performance was first measured at zero current (i.e., open circuit conditions) for one minute and then at seven constant-current steps that spanned a range over which the maximum power density for each sample occurred. Each current step was held for 45 s using a potentiostat (VMP3, Bio-Logic Science Instruments, France). This experimental procedure was performed twice for each seawater sample without disassembling the cell between the first and second cycle. The temperature, conductivity (Oakton Con 11 conductivity meter, Oakton Instruments, Vernon Hills, IL), and pH (Thermo Fisher Orion Star with Orion ROSS pH triode, Thermo Fisher Scientific, Waltham, MA) of the influent and effluent were measured at regular intervals during the electrochemical tests.

2.3 Statistical Methods

When statistical significance was assessed, the fitting and its corresponding R-squared were determined using Origin v2017 (OriginLab Corporation). The student t-tests, one-way analysis of variance (ANOVAs), and random effect tests were performed using RStudio v1.1.383 (Rstudio, Inc.). A p-value less than 0.05 was considered statistically significant. For all statistical analyses, the data from Nelson Bay in September 2016 was omitted because it was determined to be an outlier based on the Dixon's Q-test (95% confidence).

3. Theory

3.1 Open Circuit Voltage

The open circuit voltage (*OCV*, V) is the voltage difference created by the salinity gradient across the membrane stack when no current is flowing [24]. We estimated the ideal

OCV using a previously validated modification of the Nernst equation, wherein the ion activity ratio is replaced by the influent conductivity ratio of the water pair [16]:

$$OCV_{\mathrm{cond}} = N_{\mathrm{m}}\alpha\frac{RT}{zF}ln\frac{\kappa_{\mathrm{C}}}{\kappa_{\mathrm{D}}} \quad (1)$$

where N_{m} (dimensionless) is the total number of ion exchange membranes (IEMs), T (K) is the solution temperature, F (96485 C.mol^{-1}) is the Faraday constant, z is the charge of the ions in solution, α (dimensionless) is the average membrane permselectivity of an AEM/CEM pair, R (8.314 J.mol^{-1}.K^{-1}) is the universal gas constant, and κ_{C} and κ_{D} (S.cm^{-1}) are the conductivity of concentrated and dilute solutions respectively. The experimental *OCV* of the stack was obtained by measuring the stack potential under zero-current.

3.2 Stack Resistance

The resistance of an RED cell is the total resistance of all the components, including electrodes, concentrated/dilute solutions, membranes, spacers, and the diffusion boundary layer [35]. Total resistance (R_{tot}, Ω) is defined as the sum of ohmic and non-ohmic resistances:

$$R_{\mathrm{tot}} = R_{\mathrm{ohmic}} + R_{\mathrm{non-ohmic}} \quad (2)$$

Ohmic resistance (R_{ohmic}, Ω), which follows Ohm's law, is the sum of the dilute (R_{D}) and concentrated solution resistances (R_{C}), membrane resistance (R_{M}), and the resistance due to the spacer shadow effect (R_{SS}) [16] as given by:

$$R_{\mathrm{ohmic}} = R_{\mathrm{D}} + R_{\mathrm{C}} + R_{\mathrm{M}} + R_{\mathrm{SS}} \quad (3)$$

R_{D} and R_{C} were calculated from $\frac{N_{\mathrm{i}}h}{A\varepsilon^2\kappa_{\mathrm{s}}}$, in which $N_{\mathrm{i\ (i=C,D)}}$ (dimensionless) is the total number of concentrated or dilute solution compartments, h (m) is the thickness of the flow channels between the membranes (i.e., the spacer thickness), A (m^2) is the cross-sectional area of a single membrane, ε (dimensionless) is the porosity of the spacer, and κ_{s} is the solution conductivity

with s=C,D. R_M represents the combined resistance to ion transport of the cation and anion exchange membranes used and was experimentally determined from chronopotentiometry technique (this method to calculate R_M is consistent with other RED studies [1,16,36]). R_{SS} represents the resistance of the portion of membrane area that is masked by the spacer and is directly proportional to membrane resistance by $\frac{1-\beta}{\beta}$ [1,16], where β (dimensionless) is the spacer shadow factor. The spacer shadow factor represents the area of the membrane which is covered by the spacer, calculated as $\beta = 1 - \varepsilon$, where ε is the spacer porosity (dimensionless) [16]. Non-ohmic resistance ($R_{non\text{-}ohmic}$, Ω) was calculated as [22,37]:

$$R_{\mathrm{non-ohmic}} = R_{\Delta C} + R_{BL} \quad (4)$$

where $R_{\Delta C}$ is the resistance due to bulk concentration changes caused by ion transport across the membrane, and R_{BL} is the boundary layer resistance. $R_{\Delta C}$ (Ω) can be estimated from [37,38]:

$$R_{\Delta C} = N_m \alpha \frac{RT}{zFj} \ln\left(\frac{A_{\mathrm{dilute}}}{A_{\mathrm{concentrated}}}\right) \quad (5)$$

where j (A.m^{-2}) is the current density and A_{dilute} and $A_{concentrated}$ represent the concentration at the outflow of the dilute and concentrated chambers respectively, and were calculated as [37]:

$$A_{\mathrm{dilute}} = 1 + \frac{jt_{res}}{F\varepsilon h C_{\mathrm{dilute}}} \quad (6)$$

and

$$A_{\mathrm{concentrated}} = 1 - \frac{jt_{res}}{F\varepsilon h C_{\mathrm{concentrated}}} \quad (7)$$

In Eqs. 6 and 7, t_{res} (s) is the solution residence time in the membrane stack, h (m) is the intermembrane distance, and C (mol.l^{-1}) is the total salt concentration in the dilute (C_{dilute}) and concentrated ($C_{concentrated}$) solutions. The boundary layer resistance (R_{BL}, Ω) depends on the change in concentration over time at both the middle of a compartment and at the membrane-solution interface [37,39]. According to Vermaas et al.[37], R_{BL} can be determined as:

$$R_{\mathrm{BL}} = \frac{N_m}{2}\left(0.62 t_{\mathrm{res}} \frac{h}{L} + 0.05\right) \quad (8)$$

where L (m) is the cell length (i.e., the path length of the feed water in the compartment). Experimentally, R_{tot} (Ω) at the maximum power density can be obtained using chronopotentiometry (See Section 2.2) according to [36]:

$$R_{\mathrm{tot}} = \frac{OCV - V_{\mathrm{max}}}{I_{\mathrm{max}}} \quad (9)$$

where V_{max} (V) and I_{max} (A) are the voltage and current recorded at maximum power density. Values of R_{tot}, R_{D}, R_{C}, R_{M}, R_{SS}, $R_{\Delta\mathrm{C}}$, R_{BL} reported below were multiplied by $\frac{A}{N_{\mathrm{cp}}}$ (where A (cm^2) is the cross-sectional area of a single membrane and N_{cp} (dimensionless) is the number of cell pairs in the stack) to obtain units of ($\Omega.\mathrm{cm}^2.\mathrm{cell\ pair}^{-1}$).

3.3 Power Density

Power density is the power generated per unit of total membrane area. Theoretically, the maximum obtainable power density ($PD_{\mathrm{max,theor}}$, $\mathrm{mW.m}^{-2}$) can be calculated using the ideal OCV (Eq. 1) divided by R_{tot} (Eq. 2) and normalized to the total membrane area, yielding [22,37]:

$$PD_{\mathrm{max,theor}} = \frac{OCV^2}{4 N_{\mathrm{m}} A R_{\mathrm{tot}}} \quad (10)$$

where A (m^2) is the cross-sectional area of a single membrane.

Experimentally, maximum power density (PD_{max}, $\mathrm{mW.m}^{-2}$) was obtained by applying several constant-current steps. The applied current [I (A)] and voltage [E (V)] to maintain the constant current were recorded and used to calculate power density according to [40]:

$$PD = \frac{EI}{N_{\mathrm{m}} A} \quad (11)$$

The value at which I and E give the maximum observed PD according to Eq. 11 is defined as $PD_{\mathrm{max,obs}}$. This notation is used to differentiate it from $PD_{\mathrm{max,theor}}$ (Eq. 10).

4. Model Development

Improving our ability to predict power output fluctuations of real waters is important for refining power production estimates from natural salinity gradients. In this study, we explored the possibility of using easily measured variables to estimate the power output from real waters. We evaluated how well we could predict $PD_{max,obs}$ by only knowing two field-measurable water properties: temperature and conductivity. To do this, we combined our experimental data with established relationships that describe RED performance according to known parameters (e.g., *OCV*, PD_{max}, R_{tot}, etc), empirical data, and statistical tools.

The model included three dependent variables representing RED performance: *OCV*, R_{tot}, and PD_{max}. Predicted *OCV* was calculated from the ideal *OCV* relationship derived from the conductivity rule proposed previously [16], corrected for membrane permselectivity (Eq. 2). The total stack resistance, R_{tot}, was calculated as the summation of R_{ohmic} and $R_{non\text{-}ohmic}$ (Eq. 3), with each component of resistance derived from either established relationships (solution resistances: R_C & R_D [16]; concentration gradient resistance: $R_{\Delta C}$ [5] [6]) or previously reported empirical relationship (boundary layer resistance, R_{BL} [37]). Since membrane and spacer-shadow resistances with real waters have not been described mathematically, we first developed relationships for R_M and R_{SS} as functions of our two independent variables: T and κ. We then fit our experimental data using non-linear regression analysis. The assumptions made for this empirical relationship were:

(1) T and κ are independent of each other (validated using linear regression analysis as shown in Figure 3);

(2) The locations where we obtained seawater did not have a significant impact on our dependent variables (assessed using a random effect test based on a linear model in which sampling location was treated as a variable). This analysis focused on variability of the seawater location and did not consider the distance between each location and the WWTP;

(3) The relationship between membrane resistance and temperature is described by an exponential function as described in Ref [41];

(4) The membrane resistance is primarily controlled by the dilute solution [29].

5. Results and Discussion

5.1 Seawater Temperature and Conductivity

We first examined seawater temperature and conductivity across the sampling dates and sites (**Figure 2**). The lowest temperatures were recorded in February and November and ranged from 11-12^{o}C and 14-16^{o}C, respectively, across the sites. The highest temperatures occurred in July (30-33^{o}C) and September (27-29^{o}C) (**Figure 2A**). The samples collected in April fell within a range of 22-23^{o}C.

Seawater conductivity depended on the site and sampling date. Conductivity was relatively constant across the sampling dates at sites BS and TC, averaging 47.06 ± 3.36 mS.cm^{-1} (**Figure 2B**). At site NB, conductivity was dependent on the sampling date, varying from a low of 8.33 mS.cm^{-1} (September) to a high of 47.50 mS.cm^{-1} (February). This variability was likely due to two factors. First, NB is more strongly influenced by freshwater inputs (i.e., rivers) than the other two locations (**Figure 1**). Second, ahead of Hurricane Matthew [43] that made landfall near the sampling sites in early October 2016, extensive precipitation drained into rivers that

emptied along the coast. This surge of freshwater explains the low conductivity reading at NB in September.

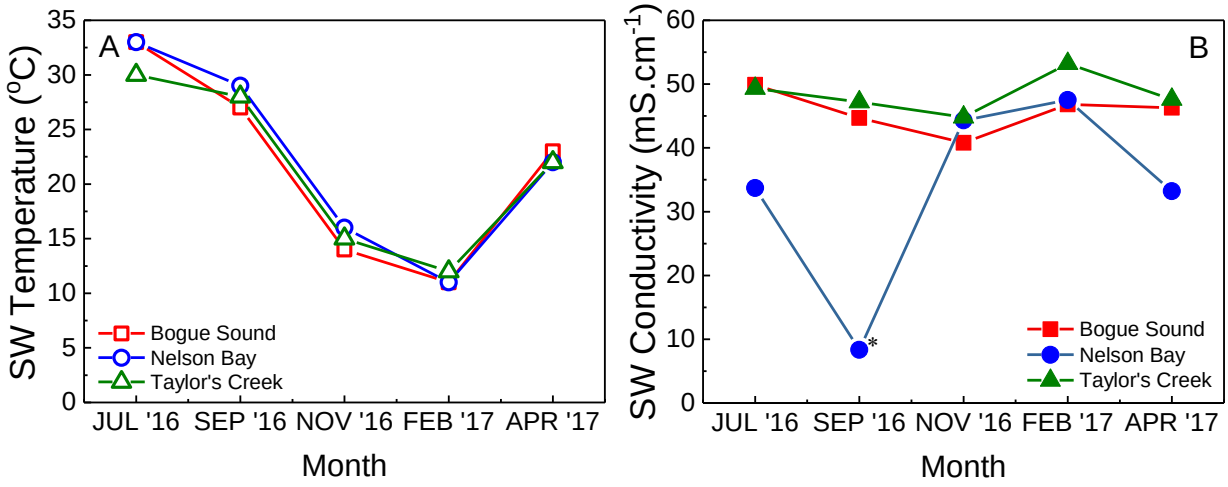

Figure 2. (A) Temperature and (B) conductivity of the seawater (SW) samples collected from three different sites along coastal North Carolina between July 2016 and April 2017. The values were recorded at the same time the samples were collected. Error bars are not included because only one measurement was taken per sampling date at each of the sites. The sample at Nelson Bay in September 2016 impacted by the hurricane is marked with an asterisk (*).

In salt solutions with a constant ionic composition, conductivity is known to increase with temperature [44]; however we did not find a significant association between conductivity and temperature in the waters we sampled (**Figure 3**). In natural waters, the ionic composition and concentration vary throughout the year independently from temperature, such that changes in conductivity cannot be solely attributed to temperature variations. For the waters in our study, we confirmed that conductivity and temperature were statistically independent from each other (R^2 = 0.09, $p < 0.05$). This is an assumption we used to develop our model (sections 4 and 5.4).

Additionally, during the samples collection, we also measured the pH of the real waters. Our findings (Table S1) suggest that the variation in pH of the seawater was relatively small (8.28±0.21). Given that measured pH indicates the presence of charged species [H^+] or [OH^-],

which directly impacts the ionic strength of a solution, any significant change in pH would be reflected in our conductivity measurements.

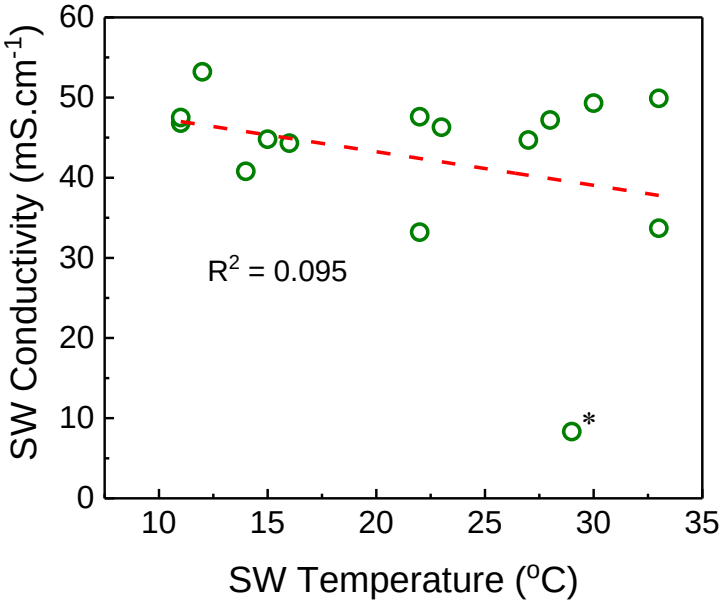

Figure 3. Linear correlation ($p < 0.05$) between seawater (SW) conductivity and temperature for all seawater samples collected from three different sites along coastal North Carolina from July 2016 to April 2017. The sample at Nelson Bay in September 2016 impacted by the hurricane is marked with an asterisk (*).

5.2 RED Power Production

We tested each seawater sample in the RED cells to determine how temperature and conductivity variations affected power output. Maximum experimental power densities ($PD_{max,obs}$) with the BS seawater ranged from 94.4±0.1 mW.m^{-2} (November) to 247.5±10.9 mW.m^{-2} (July) (**Figure 4**). For the NB seawater, a $PD_{max,obs}$ of 137.9±6.2 mW.m^{-2} was obtained from the July sample, but dropped by 93% to 10.4±1.8 mW.m^{-2} with the September sample. This drop was likely due to the substantially lower conductivity of the September NB water caused by the heavy rainfall of Hurricane Matthew diluting the water prior to the sampling date. The

$PD_{max,obs}$ with the TC seawater ranged from 119.3±10.1 mW.m^{-2} (November) to 203.4±11.6 mW.m^{-2} (July). For all samples, the largest $PD_{max,obs}$ was obtained from the July samples, when temperatures were the highest. For the BS and TC seawater, the lowest $PD_{max,obs}$ values were obtained from the November samples which had the second lowest temperatures across all sampling dates.

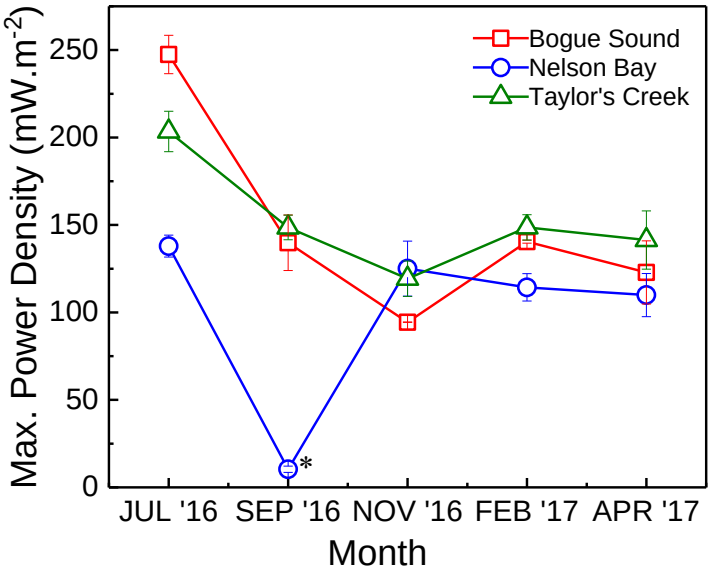

Figure 4. Maximum power densities ($PD_{max,obs}$) obtained from seawater samples collected at three different sites in North Carolina between June 2016 and April 2017. For all tests, the effluent from a domestic wastewater treatment facility located on the coast was used as the dilute solution. Error bars represent the standard error of duplicate experiments (n = 2). The sample at Nelson Bay in September 2016 impacted by the hurricane is marked with an asterisk (*).

To investigate the impact of temperature and conductivity on $PD_{max,obs}$, we examined statistical correlations between these variables and $PD_{max,obs}$. We selected linear correlations because previous studies using synthetic solutions showed that this function described well the relationship between $PD_{max,obs}$ and temperature [22,33,45,46], and $PD_{max,obs}$ and concentration ratio [22,47]. To determine the combined effect of temperature and conductivity, we conducted a

multiple linear regression (**Table S2**). The combined impact of these two variables on $PD_{max,obs}$ was found to be significant ($R^2 = 0.73$, $p<0.05$), with conductivity having a stronger influence than temperature (based on regression coefficients of 4.29 and 3.53 for conductivity and temperature, respectively). Treated separately, neither temperature nor conductivity alone could explain $PD_{max,obs}$ at each site. This conclusion is based on the moderate correlations between temperature and $PD_{max,obs}$ for all sites (BS, $R^2 = 0.53$, $p > 0.05$; NB, $R^2 = 0.46$, $p > 0.05$; TC, $R^2 = 0.45$, $p > 0.05$) (**Figure S2**) and lack of correlation between conductivity and $PD_{max,obs}$ for sites NB ($R^2 = 0.05$, $p > 0.05$) and TC ($R^2 = 0.17$, $p > 0.05$) (**Figure S3B-C**). Only conductivity at site BS could explain well $PD_{max,obs}$ ($R^2 = 0.74$, $p < 0.05$) (**Figure S3A**). This analysis shows that including both temperature and conductivity can better explain the $PD_{max,obs}$ data than using either variable alone. It is important to note, however, that this finding is based on a relatively small sample size (five sampling dates at three sites). More continuous sampling and testing are needed to better refine actual month-to-month $PD_{max,obs}$ variations and the influence of temperature and conductivity.

5.3 Open Circuit Voltage and Resistance

Since $PD_{max,theor}$ is a function of *OCV* and R_{tot} (Eq. 10), we examined whether variations in these two parameters could be explained by changes in temperature or conductivity. The *OCV*s were relatively stable across all sampling sites and dates, except for the September NB sample impacted by the excessive rainfall (**Figure S4A**). Excluding that outlier, the *OCV* averaged 0.545 V and varied by ±0.028 V. Relative to the other sites, the NB *OCV* values were generally the lowest (except the November sample), but the difference across sites was not significant ($p > 0.05$).

In contrast to *OCV*, there were substantial variations in R_{tot} across sampling sites and dates. For all sites, the lowest R_{tot} occurred in July and averaged 74.9±5.1 $\Omega.cm^2$ (**Figure S4B**). The

highest R_{tot} for a given site depended on the sampling date. For BS and TC, maximum R_{tot} of 121.4±2.6 Ω.cm^2 from the BS samples and 107.4±0.8 Ω.cm^2 from the TC samples were recorded with the November sample. The maximum R_{tot} (177.8±17.3 Ω.cm^2) from the NB sample (and the highest R_{tot} recorded across all sampling sites) was obtained from the September sample.

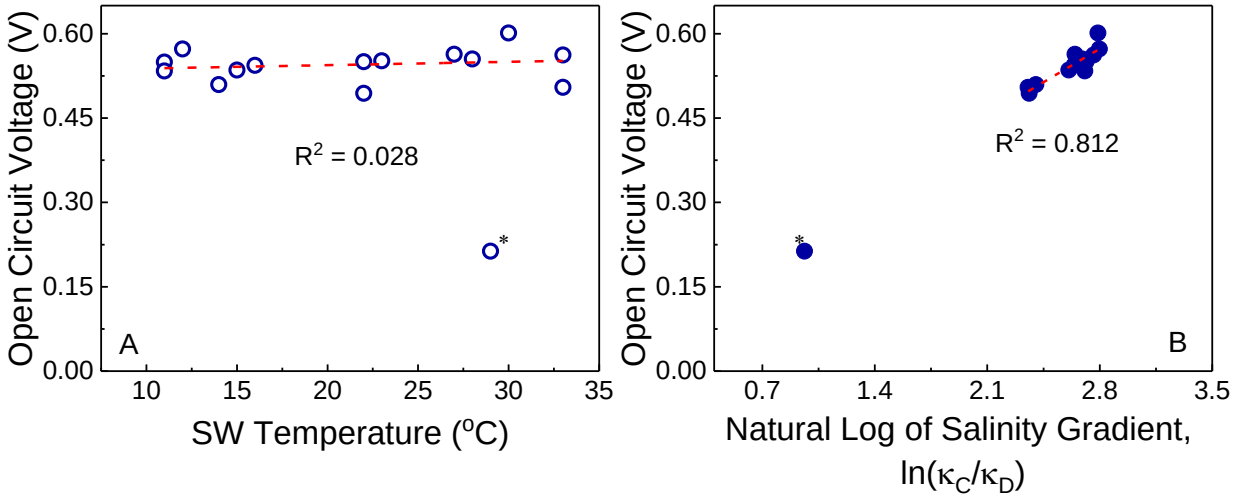

Figure 5. Linear correlations ($p < 0.05$) between (A) open circuit voltage (*OCV*) and seawater (SW) temperature, and (B) *OCV* and natural log of salinity gradient [$\ln(\kappa_C/\kappa_D)$] for all SW samples. The sample at Nelson Bay in September 2016 impacted by the hurricane is marked with an asterisk (*).

We next determined how well temperature and conductivity variations could explain changes in the *OCV* and R_{tot} values. The modified Nernst equation (Eq. 1) indicates that *OCV* is proportional to temperature and conductivity ratio of the concentrated and dilute solutions. Regression analysis of *OCV* versus temperature and natural log of ratio between seawater and wastewater effluent conductivities [$\ln(\kappa_C/\kappa_D)$] showed that *OCV* strongly correlated with $\ln(\kappa_C/\kappa_D)$ (R^2=0.812; **Figure 5B**) but not with temperature (R^2=0.028; **Figure 5A**). Theoretically, the electromotive force should increase as temperature and conductivity increase

[37]. However, as shown in **Figure 5B**, changes in temperature did not substantially impact the *OCV*. Conversely, changes in seawater conductivity affected OCV significantly ($p < 0.05$), which is consistent with prior studies where OCV was proportional to the salinity gradient, as expected from the Nernst equation [16,22,31]. Given that the dilute solution composition in this study was constant across experiments, the strength of the salinity gradient was driven by changes in seawater conductivity only.

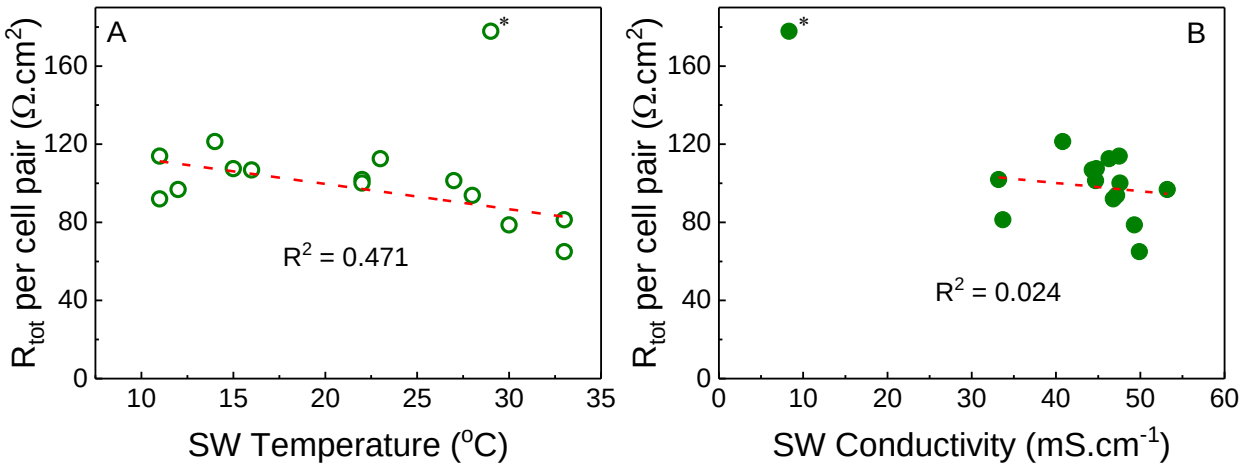

Figure 6. Linear correlations ($p < 0.05$) between (A) total stack resistance (R_{tot}) and seawater (SW) temperature, and (B) R_{tot} and SW conductivity for all SW samples. The sample at Nelson Bay in September 2016 impacted by the storm is marked with an asterisk (*).

While there is a clear relationship between temperature and conductivity and OCV (Eq. 1), there is no obvious scaling relationship between these two variables and resistance (Eqs. 2-9). As a result, we examined linear relationships for our analyses. Temperature was more strongly correlated with R_{tot} than conductivity, albeit only moderately ($R^2 = 0.47$) (**Figure 6A**). In general, low stack resistance was associated with samples that had the highest temperature (33^{o}C for the BS and NB samples, and 30^{o}C for the TC samples) (**Figure S6A**). Membrane resistance was the dominant component of total resistance in most cases, except for samples with the

highest temperatures, of which resistance from the dilute water compartment was the largest component. These findings are consistent with a previous study using synthetic waters where membrane resistance, solution resistance, and non-ohmic resistance decreased as the temperature of the water pair increased [41]. Theoretically, seawater conductivity should affect RED stack resistance by means of solution resistance [22]. However, as shown in **Figure 6B**, changes in seawater conductivity did not significantly impact the total resistance, meaning that it was masked by the large resistance of the dilute solution. Compared to the dilute solution, the average solution resistance of all seawater samples was 90.7% lower (**Figure S7**). As a result, the impact of variation in seawater conductivity on overall stack resistance was not significant ($p>0.05$). Changes in seawater conductivity also had minimal impact on the membrane resistance, which is consistent with prior studies showing that when a membrane separates a gradient, the dilute solution conductivity impacts membrane resistance most significantly [48] [42]. In summary, for the waters tested, we found that the two main parameters that describe $PD_{max,obs}$ (OCV, R_{tot}) were affected differently by temperature and conductivity. Temperature could better explain variations in R_{tot} whereas conductivity was a larger driver of the OCV variability. These results support our conclusions from above that both temperature and conductivity are needed to improve the accuracy of $PD_{max,obs}$ predictions.

5.4. Predictive Model of RED Performance using Real Waters

For our predictive model of power output, we first developed a correlation between the R_M and R_{SS} data obtained from our experiments against the variation in temperature (T, K) from all the seawater samples to generate an empirical relationship for R_M. Non-linear fitting for R_M as function of temperature resulted in the following equation:

$$R_M = 8123.3e^{-0.019T} \quad (12)$$

The spacer-shadow resistance was defined as $\frac{\beta}{1-\beta}R_{\mathrm{M}}$, in which β (dimensionless) is the spacer shadow factor (40% for the spacers used in this study). This yielded:

$$R_{\mathrm{SS}} = 3249.3\mathrm{e}^{-0.019T} \tag{13}$$

By combining our empirically determined relationships (R_{M}, R_{SS}) with those established in the literature (R_{C}, R_{D}, R_{BL}, $R_{\Delta\mathrm{C}}$) to get R_{tot} and OCV_{cond} as a function of T and κ, we then calculated $PD_{\mathrm{max,theor}}$ values (Eq. 10) using the seawater temperature and conductivity values measured in the field. These $PD_{\mathrm{max,theor}}$ values were then validated using our $PD_{\mathrm{max,obs}}$. Regression analysis (**Figure 7**) from the $PD_{\mathrm{max,obs}}$ versus $PD_{\mathrm{max,theor}}$ plot resulted in the following relationship:

$$PD_{\mathrm{max,pred}} = 0.812 * PD_{\mathrm{max,theor}} \tag{14}$$

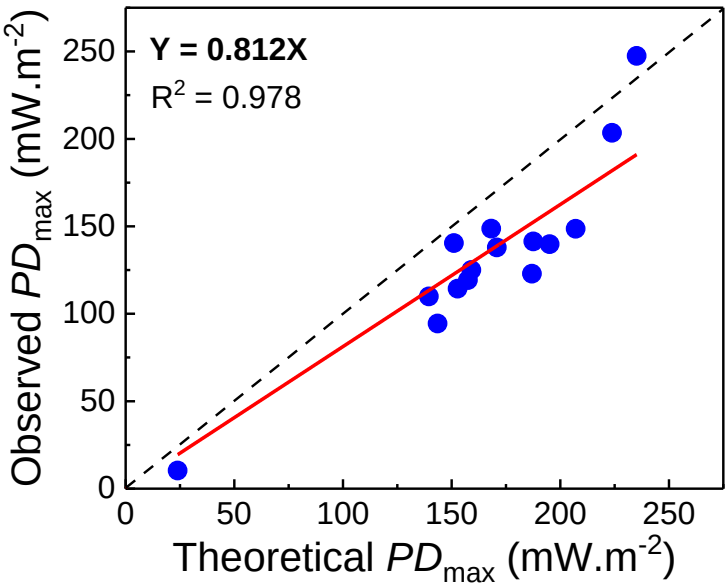

Figure 7. Parity plot between observed ($PD_{\mathrm{max,obs}}$) and theoretical ($PD_{\mathrm{max,theor}}$) maximum power density. The blue circles represent $PD_{\mathrm{max,obs}}$ obtained from all of the seawater samples. The solid red line shows the linear regression between the observed and modeled data, and the dotted line represents a 1:1 relationship.

The coefficient of determination (R^2) from the linear regression on parity plot is equal to 0.978 ($p<0.05$), indicating strong linear relationship. Additionally, eliminating the PD_{max} data from Nelson Bay in the September 2016 sample would not significantly change the slope of the regression forced through zero ($m = 0.813$; $R^2 = 0.979$; $p<0.05$).

Equation 14 shows that, on average, the initial model overestimated the expected power output by 18.8%. A discrepancy between experimental and theoretical PD_{max} was anticipated because: (1) $PD_{max,\,theor}$ is calculated from the maximum obtainable voltage (i.e., zero-current) while $PD_{max,obs}$ is determined when current is flowing through the cell, causing voltage losses [10], and (2) water quality variables, including organic and inorganic constituents, were not considered in the model; however, they are known to decrease power output [16,17]. We calibrated the model by defining the average discrepancy between $PD_{max,theor}$ and $PD_{max,obs,}$ (~18.8%) as the collective impact of all unmeasured factors (e.g., inorganic and organic constituents). This final equation describing the predicted values for PD_{max} ($PD_{max,pred}$) is given below:

$$PD_{\mathrm{max,pred}} = 0.812\,\frac{OCV_{\mathrm{cond}}{}^{2}}{4N_m AR_{\mathrm{tot}}} \tag{15}$$

5.4.1. Model Validation

We investigated the validity of our model using two different data sets: (1) previous reports of RED cells using natural waters, and (2) our own experimental data obtained with a synthetic solution of NaCl. Reports of RED performance using real waters are limited. We selected two papers that examined the impact of real waters on RED performance: Kingsbury et al. [16] and Vermaas et al. [17]. Kingsbury et al. [16] used a similar setup as this study but with a different flow rate (217 $mL.min^{-1}$ vs 107 $mL.min^{-1}$), while Vermaas et al. [17] used similar

concentrated and dilute water pairs (i.e., SW-RW), but a different RED cell design. To be consistent with our study, we only used the water conductivities and temperatures reported in their studies and did not consider other water quality parameters (e.g., ion composition).

Our model predicted maximum power density ($PD_{max,pred}$) within ~20% of the $PD_{max,obs}$ values reported in Kingsbury et al. [16] and Vermaas et al. [17] (**Table S3**). The remaining 20% is attributed to experimental variables (e.g., RED design, water quality properties other than temperature and conductivity, membrane type), uncertainties (e.g., instrument, measurement, and random errors), or statistical bias that were not captured by the model's fitting constant. Nevertheless, an analysis of variance indicated that this difference was not statistically significant (two-sample t-test, $p>0.05$). While the model did a good job at predicting $PD_{max,obs}$ from these two studies, verification with additional data sets are needed to strengthen the applicability of this model for different RED designs and water types.

We also compared model predictions to experimental results using synthetic NaCl solutions in our RED cells. Two-sample t-tests showed $PD_{max,pred}$ to be significantly different than $PD_{max,obs}$ for the synthetic solutions ($p<0.05$, 95% confidence interval). This outcome was expected and can be attributed to our use of empirical correlations derived from real waters. Unlike synthetic NaCl solutions, real waters contain many other constituents, including multivalent ions and NOM. These constituents would increase some metrics (e.g., R_{tot}) and decrease others (e.g., *OCV*) relative to values derived from synthetic solutions, resulting in underestimated $PD_{max,obs}$ for synthetic NaCl solutions.

In order to broaden our $PD_{max,pred}$ predictions across a range of possible seawater conductivities and temperatures, we used the model to create a $PD_{max,obs}$ multi-variable contour plot (**Figure 8**). This plot shows $PD_{max,pred}$ values from real waters (black lines), over a range of two variables: seawater temperature and conductivity. We used the range of 4-35^{o}C and 0-60

mS.cm^{-1} to represent values typical of coastal environments [44]. The near vertical slope of the contours at low conductivity (< 30 mS.cm-1) indicates that a step change in conductivity had a stronger effect on $PD_{max,pred}$ than a step change in temperature. The increased curvature and decreasing slope of the contours at higher conductivity and temperature shows that the effect of temperature became more pronounced and comparable to that of conductivity. The $PD_{max,obs}$ values obtained from previous studies using real waters (red circles) agree relatively well with the contour plot.

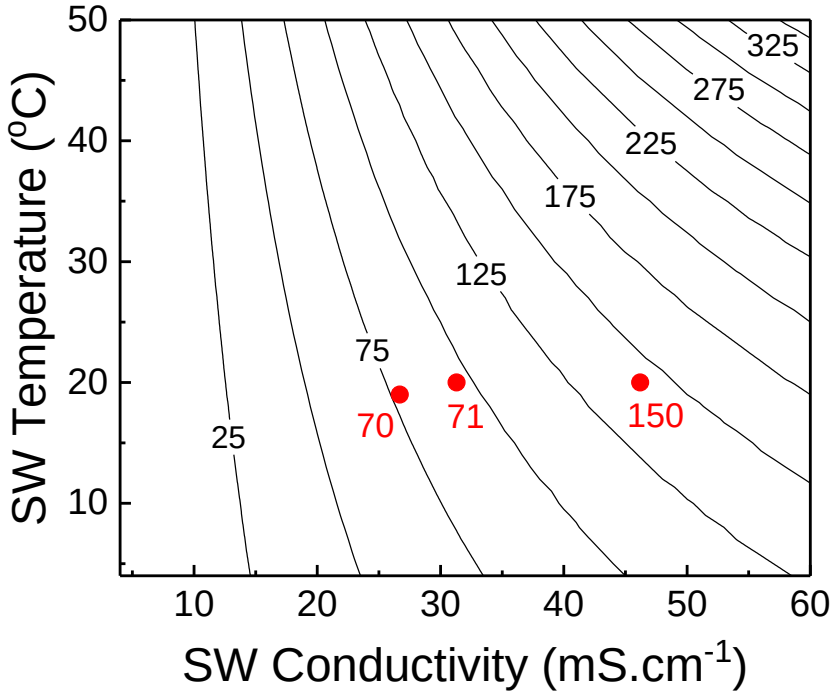

Figure 8. Contour plot of predicted power density (black lines; $PD_{max,pred}$; mW.m^{-2}) from real seawater (SW; concentrated solution) and effluent from a wastewater treatment plant (dilute solution, conductivity of 3.2 mS.cm^{-1}) over a range of temperature and seawater conductivity values representative of coastal environments. The filled red circles are observed maximum power densities ($PD_{max,obs}$; mW.m^{-2}) obtained from other studies using real waters [16,17].

It is important to note that a key assumption in our model is that the dilute solution composition remains constant and has similar properties (e.g., conductivity, inorganic/organic

constituents) as the WW effluent used in this study. Our model development, particularly for the resistance terms, assumed the dilute solution conductivity was constant but the temperature could vary. For the concentrated solution, both conductivity and temperature varied. Therefore, our model validity might be limited to cases where the dilute solution has similar properties to treated WW. Since RED requires a large concentration gradient for power output, the range of practical and abundant dilute solutions along coastlines is relatively small. Coastal wastewater effluent is one such source because its conductivity is typically stable over time and varies little in composition (assuming the plant is meeting its discharge permit) [49]. More general application of our model might require incorporation of variable dilute conductivity, especially in the case rivers that are subject to strong tidal fluctuations [42].

6. Conclusion

Our overall objective was to develop a semi-empirical model to predict power production from coastal salinity gradient energy (SGE) resources by incorporating temporal changes in field-measurable water properties, specifically conductivity and temperature. To do this, we collected several seawater samples between 2016 and 2017 at three sites along the North Carolina coast and tested the waters in lab-scale reverse electrodialysis (RED) cells using the effluent of a wastewater treatment plant as the dilute solution. The following points summarize our major findings:

1. Power densities largely followed the temperature and conductivity trends of the seawater samples. These two variables together correlated strongly with maximum power densities, but separately could not explain well the variance in power densities.

2. Maximum power density varied between 94.4-247.5 $mW.m^{-2}$. Most notably, power output decreased by 92.5% when a major storm event decreased seawater conductivity at one site by 75.3% relative to the prior sampling date, highlighting the susceptibility of salinity gradient power processes to extreme weather events. This sensitivity to storms is consistent with a previous study by Reyes-Mendoza et al. [15].
3. Seawater conductivity was not found to be strongly correlated with temperature, likely due to changes in organic and inorganic ion composition across the sampling dates.
4. A semi-empirical model developed to predict maximum power density (PD_{max}) based on low-cost, field-measurable temperature and conductivity values was able to estimate within ~20% the observed power densities reported by studies using real waters.

Acknowledgements

This research was supported by the University of North Carolina Research Opportunities Initiative (ROI) program and the North Carolina Policy Collaboratory from funding appropriated by the North Carolina General Assembly. We also wish to thank the staff of Beaufort Town Wastewater Treatment Plant for their assistance and support in acquiring effluent samples.

References

[1] J.W. Post, H.V.M. Hamelers, C.J.N. Buisman, Energy recovery from controlled mixing salt and fresh water with a reverse electrodialysis system, Environ. Sci. Technol. 42 (2008) 5785–5790. doi:10.1021/es8004317.

[2] N.M. Bazhin, Gibbs energy role in fresh and salt water mixing, Desalination. 365 (2015) 343–346. doi:10.1016/j.desal.2015.03.023.

[3] G.Z. Ramon, B.J. Feinberg, E.M. V. Hoek, Membrane-based production of salinity-gradient power, Energy Environ. Sci. 4 (2011) 4423. doi:10.1039/c1ee01913a.

[4] R. Aaberg, Osmotic Power, Refocus. 4 (2003) 48–50.

[5] J. Kuleszo, C. Kroeze, J. Post, B.M. Fekete, The potential of blue energy for reducing emissions of CO2 and non-CO2 greenhouse gases, J. Integr. Environ. Sci. 7 (2010) 89–96. doi:10.1080/19438151003680850.

[6] J. Veerman, Reverse Electrodialysis: design and optimization by modeling and experimentation, University of Groningen, 2010.

[7] M.R. Hall, J. West, B. Sherman, J. Lane, D. de Haas, Long-Term Trends and Opportunities for Managing Regional Water Supply and Wastewater Greenhouse Gas Emissions, Environ. Sci. Technol. 45 (2011) 5434–5440. doi:10.1021/es103939a.

[8] International Energy Agency, Key World Energy Statistics, 2019.

[9] J.W. Post, Blue Energy: electricity production from salinity gradients by reverse electrodialysis, Wageningen University, 2009.

[10] Y. Mei, C.Y. Tang, Recent developments and future perspectives of reverse electrodialysis technology: A review, Desalination. 425 (2017) 156–174. doi:10.1016/j.desal.2017.10.021.

[11] B.E. Logan, M. Elimelech, Membrane-based processes for sustainable power generation using water, Nature. 488 (2012) 313–319. doi:10.1038/nature11477.

[12] J.M. Salamanca, O. Álvarez-Silva, F. Tadeo, Potential and analysis of an osmotic power plant in the Magdalena River using experimental field-data, Energy. 180 (2019) 548–555. doi:10.1016/j.energy.2019.05.048.

[13] O.A. Alvarez-Silva, A.F. Osorio, C. Winter, Practical global salinity gradient energy potential, Renew. Sustain. Energy Rev. 60 (2016) 1387–1395. doi:10.1016/j.rser.2016.03.021.

[14] O. Alvarez-Silva, C. Winter, A.F. Osorio, Salinity Gradient Energy at River Mouths, Environ. Sci. Technol. Lett. 1 (2014) 410–415. doi:10.1021/ez500239n.

[15] O. Reyes-Mendoza, O. Alvarez-Silva, X. Chiappa-Carrara, C. Enriquez, Variability of the thermohaline structure of a coastal hypersaline lagoon and the implications for salinity gradient energy harvesting, Sustain. Energy Technol. Assessments. 38 (2020) 100645. doi:10.1016/j.seta.2020.100645.

[16] R.S. Kingsbury, F. Liu, S. Zhu, C. Boggs, M.D. Armstrong, D.F. Call, O. Coronell, Impact of natural organic matter and inorganic solutes on energy recovery from five real salinity gradients using reverse electrodialysis, J. Memb. Sci. 541 (2017) 621–632. doi:10.1016/j.memsci.2017.07.038.

[17] D.A. Vermaas, D. Kunteng, M. Saakes, K. Nijmeijer, Fouling in reverse electrodialysis under natural conditions, Water Res. 47 (2013) 1289–1298. doi:10.1016/j.watres.2012.11.053.

[18] L. Gómez-Coma, V.M. Ortiz-Martínez, J. Carmona, L. Palacio, P. Prádanos, M. Fallanza, A. Ortiz, R. Ibañez, I. Ortiz, Modeling the influence of divalent ions on membrane resistance and electric power in reverse electrodialysis, J. Memb. Sci. 592 (2019) 117385. doi:10.1016/j.memsci.2019.117385.

[19] A. Huyer, Seasonal variation in temperature, salinity, and density over the continental shelf off Oregon, Limnol. Oceanogr. 22 (1977) 442–453. doi:10.4319/lo.1977.22.3.0442.

[20] V. Ittekkot, Variations of Dissolved Organic Matter During a Plankton Bloom: Qualitative Aspects, Based on Sugar and Amino Acid Analyses, Mar. Chem. 11 (2000) 143–158.

[21] N. Ogura, Further Studies on Decomposition of Dissolved Organic Matter in Coastal Seawater, Mar. Biol. 31 (1975) 101–111.

[22] A. Daniilidis, D.A. Vermaas, R. Herber, K. Nijmeijer, Experimentally obtainable energy from mixing river water, seawater or brines with reverse electrodialysis, Renew. Energy. 64 (2014) 123–131. doi:10.1016/j.renene.2013.11.001.

[23] M. Tedesco, A. Cipollina, A. Tamburini, G. Micale, Towards 1 kW power production in a reverse electrodialysis pilot plant with saline waters and concentrated brines, J. Memb. Sci. 522 (2017) 226–236. doi:10.1016/j.memsci.2016.09.015.

[24] M. Tedesco, C. Scalici, D. Vaccari, A. Cipollina, A. Tamburini, G. Micale, Performance of the first reverse electrodialysis pilot plant for power production from saline waters and concentrated brines, J. Memb. Sci. 500 (2016) 33–45. doi:10.1016/j.memsci.2015.10.057.

[25] J. Luque Di Salvo, A. Cosenza, A. Tamburini, G. Micale, A. Cipollina, Long-run operation of a reverse electrodialysis system fed with wastewaters, J. Environ. Manage. 217 (2018) 871–887. doi:10.1016/j.jenvman.2018.03.110.

[26] L. Gómez-coma, V.. Ortiz-Martinez, M. Fallanza, A. Ortiz, R. Ibañez, I. Ortiz, Blue energy for sustainable water reclamation in WWTPs, J. Water Process Eng. 33 (2020) 101020. doi:10.1016/j.jwpe.2019.101020.

[27] M. Vanoppen, T. Van Vooren, L. Gutierrez, M. Roman, L.J. Croué, K. Verbeken, J. Philips, A.R.D. Verliefde, Secondary treated domestic wastewater in reverse electrodialysis : What is the best pre-treatment ?, Sep. Purif. Technol. 218 (2019) 25–42. doi:10.1016/j.seppur.2018.12.057.

[28] S. Pawlowski, C.F. Galinha, J.G. Crespo, S. Velizarov, Prediction of reverse electrodialysis performance by inclusion of 2D fluorescence spectroscopy data into multivariate statistical models, Sep. Purif. Technol. 150 (2015) 159–169. doi:10.1016/j.seppur.2015.06.032.

[29] J. Veerman, R.M. de Jong, M. Saakes, S.J. Metz, G.J. Harmsen, Reverse electrodialysis: Comparison of six commercial membrane pairs on the thermodynamic efficiency and power density, J. Memb. Sci. 343 (2009) 7–15. doi:10.1016/j.memsci.2009.05.047.

[30] J. Veerman, M. Saakes, S.J. Metz, G.J. Harmsen, Reverse electrodialysis : evaluation of suitable electrode systems, J. Appl. Electrochem. 40 (2010) 1461–1474. doi:10.1007/s10800-010-0124-8.

[31] R.S. Kingsbury, K. Chu, O. Coronell, Energy storage by reversible electrodialysis: The concentration battery, J. Memb. Sci. 495 (2015) 502–516. doi:10.1016/j.memsci.2015.06.050.

[32] M. Tedesco, E. Brauns, A. Cipollina, G. Micale, P. Modica, G. Russo, J. Helsen, Reverse electrodialysis with saline waters and concentrated brines: A laboratory investigation towards technology scale-up, J. Memb. Sci. 492 (2015) 9–20. doi:10.1016/j.memsci.2015.05.020.

[33] P. Dlugolecki, A. Gambier, K. Nijmeijer, M. Wessling, Practical potential of reverse

electrodialysis as process for sustainable energy generation, Environ. Sci. Technol. 43 (2009) 6888–6894. doi:10.1109/NEWCAS.2012.6329047.

[34] D.A. Vermaas, J. Veerman, N.Y. Yip, M. Elimelech, M. Saakes, K. Nijmeijer, High efficiency in energy generation from salinity gradients with reverse electrodialysis, ACS Sustain. Chem. Eng. 1 (2013) 1295–1302. doi:10.1021/sc400150w.

[35] J.G. Hong, B. Zhang, S. Glabman, N. Uzal, X. Dou, H. Zhang, X. Wei, Y. Chen, Potential ion exchange membranes and system performance in reverse electrodialysis for power generation: A review, J. Memb. Sci. 486 (2015) 71–88. doi:10.1016/j.memsci.2015.02.039.

[36] D.A. Vermaas, M. Saakes, K. Nijmeijer, Doubled power density from salinity gradients at reduced intermembrane distance, Environ. Sci. Technol. 45 (2011) 7089–7095. doi:10.1021/es2012758.

[37] D.A. Vermaas, E. Guler, M. Saakes, K. Nijmeijer, Theoretical power density from salinity gradients using reverse electrodialysis, Energy Procedia. 20 (2012) 170–184. doi:10.1016/j.egypro.2012.03.018.

[38] D.A. Vermaas, M. Saakes, K. Nijmeijer, Power generation using profiled membranes in reverse electrodialysis, J. Memb. Sci. 385–386 (2011) 234–242. doi:10.1016/j.memsci.2011.09.043.

[39] R.E. Lacey, Energy by reverse electrodialysis, Ocean Eng. 7 (1980) 1–47. doi:10.1016/0029-8018(80)90030-X.

[40] X. Zhu, W. He, B.E. Logan, Influence of solution concentration and salt types on the performance of reverse electrodialysis cells, J. Memb. Sci. 494 (2015) 154–160. doi:10.1016/j.memsci.2015.07.053.

[41] P. Długołecki, P. Ogonowski, S.J. Metz, M. Saakes, K. Nijmeijer, M. Wessling, On the resistances of membrane, diffusion boundary layer and double layer in ion exchange membrane transport, J. Memb. Sci. 349 (2010) 369–379. doi:10.1016/j.memsci.2009.11.069.

[42] S. Zhu, R.S. Kingsbury, D.F. Call, O. Coronell, Impact of solution composition on the resistance of ion exchange membranes, J. Memb. Sci. 554 (2018) 39–47. doi:10.1016/j.memsci.2018.02.050.

[43] S.R. Stewart, Hurricane Matthew, Natl. Hurric. Cent. Trop. Cyclone Rep. Al142016. (2017) 1–96. http://www.nhc.noaa.gov/data/tcr/AL142016_Matthew.pdf.

[44] M. Hayashi, Temperature-electrical conductivity relation of water for environmental monitoring and geophysical data inversion, Environ. Monit. Assess. 96 (2004) 119–128. doi:10.1023/B:EMAS.0000031719.83065.68.

[45] S. Mehdizadeh, M. Yasukawa, T. Abo, M. Kuno, Y. Noguchi, The Effect of Feed Solution Temperature on the Power Output Performance of a Pilot-Scale Reverse Electrodialysis (RED) System with Different Intermediate Distance, Membranes (Basel). 9 (2019) 1–15. doi:10.3390/membranes9060073.

[46] Z. Guo, Z. Ji, Y. Zhang, F. Yang, J. Liu, Y.-Y. Zhao, J.-S. Yuan, Effect of ions (K+, Mg2+, Ca2+ and SO42-) and temperature on energy generation performance of reverse

electrodialysis stack, Electrochim. Acta. 290 (2018) 282–290. doi:10.1016/j.electacta.2018.09.015.

[47] K. Kwon, B.H. Park, D.H. Kim, D. Kim, Parametric study of reverse electrodialysis using ammonium bicarbonate solution for low-grade waste heat recovery, Energy Convers. Manag. 103 (2015) 104–110. doi:10.1016/j.enconman.2015.06.051.

[48] A.H. Galama, D.A. Vermaas, J. Veerman, M. Saakes, H.H.M. Rijnaarts, J.W. Post, K. Nijmeijer, Membrane resistance: The effect of salinity gradients over a cation exchange membrane, J. Memb. Sci. 467 (2014) 279–291. doi:10.1016/j.memsci.2014.05.046.

[49] Primer for Municipal Wastewater Treatment Systems EPA 832-R-04-001, 2004. doi:10.1136/ebmh.7.2.58.

Supporting Information

for

Temporal Variation of Power Production via Reverse Electrodialysis using Coastal North Carolina Waters and its Correlation to Temperature and Conductivity

Elvin H. Hossen[1], Zoe E. Gobetz[2], Ryan S. Kingsbury[3], Fei Liu[3], Hannah C. Palko[4], Lindsay L. Dubbs[4], Orlando Coronell[3], Douglas F. Call[1]*

[1]Department of Civil, Construction, and Environmental Engineering, North Carolina State University, Campus Box 7908, Raleigh, USA

[2]Department of Chemical and Biomolecular Engineering, North Carolina State University, Campus Box 7612, Raleigh, USA

[3]Department of Environmental Science and Engineering, The University of North Carolina at Chapel Hill, Chapel Hill, USA

[4]Coastal Studies Institute, The University of North Carolina at Chapel Hill, Wanchese, USA

*Corresponding author: Douglas F. Call, dfcall@ncsu.edu

Table of contents

Supporting Tables

Supporting Figures

Table S1. Characteristics of the seawater samples collected and measured at three different sites over five different dates and the wastewater (WW) effluent collected at one site on one date. All seawater samples were collected from the sea surface.

	Bogue Sound (BS)					**Nelson Bay (NB)**					**Taylor's Creek (TC)**					**Beaufort effluent (WW)**
Month collected*	1	2	3	4	5	1	2	3	4	5	1	2	3	4	5	5
T. (°C)	33.2	26.7	13.6	10.3	22.6	33.5	27.9	16.3	11.5	21.2	30.2	27.7	14.1	11.8	22.2	21.5
pH	8.1	NA†	8.4	8.5	8.2	8.2	7.9	8.4	8.5	8.3	8.3	8.0	8.5	8.4	8.2	8.2
κ ($mS.cm^{-1}$)	57.5	50.4	44.8	49.9	52.6	38.9	6.5	48.6	51.8	37.5	55.8	53.6	48.7	55.2	53.7	3.2

*1 = July 2016, 2 = September 2016, 3 = November 2016, 4 = February 2017, 5 = April 2017

†Data not available

Table S2. Model parameters from multi linear regression method for $PD_{max,obs}$ versus temperature and conductivity.

Parameter	Estimated Coefficient	Standard Error	p-value
Intercept	-125.74	55.25	0.044
Temperature	3.53	0.77	0.0007
Conductivity	4.29	1.09	0.0024

The estimated coefficients, standard errors, and p-value are given for the corresponding parameters. Standard error represents how much each variable deviated from the mean value. P-value provides the relative contribution of each parameter in the model. For both variables, p-values < 0.05 indicate that temperature and conductivity significantly affected $PD_{max,obs}$. Estimated coefficient for variables show the sensitivity of $PD_{max,obs}$ to the change of temperature and conductivity. The larger the value, the more pronounced the change to the dependent variable (i.e., $PD_{max,obs}$).

Table S3. Comparison between previously reported $PD_{max,obs}$ (observed maximum power density) values and $PD_{max,pred}$ (maximum predicted power density) values from our model.

Water Pair	**Reference**	***T*** **(°C)**	κ_C **(mS.cm^{-1})**	κ_D **(mS.cm^{-1})**	$PD_{max,\ pred}$ **(mW.m^{-2})**	$PD_{max,obs}$ **(mW.m^{-2})**
SW/WW	Kingsbury et al.[1]	20	46.2	0.44	142	150
SW/BW	Kingsbury et al.[1]	20	46.2	3.1	142	110
RO/GW	Kingsbury et al.[1]	20	31.3	8.3	78	70
SW/RW	Vermaas et al.[2]	19	26.7	4.2	95	71
NaCl/NaCl	this study	10	45.4	3.1	112	251
NaCl/NaCl	this study	23	45.4	3.1	137	339
NaCl/NaCl	this study	30	45.4	3.1	165	420

SW = seawater, WW = wastewater, BW = brackish water, RO = Reverse osmosis brine, GW = brackish ground water

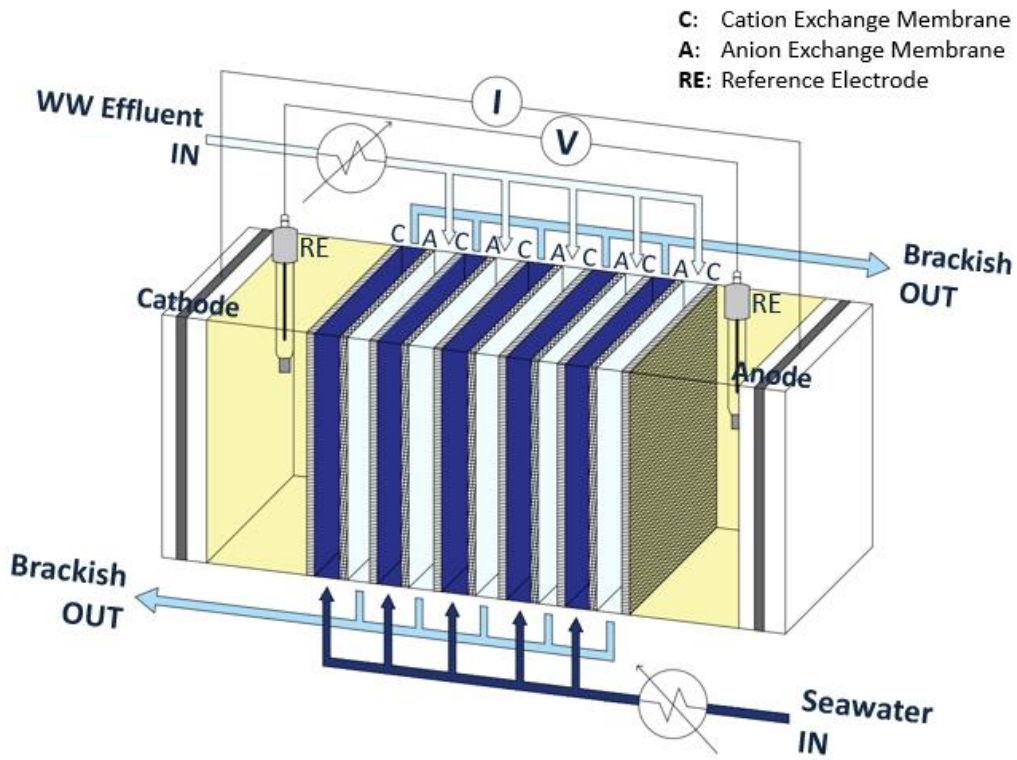

Figure S1. Schematic of the reverse electrodialysis (RED) cell used in this study. The cell consisted of five pairs each of alternating anion and cation exchange membranes (center), two Ag/AgCl reference electrodes on either side of the membrane stack, and a Pt/Ir-coated titanium anode and corrosion-resistant steel cathode. The membrane stack formed alternating chambers that permitted seawater and wastewater effluent to pass through separately.

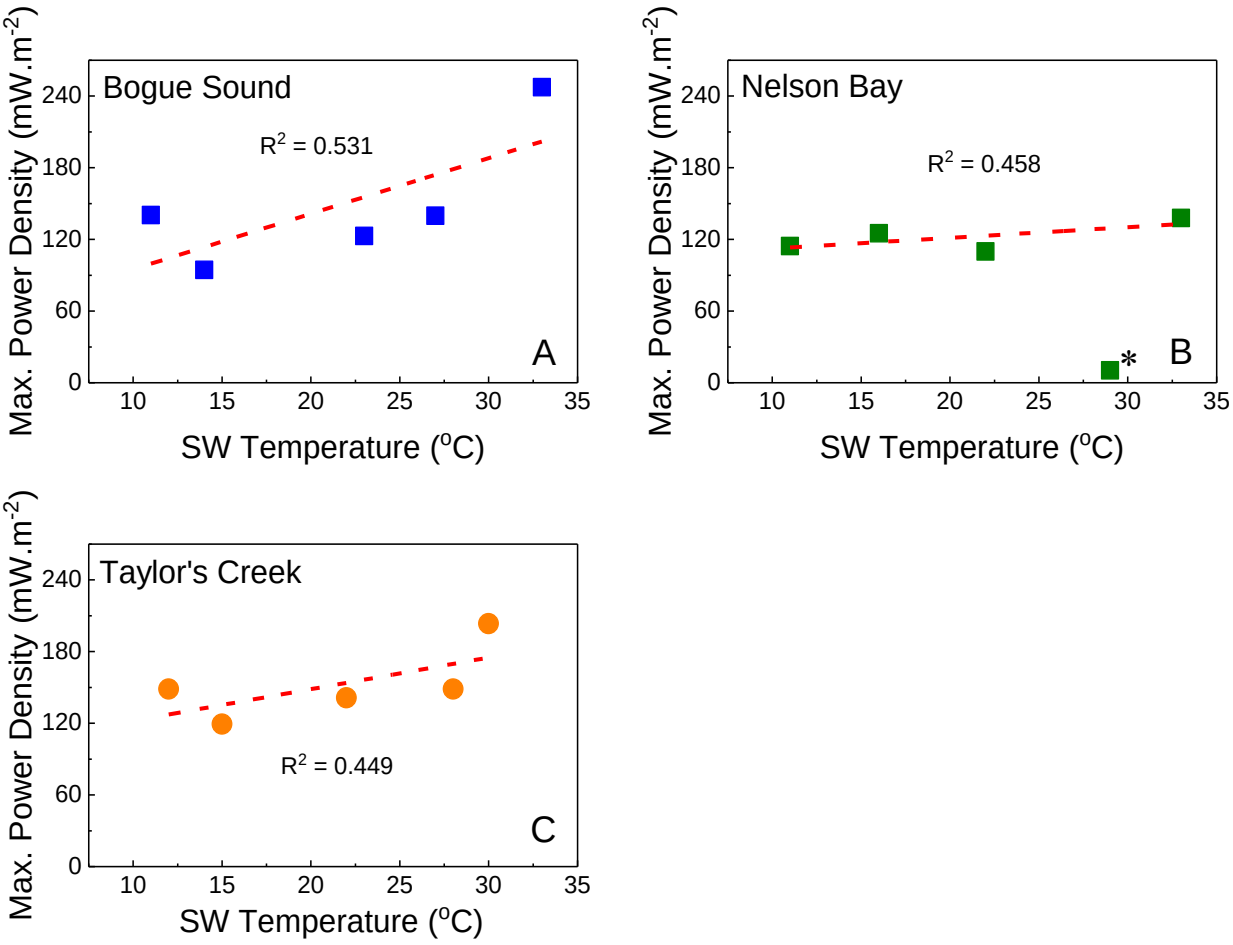

Figure S2. Linear correlations between maximum power density ($PD_{max,obs}$) and temperature of seawater (SW) samples collected from: (A) Bogue Sound, (B) Nelson Bay, and (C) Taylor's Creek. The sample at Nelson Bay in September 2016 impacted by the hurricane is marked with an asterisk (*). All correlations resulted in $p > 0.05$.

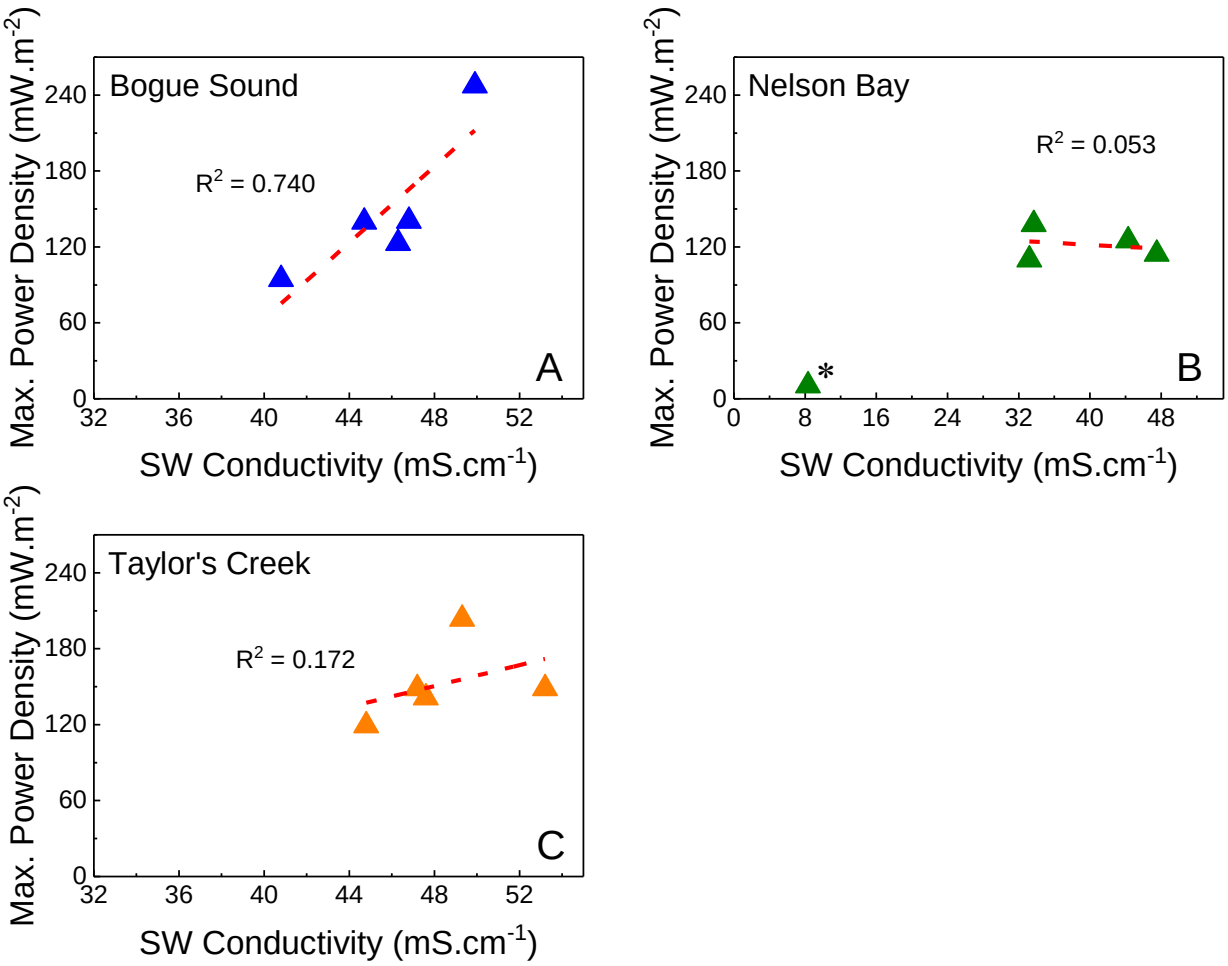

Figure S3. Linear correlations between maximum power density ($PD_{max,obs}$) and conductivity of seawater (SW) samples collected from: (A) Bogue Sound, (B) Nelson Bay, and (C) Taylor's Creek. The sample at Nelson Bay in September 2016 impacted by the hurricane is marked with an asterisk (*). The correlations resulted in $p < 0.05$ for Bogue Sound and $p > 0.05$ for Nelson Bay and Taylor's Creek.

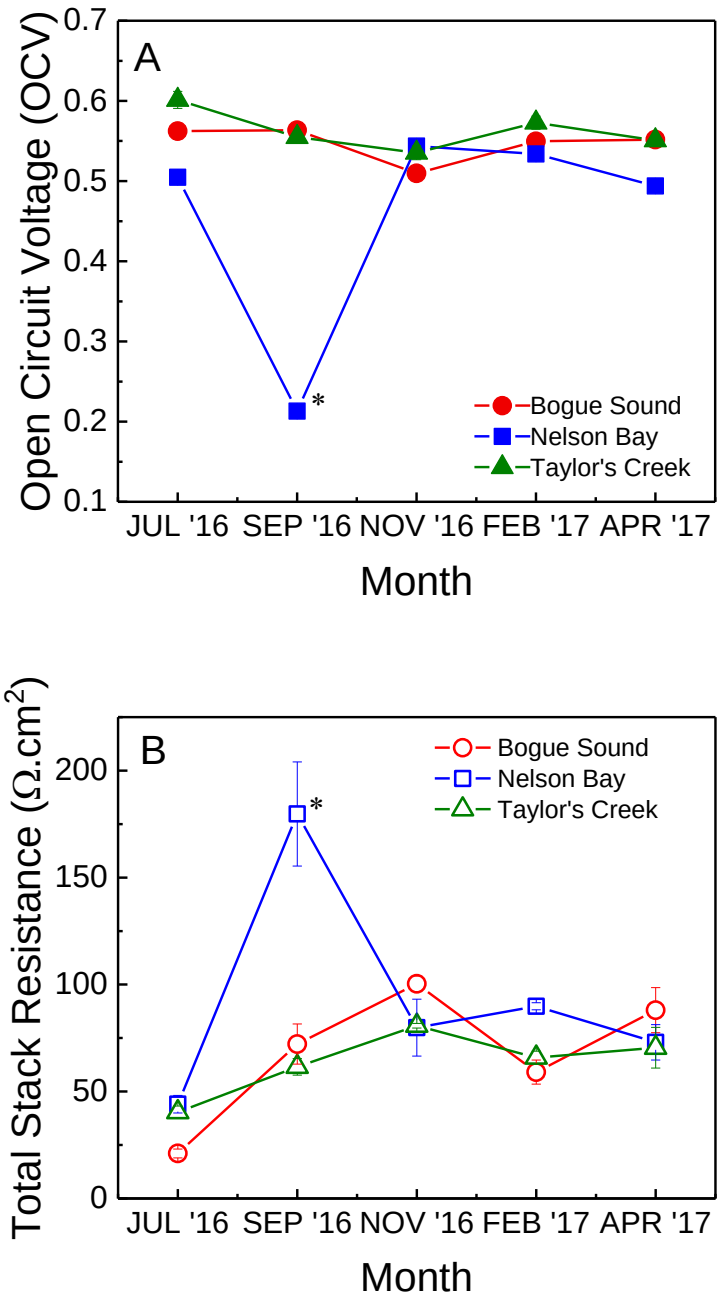

Figure S4. Variation in RED performance parameters: (A) open circuit voltage (*OCV*) and (B) total stack resistance (R_{tot}). Error bars represent the standard error of duplicate experiments (n = 2). The sample at Nelson Bay in September 2016 impacted by the hurricane is marked with an asterisk (*).

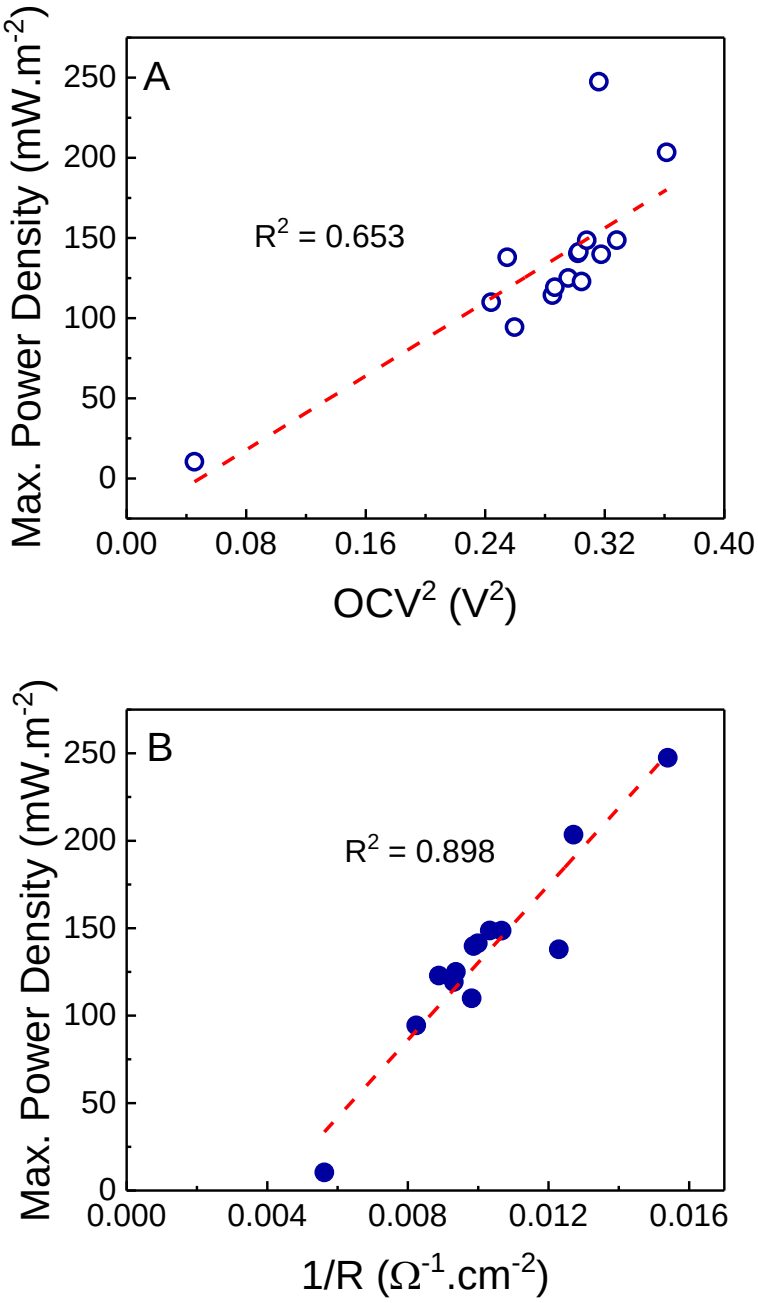

Figure S5. Linear correlations between maximum power density ($PD_{max,obs}$) and (A) the square of the open circuit voltage (OCV^2) and (B) 1/total resistance ($1/R_{tot}$). The data points represent values obtained from all seawater samples ($p < 0.05$).

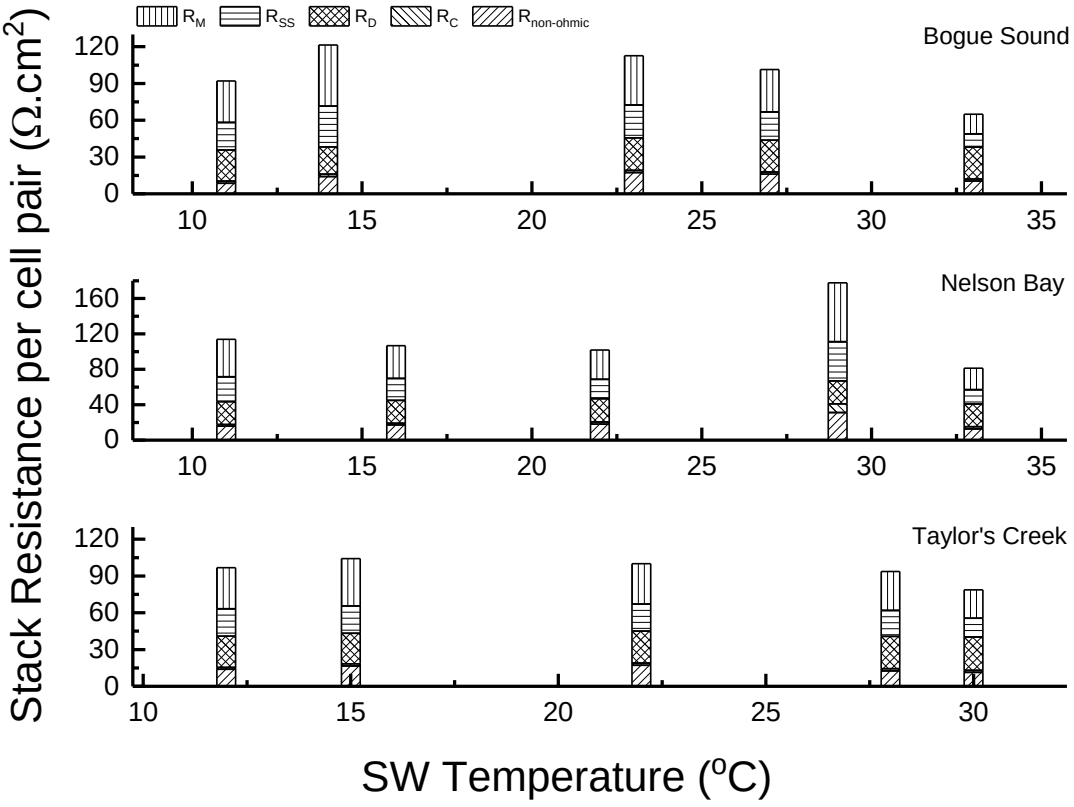

Figure S6. Stack resistance in the RED cells as a function of temperature of each seawater (SW) sample. The samples were adjusted to the temperature that was recorded in the field on each respective sampling date. R_M - membrane resistance; R_{SS} - spacer shadow effect resistance; R_D - solution resistance in the dilute compartment; R_C - solution resistance in the concentrated compartment; $R_{non\text{-}ohmic}$ is the total of all resistance components which do not follow Ohm's law.

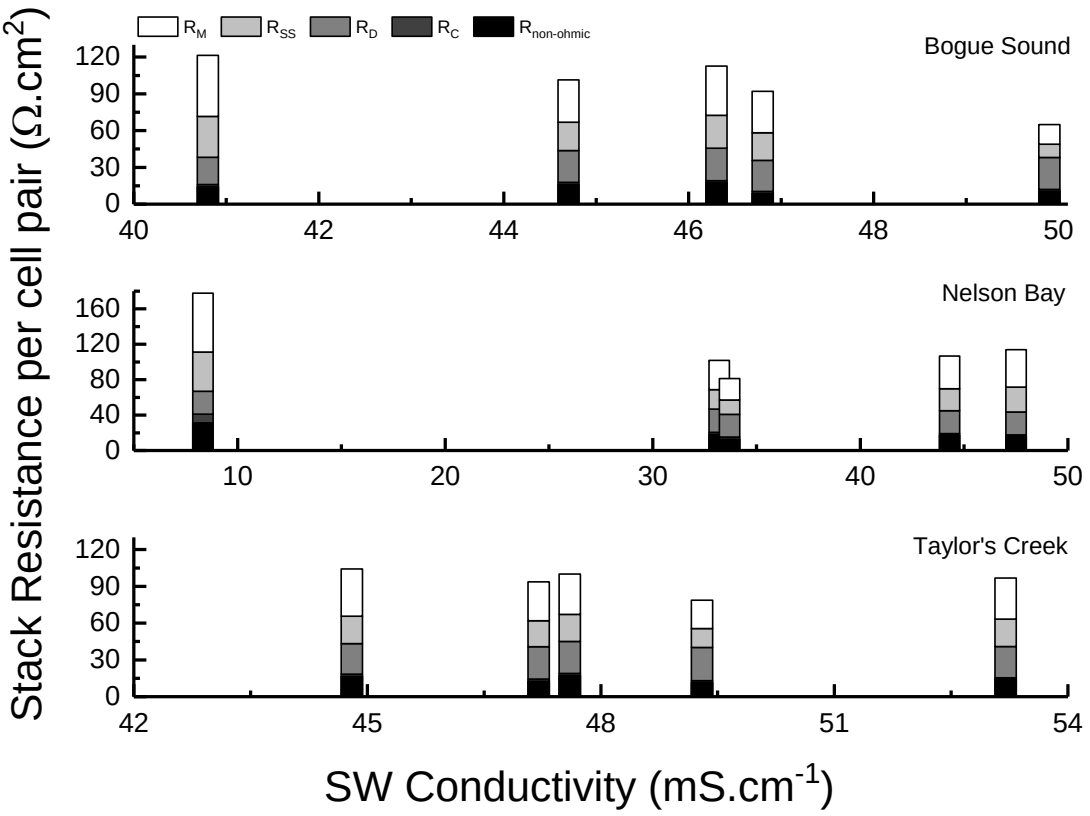

Figure S7. Stack resistance in the RED cells as a function of conductivity of each seawater (SW) sample. R_M - membrane resistance; R_{SS} - spacer shadow effect resistance; R_D - solution resistance in the dilute compartment; R_C - solution resistance in the concentrated compartment; $R_{non\text{-}ohmic}$ is the total of all resistance components which do not follow Ohm's law.